

AD-A114 854

WRIGHT STATE UNIV DAYTON OHIO  
MASS SPECTROMETRIC MEASUREMENTS OF THE CONCENTRATIONS OF GASEOU--ETC(IU)  
APR 82 C CHANG, T O TIERMAN

F/G 7/4

F33615-78-C-2066

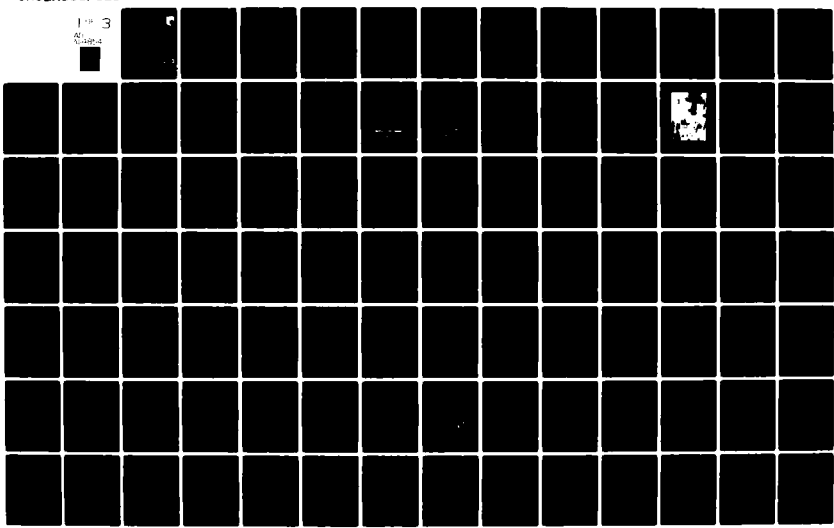
UNCLASSIFIED

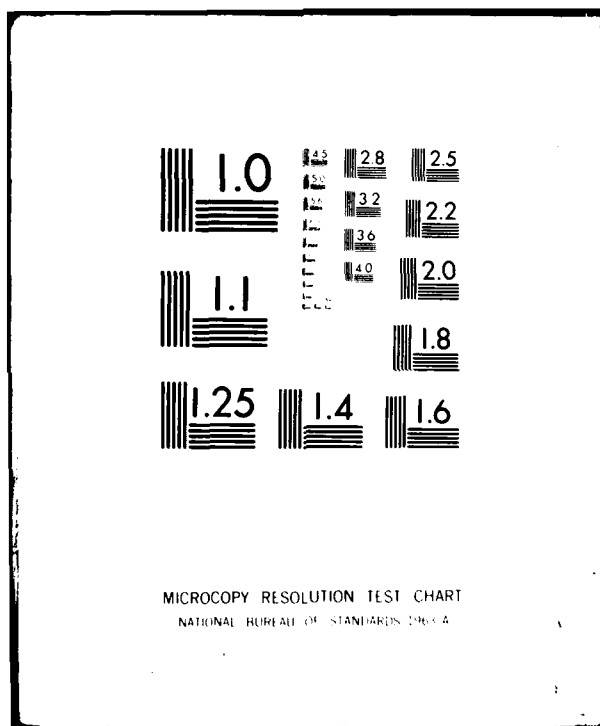
AFWAL-TR-81-2139

NL

1 P 3

AFWAL-TR-81-2139





AFWAL-TR-81-2139

(12)

MASS SPECTROMETRIC MEASUREMENTS OF THE CONCENTRATIONS  
OF GASEOUS SPECIES IN REACTIVE FLOW SYSTEMS (U)

C. CHANG, T.O. TIERNAN  
WRIGHT STATE UNIVERSITY  
DAYTON, OHIO 45435



APRIL 1982

FINAL REPORT FOR PERIOD SEPTEMBER 1978 - SEPTEMBER 1981

ADA114854

APPROVED FOR PUBLIC RELEASE: DISTRIBUTION UNLIMITED

DTIC FILE COPY

AERO PROPULSION LABORATORY  
AIR FORCE WRIGHT AERONAUTICAL LABORATORIES  
AIR FORCE SYSTEMS COMMAND  
WRIGHT-PATTERSON AIR FORCE BASE, OHIO 45433

DTIC  
ELECTED  
MAY 25 1982  
S D  
A

NOTICE

When Government drawings, specifications, or other data are used for any purpose other than in connection with a definitely related Government procurement operation, the United States Government thereby incurs no responsibility nor any obligation whatsoever; and the fact that the government may have formulated, furnished, or in any way supplied the said drawings, specifications, or other data, is not to be regarded by implication or otherwise as in any manner licensing the holder or any other person or corporation, or conveying any rights or permission to manufacture use, or sell any patented invention that may in any way be related thereto.

This report has been reviewed by the Office of Public Affairs (ASD/PA) and is releasable to the National Technical Information Service (NTIS). At NTIS, it will be available to the general public, including foreign nations.

This technical report has been reviewed and is approved for publication.

Raghunath S. Boray

RAGHUNATH S. BORAY  
Project Engineer

FOR THE COMMANDER

Frank D. Stull

FRANK D. STULL  
Chief, Ramjet Technology Branch  
Ramjet Engine Division

"If your address has changed, if you wish to be removed from our mailing list, or if the addressee is no longer employed by your organization please notify AFWAL/PORT W-PAFB, OH 45433 to help us maintain a current mailing list".

Copies of this report should not be returned unless return is required by security considerations, contractual obligations, or notice on a specific document.



of methodology and calibration procedures for monitoring several compounds of interest in an active combustion environment, including O<sub>2</sub>, CO, CO<sub>2</sub>, H<sub>2</sub>O, and hydrocarbon fuels. The third section describes the construction of a flat flame burner system and its application for flame species profiles measurements. Detailed profiles of several stable flame species, including N<sub>2</sub>, O<sub>2</sub>, CO, CO<sub>2</sub>, CH<sub>4</sub>, H<sub>2</sub>O and Ar, were obtained for both methane/air and methane/oxygen flames. Finally, the fourth section of this report is concerned with the design and construction of an innovative sample probe which consists of a quartz micro-probe tip for gas sampling and a water-cooled stainless steel probe body to provide the required physical support and protection for the tip. A theoretical analysis of the new probe design, in connection with its use for sampling a hostile combustion environment, which is characterized by high temperature high gas velocity and high pressure, as is typically the case in a ramjet combustor flowfield, is presented. The results of this analysis indicate that more reliable gas species concentration measurements can be made using the new probe system than have been possible with most other conventional probe designs. Several experimental aspects of the new probe system for ramjet combustor sampling are also described, including details of the construction of a prototype of the new probe system, as well as a batch sampling system, which is interfaced with an existing ramjet combustor facility. Several reactive ramjet combustor sampling tests using these new systems were also conducted for the evaluation of the performance of the sampling probe.

## FOREWORD

This report describes a contractual research effort involving development and utilization of a gas diagnostics system for use in evaluating ramjet combustor performance. This work was performed by Wright State University, under contract F33615-78-C-2066 in support of Work Unit 2308-S2-03. The technical monitor for this contract was Dr. R.S. Boray (AFWAL/PORT) of the Ramjet Technology Branch, Ramjet Engine Division, Aero Propulsion Laboratory. This work was completed and submitted in December 1981.



Accession For	
NTIS CRA&I	<input checked="" type="checkbox"/>
DFIG TAB	<input type="checkbox"/>
Unannounced	<input type="checkbox"/>
Justification	
Pv. ....	
Distribution/	
Availability Codes	
Avail and/or	Special
Spec	Special
A	

## TABLE OF CONTENTS

<u>Section</u>	<u>Page</u>
I      INTRODUCTION . . . . .	1-2
II     MEASUREMENT OF SIMULATED FUEL CONCENTRATION PROFILES . . . . .	2-14
A. System Description . . . . .	2-6
B. Experimental Results . . . . .	6-14
III    DEVELOPMENT OF METHODOLOGY FOR MONITORING GASEOUS SPECIES IN REACTIVE COMBUSTION ENVIRONMENTS . . . . .	14-42
A. Development of Monitoring Methodology for H <sub>2</sub> O . . . . .	20-24
B. Development of Quantitative Calibration Procedures for the Determination of the Concentrations of Gaseous Species in the Combustion Flame . . . . .	24-42
1. Parametric Study . . . . .	28-30
2. Individual Gas Calibration . . . . .	30-42
a. Methane	
b. Carbon Dioxide	
c. Oxygen	
d. Carbon Monoxide.	
e. Water	
3. Summary . . . . .	42
IV    MEASUREMENT OF GAS SPECIES CONCENTRATION PROFILES IN A ONE- DIMENSIONAL FLAT FLAME . . . . .	42-72
A. System Description . . . . .	45-53
B. Experimental Results . . . . .	53-71
V    GAS SAMPLING PROBE SYSTEM FOR RAMJET COMBUSTOR SAMPLING - THEORETICAL ANALYSIS . . . . .	71-81
A. Introduction . . . . .	71,72
B. Analysis of the New Probe Design . . . . .	72-81

TABLE OF CONTENTS (CONT.)

<u>Section</u>	<u>Page</u>
VI. GAS SAMPLING PROBE SYSTEM FOR RAMJET COMBUSTOR SAMPLING - SOME EXPERIMENTAL ASPECTS . . . . .	81-96
A. Description of the Probe . . . . .	81-86
B. Combustor Batch Sampling and Analysis . . . . .	87-91
C. Experimental Results . . . . .	91-96
REFERENCES . . . . .	97-98
APPENDIX . . . . .	99-204
A. Overall Heat Transfer Considerations For a Quartz/Stainless Steel Probe . . . . .	99-111
B. Characterization of the FlowField in The Probe Sampling System . .	112-142
C. Discussion of the Validty of Gas Species Concentration Measurements Using the Present Probe Sampling System . . . . .	143-172
D. A Revised Calculation of the Gas Flowfield In The Present Probe Sampling System . . . . .	173-181
E. Analysis of The Digital Mass Programer and The Signal Demultiplexing Modules . . . . .	182-204
F. Discussion of the Errors in the Present Flame Species Concentration Measurements . . . . .	205-211

## LIST OF ILLUSTRATIONS

	<u>Page</u>
1. Schematic Diagram of the Cold Flow Ramjet Combustor and the Mass Spectrometer Gas Sampling System.	3
2. Radial Profiles of Normalized Argon Mole Fraction for $D_I = D^* = 2.0$ in., $P_{OA} = 30.5$ psia and $P_{OF} = 87$ psia.	8
3. Radial Profiles of Normalized Argon Mole Fraction for $D_I = D^* = 3.0$ in., $P_{OA} = 22.5$ psia and $P_{OF} = 87$ psia.	9
4. Normalized Argon Concentration Results.	12
5. Photograph of the Dual Inlet Ducted Rocket Combustor	13
6. Schematic Diagram of the Gas Calibration Systems.	17
7. Schematic Diagram of the Water Inlet System for Calibration Applications.	22
8. Plot of the Ion Intensity Ratio $[I_{18} - (I_{18})_0]/(I_{14} - (I_{14})_0)$ vs. the Flow Rate Ratio $[FR]_{H_2O}/[FR]_{N_2}$ .	25
9. Plot of the Relative Ion Intensity Ratio $[I_{15} - (I_{15})_0]/[I_{40} - (I_{40})_0]$ vs. the Gas Flow Rate Ratio $[FR]_{Methane}/[FR]_{Air}$ .	33
10. Plot of the Relative Ion Intensity Ratio $[I_{44} - (I_{44})_0]/[I_{40} - (I_{40})_0]$ vs. the Gas Flow Rate Ratio $[FR]_{CO_2}/[FR]_{Air}$ .	35
11. Plot of the Relative Ion Intensity Ratio $[I_{40} - (I_{40})_0]/[I_{32} - (I_{32})_0]$ vs. the Gas Flow Rate Ratio $[FR]_{Ar}/[FR]_{O_2}$ .	36
12. Plot of the Relative Ion Intensity Ratio $[I_{20} - (I_{20})_0]/[I_{12} - (I_{12})_0]$ vs. the Ratio $[FR]_{Ar}$ from $Ar/R$ .	41
13. Schematic Diagram of the Flat Flame Burner Assembly.	46
14. Plot of the Air Flow Rate Through the Quartz Microprobe vs. the Manifold Pressure.	49
15. Schematic Diagram of the Miniature Water-Cooled Metal Probe.	52
16. Mole Fraction Profiles in the Methane/Air Flame. Test No. 1.	63

LIST OF ILLUSTRATIONS (CONT.)

	<u>Page</u>
17. Mole Fraction Profiles in the Methane/Oxygen Flame. Test No. 2.	65
18. Comparison of the Derived CO Mole Fraction Profiles Based On Two Different Methods.	68
19. Mole Fraction Profiles In The Methane/Oxygen Flame. Test No. 3.	70
20. Schematic Diagram of the Gas Probe Sampling System and the Profiles of the Gas Velocity, Temperature, Pressure, and Density of the Sampled Gas Within the Probe Sampling System.	74
21. Schematic of the Quartz/S.S. Sampling Probe.	83
22. Schematic of the Batch Combustor Sampling Stand.	88
23. Schematic of the Sample Inlet System.	90
24. Photograph of the Sampling Probe After the Ramjet Combustor Sampling Tests.	92
25. Mass Spectrum of the Ramjet Combustor Gas Sample.	96
A-1. Schematic representation of the sampling probe for the calculation of the heat transfer rate.	102
B-1. Schematic illustration of the gas flowfield within the present probe sampling system.	113
B-2. Profiles of the velocity, temperature and number density of the sampled gas within the present probe sampling system.	126
B-3. Schematic illustration of the interface between the probe and the mass spectrometer monitoring system.	131
C-1. Plot of quenching ratio as a function of position for CO within the present probe sampling.	158
C-2. Plot of $(V_a/V) (dN_{CO}/dt)/(dN_{CO}/dt)_a$ as a function of position for CO within the present probe sampling system.	163
E-1. Schematic Diagram of the Interface Between the DMP and DM Modules and the Mass Spectrometer.	183
E-2. The Ion Mass As a Function of the "start AMU" Control Settings.	186
E-3. $\log (1 - \frac{V_0}{V_i})$ As a Function of Sampling Time.	188
E-4. Time Sequence of Events in the Data Acquisition Process.	190

LIST OF ILLUSTRATIONS (CONT.)

	<u>Page</u>
E-5. Schematic of the Sample/Hold Circuit.	194
F-1. Material Balance of C,H, and O atoms.	210

## LIST OF TABLES

	<u>Page</u>
I. Experimental Parameters for Argon/Air Mixing Profile Tests.	7
II. Measured Argon/Air Mixing Data.	15,16
III. Effects of Experimental Conditions on Observed Ion Intensity Ratios.	29
IV. Formuale For the Calculation of the Relative Mole Fractions of Gaseous Species.	43
V. Calibration Coefficients Derived From the Gas Calibration Tests.	44
VI. Experimental Conditions for Flame Sampling Tests.	60
VII. Experimental Conditions for Flame Sampling Tests.	62
E-I. A Revised Computer ID Sheet for Mass Spectrometer Data Acquisition.	204

## I. INTRODUCTION

For several years, the Ramjet Technology Branch of the Aero Propulsion Laboratory (APL) has conducted a research program in the area of advanced ramjet combustion. A major goal of this research has been to achieve a superior combustor design for volume-limited ramjet missile applications. Under this program, the effects of various experimental factors, including the combustor configuration, and the types of flame holder and swirler, as well as the operating conditions (fuel-air ratios, inlet gas temperature and pressure, fuel types) on the over-all combustion efficiency have been evaluated (1-5). Detailed characterization of the combustor flowfield under simulated combustion conditions has also been accomplished in several instances (6-9).

Over the past three years a contractual research effort conducted by Wright State University has also been supported by APL. This program has been concerned with relating to the development and utilization of a sophisticated combustor gas diagnostics system for use in evaluating ramjet combustor performance. This effort was an extension of previous APL-funded contractual research programs, under which a sampling probe-mass spectrometer gas monitoring system was successfully developed and applied for in-situ measurements of the concentrations of gaseous species in simulated dump combustor flowfields. Extensive data on fuel concentrations were acquired using this system for various combustor operating conditions. These data have contributed significantly to the in-depth characterization of the combustor flowfield, and the understanding of the fuel-air mixing phenomena and its effect on the over-all combustion efficiency. The results of these research programs have previously been documented in several detailed reports (10,11).

The present Final Report summarizes the accomplishments during the entire three-year contract period.

In view of the diverse nature of various portions of the work described herein, this report is presented in four parts. The first part (Section II) describes the results of cold flow sampling tests utilizing the existing facility, but with some changes in the ramjet combustor configuration. The second part (Section III) documents the progress achieved in the development of methodology for monitoring several compounds of interest in the active combustion environment, including  $O_2$ ,  $CO$ ,  $CO_2$ ,  $H_2O$  and hydrocarbons. The third part (Section IV) describes the construction of a flat flame burner system and its application for flame species profile measurements. Finally, the fourth part (Sections V, VI) is concerned with design and construction of an innovative sample probe, and the application of this new probe for actual combustion sampling.

## II. MEASUREMENT OF SIMULATED FUEL CONCENTRATION PROFILES

### A. System Description.

A major task which was undertaken during the present contract was the in-situ measurement of the concentrations of gaseous species in the ramjet combustor flow field under simulated combustion conditions. The goal of this effort was to study fuel-air mixing phenomena, the understanding of which are vital to the achievement of better combustion efficiency. The initial phase of this portion of the research was conducted in the course of an earlier contract. The latter yielded a considerable quantity of mixing data for a dump combustor having a basic configuration (10,11). Substantial progress was also achieved during the present program in extending the fuel-air concentration measurements to several new combustor designs.

Shown in Fig. 1 is a schematic diagram of the cold flow ramjet combustor and the interfaced mass spectrometer gas sampling system. The basic ramjet combustor

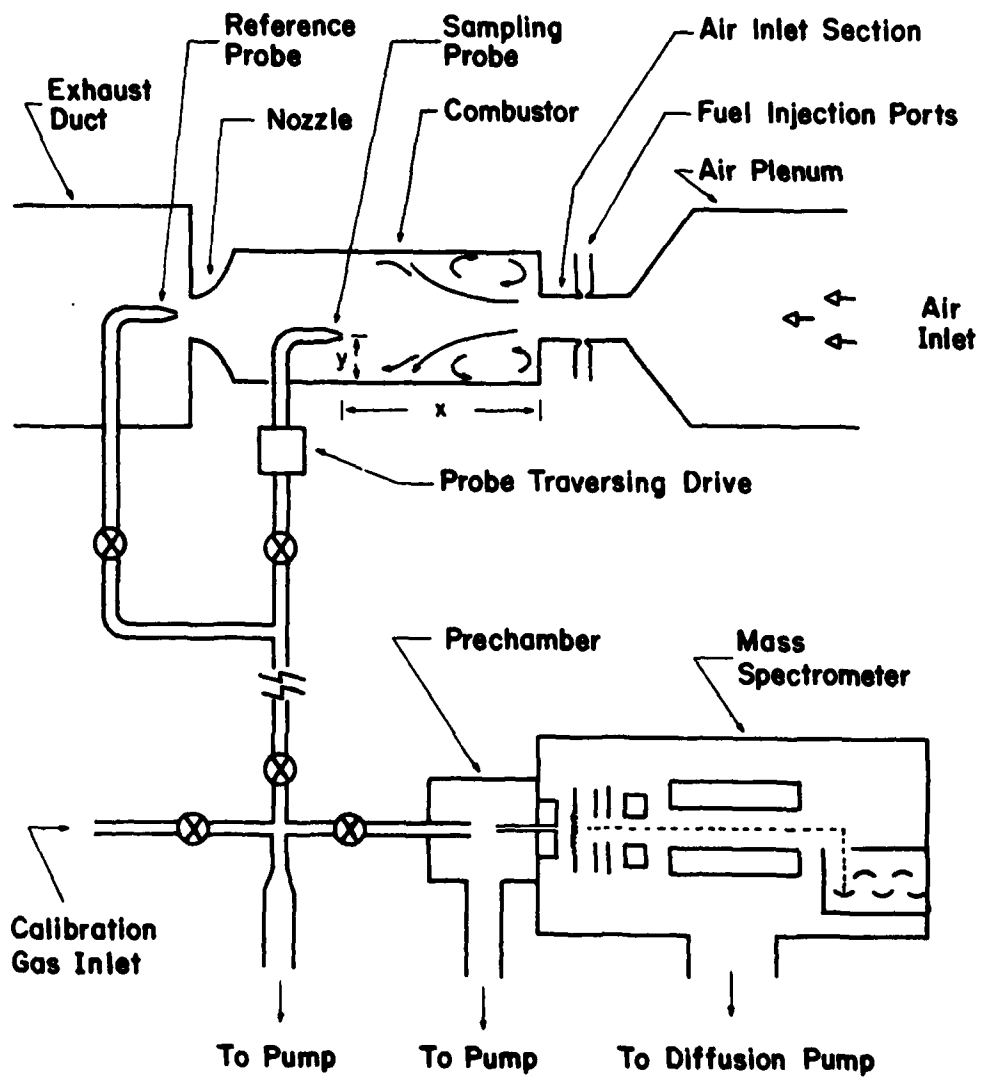


Figure 1. Schematic Diagram of the Cold Flow Ramjet Combustor and the Mass Spectrometer Gas Sampling System.

facility consists of an air plenum, an air inlet section with several fuel injection ports, a ramjet combustor chamber, a nozzle and an exhaust duct. Several removable windows are located on the sides of the combustor chamber, and a sampling probe can be inserted through these openings. A probe-traversing drive is installed as shown, to permit automatically moving the probe across the combustor chamber. This can be done either continuously or in step-wise fashion during a typical experiment. A fixed reference probe is also positioned to sample the fuel-air mixture as it exits from the nozzle.

During a typical fuel-air mixing test, a trace quantity of simulated fuel (argon) is injected into the air stream in the inlet section. Mixing of the argon and air occurs mainly within the combustion chamber section. This mixture is then sampled by the sampling probe and subsequently analyzed on-line, and in real time by the mass spectrometer system.

The mass spectrometer employed in this study incorporates a quadrupole mass filter and is interfaced with a computer for on-line, real-time data acquisition. For the studies reported here, data acquisition rates were set at one (low speed) or ten (high speed) data points per second (for all or up to 64 channels simultaneously), each data point being the integrated value over 128 or 8 analog-to-digital raw data values, respectively. The mass spectrometer system was also equipped with a 6-channel mass programmer which allows rapid sequential monitoring of as many as six different ion species. Since only the fuel-air ratio was to be monitored in the initial tests, only two channels of the mass programmer were utilized. The first channel was tuned to an ion mass ( $m/z$ ) characteristic of the fuel species, while the second channel was tuned to an ion characteristic of air. Switching between these two channels was controlled by a pulse (5 volts, 10 msec duration) which was synchronized with the computer data acquisition process. At the low data acquisition rate, a total time period of two seconds is required to yield one fuel/air ratio data point. On the other hand, at the high data acquisition rate, the same set of data can be obtained in only 0.2 second.

In order to cope with the continuously changing sampling environment within the combustion chamber, resulting from such factors as pressure fluctuations, sharp concentration gradients, and variations of the dynamic flow field patterns, all of which affect the operation of the mass spectrometer, a continuously operating built-in calibration system must be utilized in order to ensure detection accuracy. Such a calibration system is also desirable so that any mass discrimination which occurs in sampling along the entire inlet line can be properly corrected. To this end, argon was selected as the simulated fuel in the fuel-air mixing tests, since its natural abundance in air (0.934%) provides a convenient internal standard for the calibration of the gas analysis system.

During a typical fuel-air mixing test, the sampling probe was first allowed to traverse the combustor flow field, into which only pure air had been injected. The mass spectrometer system was separately calibrated for each sampling point, irrespective of the variation of the sampling environment. Subsequently, the same combustor flow field, into which both air and argon had been injected, was sampled with the sampling probe, and the gaseous sample was analyzed by the mass spectrometer. The two runs described were conducted under essentially identical conditions, except for the fact that argon was introduced during the second run. Since the quantity of argon injected normally amounted to only 1% or less of the quantity of air introduced into the flow field, the presence of the injected argon did not significantly perturb the flow field at the sampling point. The accuracy of the concentration measurement could thus be assured.

Signals from the mass spectrometer are continuously acquired by the interfaced computer during a given test. At the end of the test the data obtained are, in turn, processed and converted into a readable output, which is usually presented in the form of a mole fraction profiles. Recently, a new computer system was installed for use with the analytical instrumentation and concurrently, the computer program for processing the acquired data was updated and modified, so that the

entire data reduction process can be performed automatically, without manual intervention.

### B. Experimental Results.

The first portion of the cold flow sampling work accomplished during the present reporting period entailed measurement of the dump combustor argon mole fraction profiles. An extensive series of tests were conducted to evaluate the effects of various design and operational parameters on the fuel-air mixing efficiency. The data obtained complement and extend the information derived during the previous contract, in which all data were obtained with an inlet section of 2.5 in. I.D. ( $D_I$ ). In the current sampling tests, two new inlet sections having diameters of 2 in. and 3 in I.D., respectively, were employed, along with two new nozzles having nozzle orifice diameters ( $D^*$ ) of 2 in. and 3 in., respectively. Thus, these studies directly evaluate the performance of the ramjet combustor with various inlet section dimensions and different nozzle sizes. In addition, several other parameters were varied in these tests, and the effects on the argon mole fraction profiles were observed. Among these variables were the inlet air pressure, inlet argon pressure, probe position, type of sampling probe (static or impact probe), orientation and numbers of fuel injection ports, and sampling rate. The data obtained, coupled with the information derived from other diagnostic techniques, such as flow visualization and pressure measurements, yield an in-depth characterization of the combustor flow field.

Experimental parameters relevant to these tests are listed in Table I. For the sake of illustration, two sets of radial and axial concentration profiles of injected argon, obtained in these tests, are shown in Figures 2 and 3. The profiles in Fig. 3 were obtained with an inlet section of 3 in I.D. and a nozzle having an orifice diameter of 3 in. The injected argon pressure (POF) in both cases was 87 psia. The inlet air press (POA) employed for the measurements shown in Fig. 2 was 30.5 psia while that for the measurements shown in Fig. 3 was

TABLE I  
EXPERIMENTAL PARAMETERS FOR ARGON/AIR MIXING  
PROFILE TESTS

<u>PoA</u> <u>(psia)</u>	<u>PoF</u> <u>(psia)</u>	<u>X</u> <u>(inches)</u>	<u>DI</u> <u>(inches)</u>	<u>D*</u> <u>(inches)</u>	<u>Mode</u>	<u>Probe</u>
22.4	88	8.69	2	2	low	impact
30.5	88	8.69	2	2	low	impact
22.5	89	4.06	2	2	low	static
30.5	87	4.06	2	2	low	static
30.5	87	10.06	2	2	low	static
30.5	87	11.44	2	2	low	static
30.5	87	5.44	2	2	low	static
30.5	87	2.69	2	2	low	static
22.5	87	8.69	2	2	low	static
30.5	87	8.69	2	2	low	static
30.5	87	0.10	2	2	low	impact
30.5	87	0.10	2	2	high	impact
30.5	87	0.10	2	2	high	impact
22.5	87	2.69	3	3	low	static
22.5	87	8.69	3	3	low	static
22.5	87	5.44	3	3	low	static
22.5	87	11.44	3	3	low	static
22.5	87	10.06	3	3	low	static
22.5	87	4.06	3	3	low	static
22.5	87	0.10	3	3	low	impact
22.5	87	0.10	3	3	high	impact

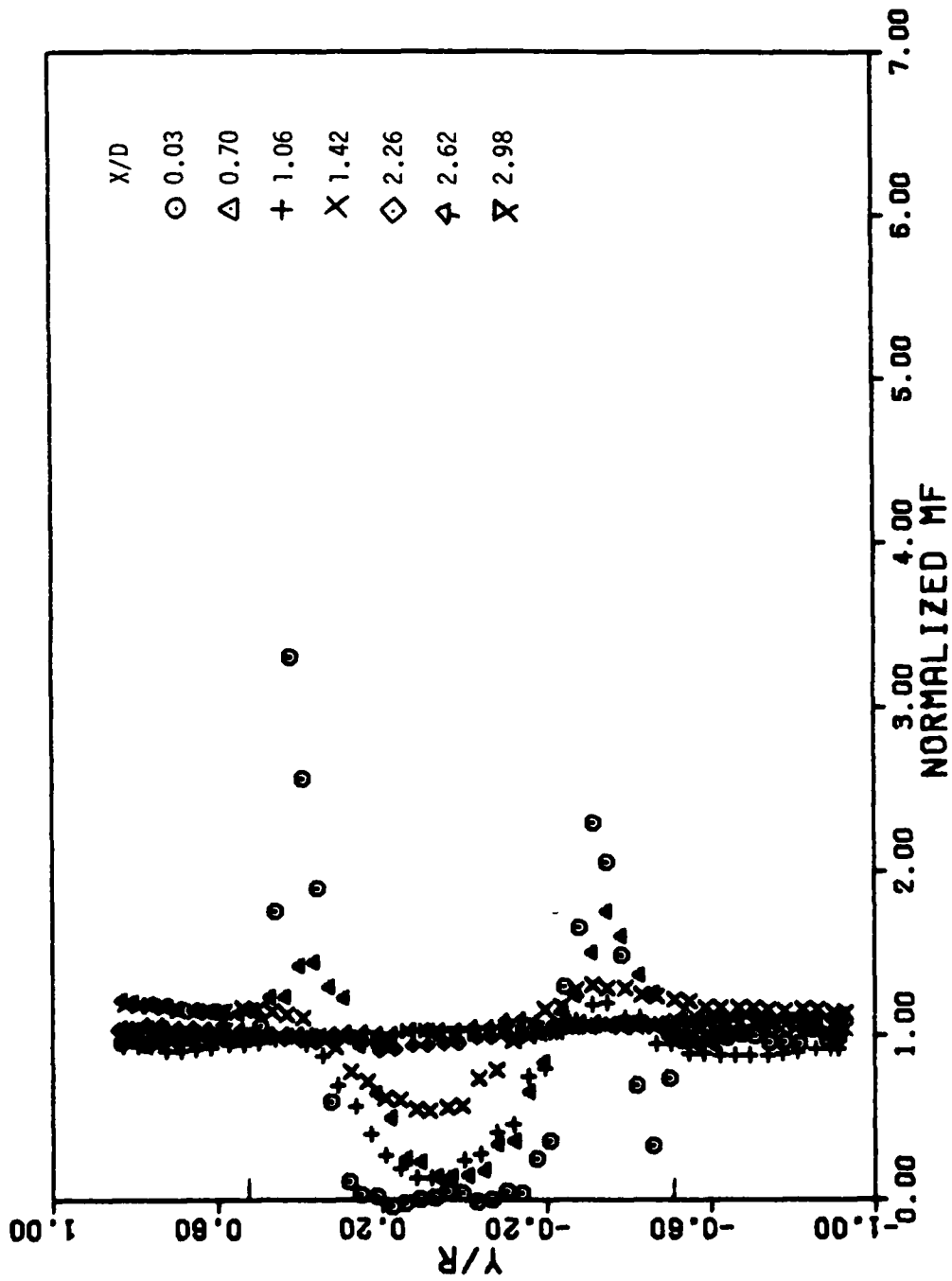


Fig. 2. Radial profiles of Normalized Argon Mole Fraction for  
 $D_1 = D^* = 2.0$  in.,  $P_{0A} = 30.5$  psia and  $P_{0F} = 87$  psia.

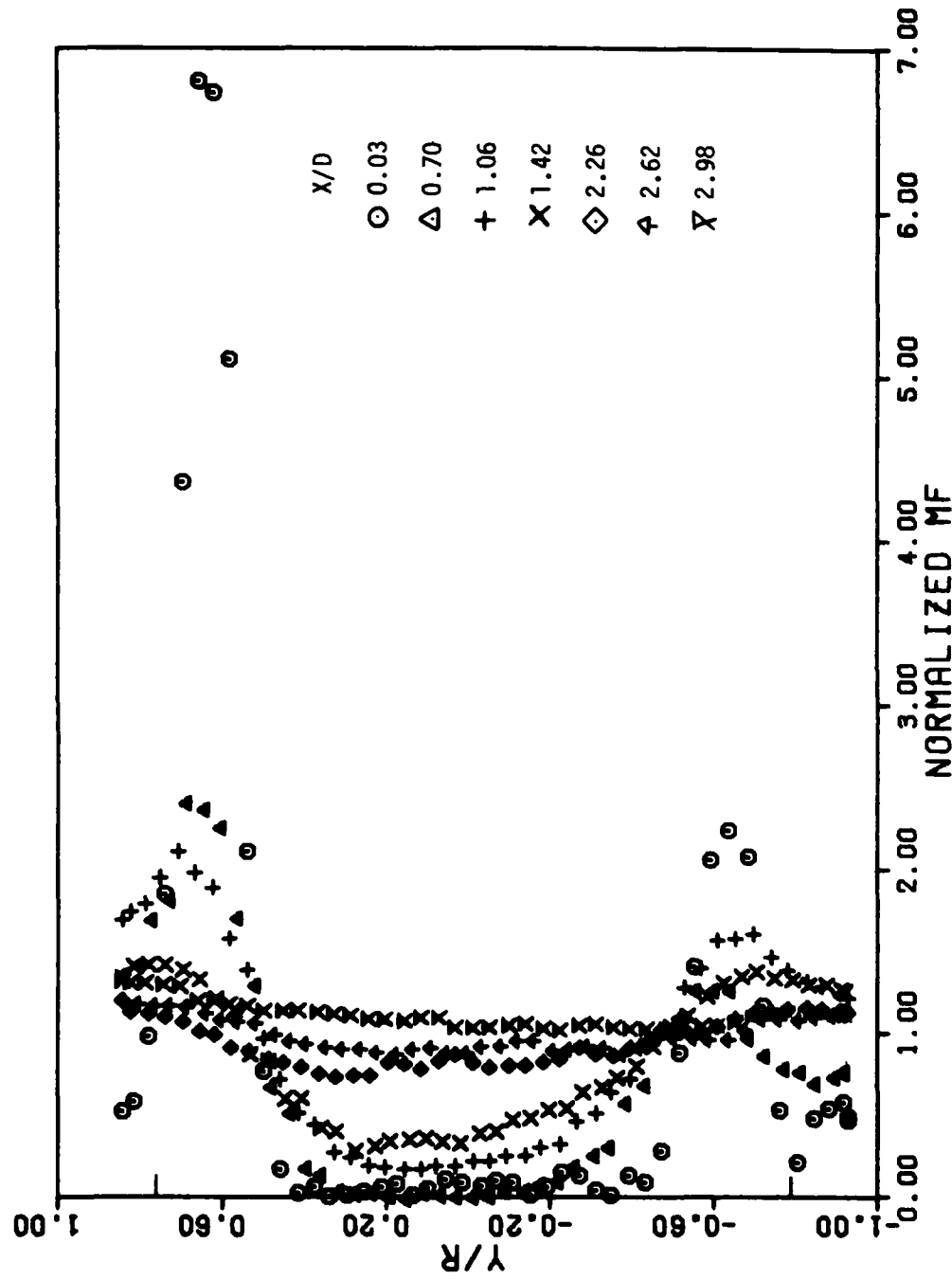


Fig. 3. Radial profiles of Normalized Argon Mole Fraction for  $D_1 = D^* = 3.0$  in.,  $P_{OA} = 22.5$  psia and  $P_{OF} = 87$  psia.

only 22.5 psia, owing to limited air supply capability. The sampling in both cases was with a side-orifice (that is, static pressure type) sampling probe in all locations except at  $X/D = 0.03$  ( $X$  is the distance between the sampling orifice and the sudden expansion step, while  $D$  is the diameter of the ramjet combustor, 3.84 in.). At this position, an impact probe was used since this was the only type which would permit access from the wall window. The argon concentration measurements were made in the horizontal plane of symmetry of the dump combustor, and two of the eight fuel injections lie in this plane.

It is clear from both Figures 2 and 3 that the argon concentration approaches that characteristic of uniform or complete mixing as  $X/D$  increases. However, it is seen that while uniform mixing is achieved at  $X/D = 2.26$  for the configuration with the 2 in. inlet, this condition is attained at  $X/D = 2.98$  for the 3 in. inlet configuration. However, it must be noted that the air inlet pressures (POA) were different in the two cases reported here.

For a given  $X/D$  value at which complete mixing has not yet been attained, the normalized argon mole fraction profile is generally characterized by two sharp peaks and a relatively flat valley in the vicinity of the combustor center line (that is, at  $Y/R = 0$ , where  $Y$  is the radial distance from the center line, and  $R$  is the radius of the combustor). The distance between these two peaks generally corresponds to the diameter of the inlet section ( $D_I$ ). The relative heights of these two peaks are different and this is a reproducible observation.

The typical argon mole fraction profiles such as shown in Figures 2 and 3 generally confirm the conclusions of other flowfield analyses, in which the flowfield was found to consist of three distinctively different fuel-air mixing (6) regions. The first region is the inner core inviscid flow region which corresponds to the region between the two sharp peaks in Figures 2 and 3. Within this region, the argon mole fraction profile shows a sharp decay which is characteristic of pure diffusion mixing. The second flowfield region is a shear flow region which

corresponds to the outer slope of the peaks in Figures 2 and 3. Within this region, fuel-air mixing is controlled by both diffusion and shear flow. The third flowfield region, the recirculation region, lies in the outer ring near the combustor wall. Within this region, the argon concentration profile appears to be flat and is thus characterized by vigorous flow recirculation mixing.

Fig. 4 shows the axial distribution of the normalized centerline argon concentration for the experimental configuration utilizing the two inlets mentioned above and also for an inlet used in the earlier work. The data plotted in Fig. 4 shows that of an air inlet pressure of 30 psia and an argon inlet pressure of 87 psia, the smaller inlet (that is,  $D_I = D^* = 2$  in.) gives better mixing compared to the larger inlet ( $D_I = D^* = 2.5$  in.). However, direct comparison of these data with that for the 3 in. inlet cannot be made, since a different air inlet pressure ( $POA = 22.5$  psia) was employed in the latter case.

Toward the end of the present contracting period, the dump combustor was converted into a dual inlet ducted rocket configuration.

A photograph of this new combustor configuration is shown in Fig. 5. This combustor consists of a mixing chamber, previously employed, and a new air inlet section, mounted in a rotatable fashion in front of the mixing chamber. The air inlet section has two side air inlet ports positioned 90 degrees apart. The conduits leading into these two ports have either circular or rectangular cross sections, but the same cross sectional area. An end plate is mounted on the front end of the air inlet section. An argon injection port is positioned on this end plate, located along the axis of the combustor.

In order to facilitate monitoring of the fuel/air mixing profile in the air inlet section of the combustor, a set of sampling probes was fabricated. These probes are mounted on the existing windows located on the mixing chamber, (as was the case with other previously used probes) but as many as four additional sections can be added to the front end of the probes in order to extend the

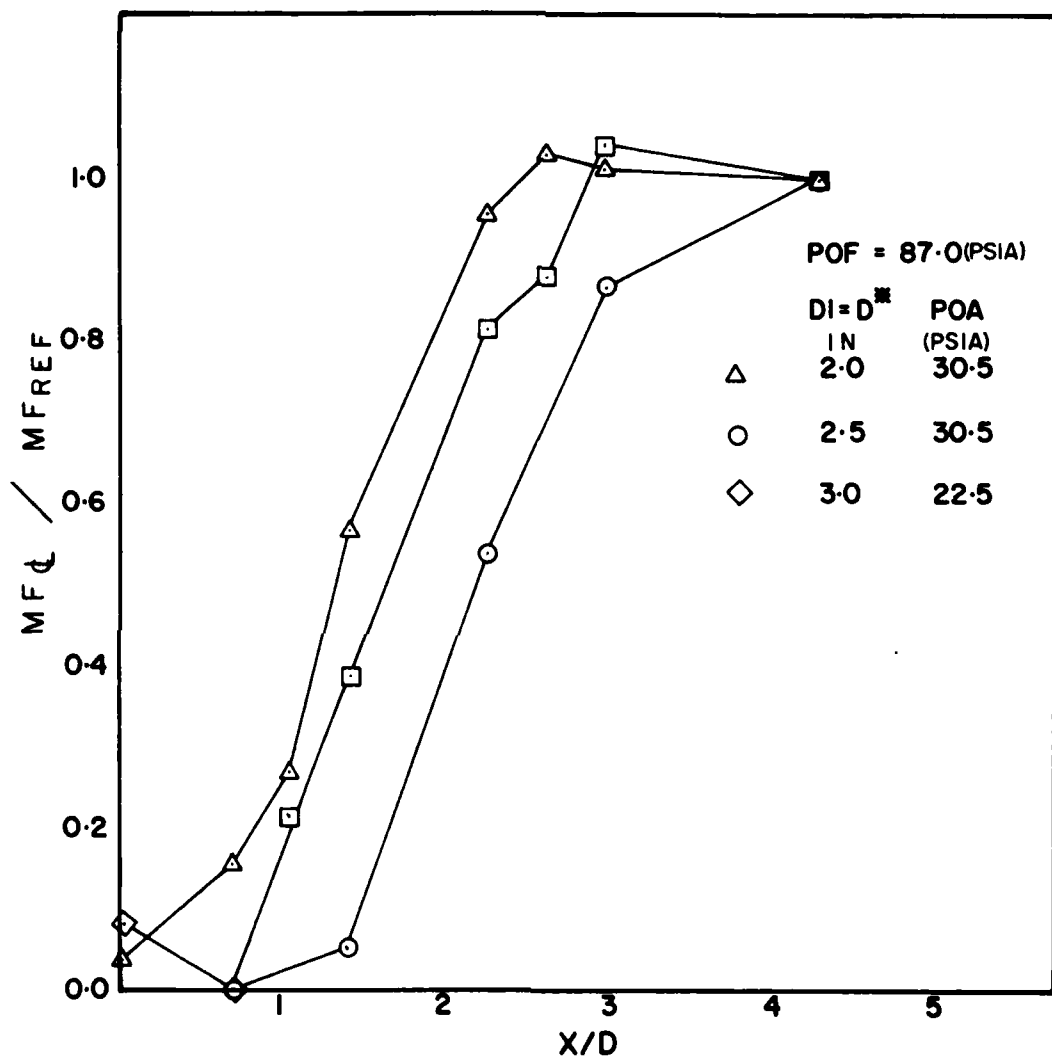


FIGURE. 4. NORMALIZED ARGON CONCENTRATION RESULTS

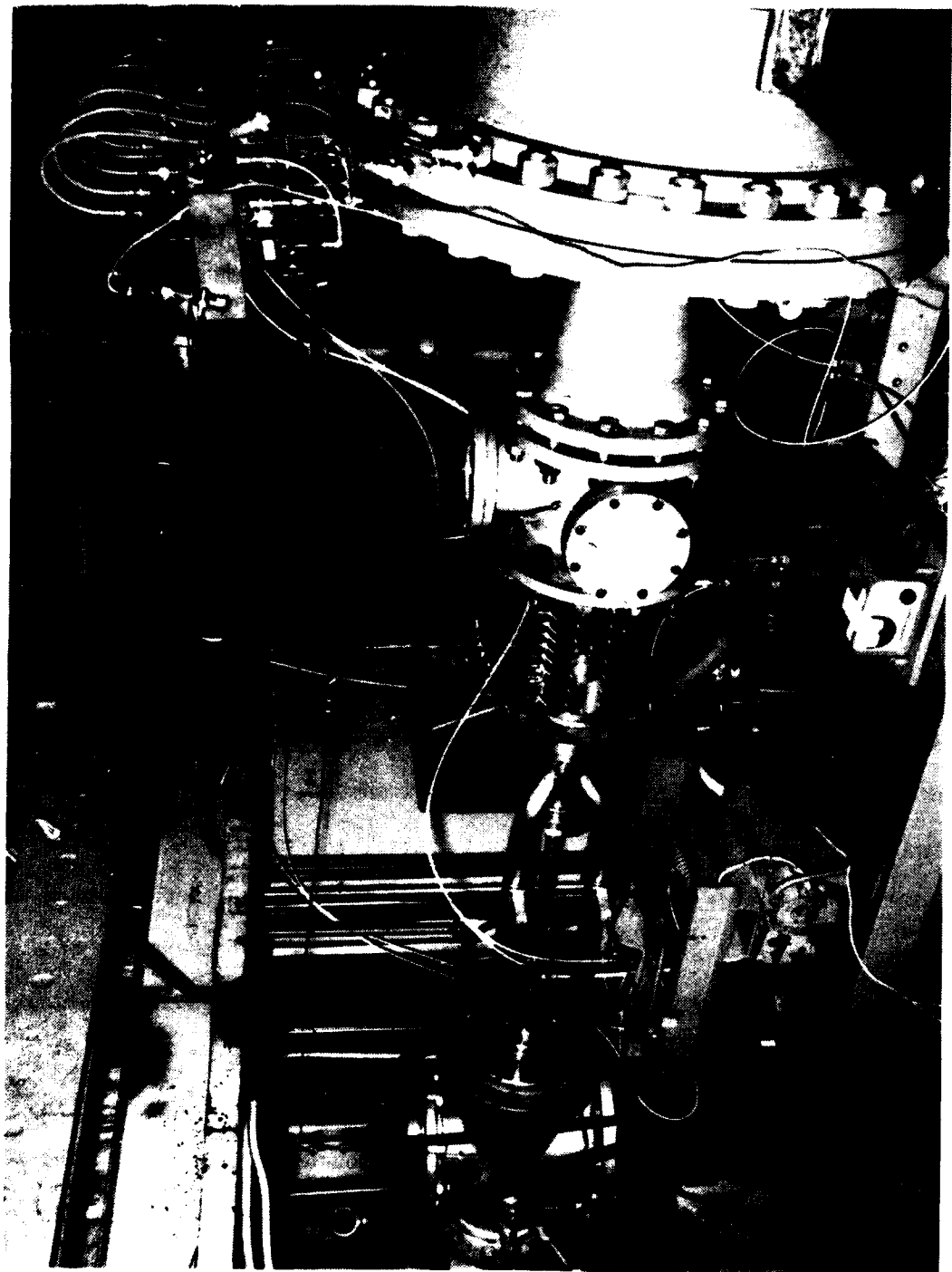


Figure 5. Facility Photograph of the Dual Inlet Ducted Rocket Combustor.

sampling position well into the air inlet section. As with other probes utilized in this work, two types of probe tip geometry were employed with the new probes, both similar to the original probe design. One of the new probes constructed is a total pressure sampling probe, having a sampling aperture, 0.020 in. in diameter, located at the front end of the probe. The second type of probe constructed is a static pressure sampling probe, having four orthogonal sampling apertures (each 0.010 in. diameter) on the probe body.

Table II lists the measured argon/air mixing data obtained for the dual inlet ducted rocket combustor with the circular inlet conduits. A few tests were also conducted for the combustor with the rectangular inlet conduits. Analysis of all these data is still in progress. In view of the complexity of this combustor configuration, more sampling tests will still be required to fully characterize the flowfield.

### III. DEVELOPMENT OF METHODOLOGY FOR MONITORING GASEOUS SPECIES IN REACTIVE COMBUSTION ENVIRONMENTS

This section describes the development of methodology for monitoring several compounds of interest in the active combustion environment, including  $O_2$ ,  $CO$ ,  $CO_2$ ,  $H_2O$ , and hydrocarbon compounds. This work entailed preparation of various gas standard mixtures, covering an appropriate range of concentrations, determination of the most suitable mass spectrometric peaks to be monitored and the procedures to be employed for detection of the components of each standard mixture to be detected, and finally, determination of the mass spectrometer signal response for these components over a wide range of mixture concentrations. The significance of possible interferences from other compounds which are expected to be present during a typical combustion experiment was also accessed.

Preliminary work on the tasks just described was accomplished under the previous research effort (11). A gas calibration system (Fig. 6), which was required in

Table II  
Measured Argon/Air Mixing Data

<u>Probe Position</u> <u>x(in)</u>	<u>Air Pressure</u> <u>POA (psia)</u>	<u>Ar Pressure</u> <u>POF (psia)</u>	<u>Probe</u>	<u>Integration</u> <u>Speed</u>
18.25	35.5	136	static	Low
18.25	40.5	190	static	Low
18.25	40.5	130	static	Low
18.25	30.5	130	static	Low
12.25	35.5	130	static	Low
12.25	40.5	200	static	Low
12.25	40.5	130	static	Low
12.25	30.5	130	static	Low
12.25	35.5	90	static	Low
12.25	40.5	90	static	Low
9.5	40.5	200	static	Low
9.5	40.5	130	static	Low
9.5	40.5	90	static	Low
9.5	35.5	130	static	Low
9.5	35.5	90	static	Low
9.5	30.5	130	static	Low
9.5	30.5	90	static	Low
15.5	40.5	200	static	Low
15.5	40.5	130	static	Low
15.5	40.5	90	static	Low
15.5	35.5	130	static	Low
15.5	35.5	90	static	Low
15.5	30.5	130	static	Low
15.5	30.5	90	static	Low
15.5	40.5	195	static	Low
15.5	40.5	130	static	Low
15.5	40.5	90	static	Low
15.5	35.5	130	static	Low
15.5	35.5	90	static	Low
15.5	30.5	130	static	Low
9.31	40.5	200	static	Low
9.31	40.5	130	static	Low
9.31	40.5	90	static	Low
9.31	35.5	130	static	Low
9.31	35.5	90	static	Low
9.31	30.5	130	static	Low
9.31	30.5	90	static	Low
8.31	40.5	200	static	Low
8.31	40.5	130	static	Low
8.31	40.5	90	static	Low
8.31	35.5	130	static	Low
8.31	35.5	90	static	Low
8.31	30.5	130	static	Low
8.31	30.5	90	static	Low
6.31	40.5	200	total	high

Table II (Cont.)

Probe Position X(in)	Air Pressure POA (psia)	Ar Pressure POF (psia)	Probe	Integration Speed
6.31	40.5	130	total	high
6.31	40.5	90	total	high
6.31	35.5	130	total	high
6.31	35.5	90	total	high
6.31	30.5	130	total	high
6.31	30.5	90	total	high

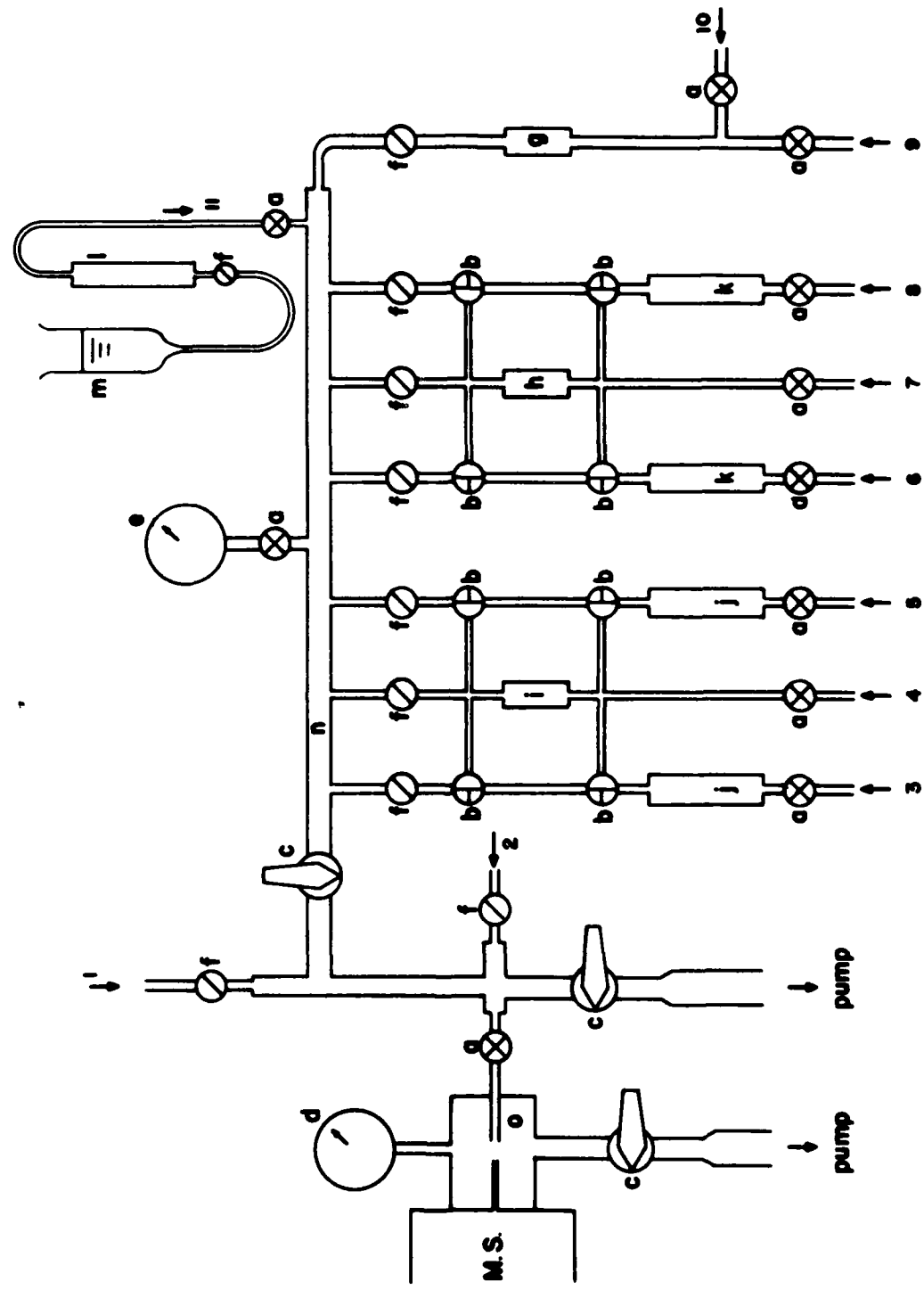


Figure 6 Schematic Diagrams of the Gas Calibrations Systems

LEGENDS FOR FIGURE 6

<u>Legend</u>	<u>Item Designated</u>
a	on-off valve
b	three-way valve
c	ball valve
d	pressure gauge (0-50 torr)
e	pressure gauge (0-300 torr)
f	metering valve
g	linear mass flow meter (0-10,000 SCCM)
h	linear mass flow meter (0-1,000 SCCM)
i	linear mass flow meter (0-100 SCCM)
j	rotometer (4-166 SCCM, air)
k	rotometer (20-859 SCCM, air)
l	rotometer (0.003-1.4 cc/min, water)
m	water reservoir
n	manifold
o	prechamber
1.	existing combustor gas inlet.
2.	existing compressed air inlet.
3.	nitrogen dioxide gas inlet
4.	carbon monoxide gas inlet
5.	nitric oxide gas inlet
6.	carbon dioxide gas inlet
7.	fuel and carbon dioxide standard mixture inlet

LEGENDS FOR FIGURE 6 (Continued)

<u>Legend</u>	<u>Item Designated</u>
8.	fuel gas inlet
9.	oxygen gas inlet
10.	auxiliary gas inlet
11.	water inlet

connection with these monitoring studies, was designed and constructed and was demonstrated to function satisfactorily. A detailed description of this calibration system was presented earlier (11). This system can be utilized to prepare a gas mixture consisting of as many as eight different gaseous components. The flow rate of each gaseous component entering the central manifold is separately controlled by a metering valve, and is measured by a flow meter. The composition of the final gas mixture is thus readily determined. The prepared mixture is then admitted to the mass spectrometer via the gas inlet system. This permits rapid calibration of the mass spectrometer (that is, determination of the signal response for a given quantity of gas introduced) for any gases to be monitored.

In the course of the previous contractual effort, the preliminary procedures for monitoring selected gases of interest were also developed. Calibration data and coefficients were obtained for the gases methane, carbon dioxide, and oxygen. These results generally established the methodology required for the monitoring of those gaseous species. However, more elaborate calibration tests were still necessary because the calibration tests are quantitatively significant only when the gases are sampled under conditions closely approximating those of actual combustion tests. The latter conditions are realized by sampling a flame, or an actual combustion device. The sampling conditions to be employed in such tests are largely dependent on the design of the combustion facilities and the sampling probes utilized, both of which have been addressed in the course of the present program.

#### A. Development of Monitoring Methodology for H<sub>2</sub>O

Development of sampling techniques and preliminary calibration measurements for monitoring water (H<sub>2</sub>O) were also undertaken during the earlier contract effort. Only limited success was realized in these earlier experiments, however, with the previously employed experimental arrangement, water was supplied from a pressurized reservoir in liquid form (Fig. 6, item m). The water passed through a flow meter, and then was injected into the air stream in a manifold which was

heated to 230°C. The injected water was expected to vaporize within this manifold, which is attached to the mass spectrometer ion source inlet. The main problem encountered during these earlier tests was that the intensity of the mass spectrum being monitored as an indicator of the  $\text{H}_2\text{O}^+$  concentration ( $\text{H}_2\text{O}^+$ ,  $m/e = 18$ ) was found to fluctuate excessively, for any of the water flow rates utilized. This was a clear indication that the water introduced did not vaporize in a continuous manner, in spite of the relatively high temperature at which the walls of the manifold were maintained. During the present contractual period a completely new experimental approach was devised and implemented, and was shown to be effective.

Fig. 7 shows a schematic diagram of the newly designed water inlet system which incorporates an oven. The temperature of this oven can be maintained at 145°C. Located within this oven are a water reservoir (item c), three copper coils and several additional heating units. During a test, a stable stream of nitrogen gas, at a flow rate of 1000 SCCM, is allowed to mix with a stream of water vapor, the flow rate of which is regulated by a metering valve (item b in Fig. 7), which is also located within the oven. The resulting Nitrogen/water mixture is introduced into the mass spectrometer, which is adjusted to detect the intensities of the  $\text{H}_2\text{O}^+$  ( $m/e = 18$ ) and  $\text{N}^+$  ( $m/e = 14$ ) ions, alternately. Precautions were taken to prevent any premature condensation of water vapor in the transfer line. In one test, the ratio of the intensities of the  $\text{H}_2\text{O}^+$  and  $\text{N}^+$  ions was continuously monitored for a period of 30 minutes. The precision of the ratio of the measured ion intensities was  $3.94 \pm 0.01$ , which clearly demonstrates the excellent stability of the water flow rate which is achieved with the new experimental arrangement.

In the present tests, the water flow rate was determined by weighing the condensed water collected within a cold trap (item g, Fig. 7) during a period of 30 minutes. Careful design of the trap configuration was required in order to

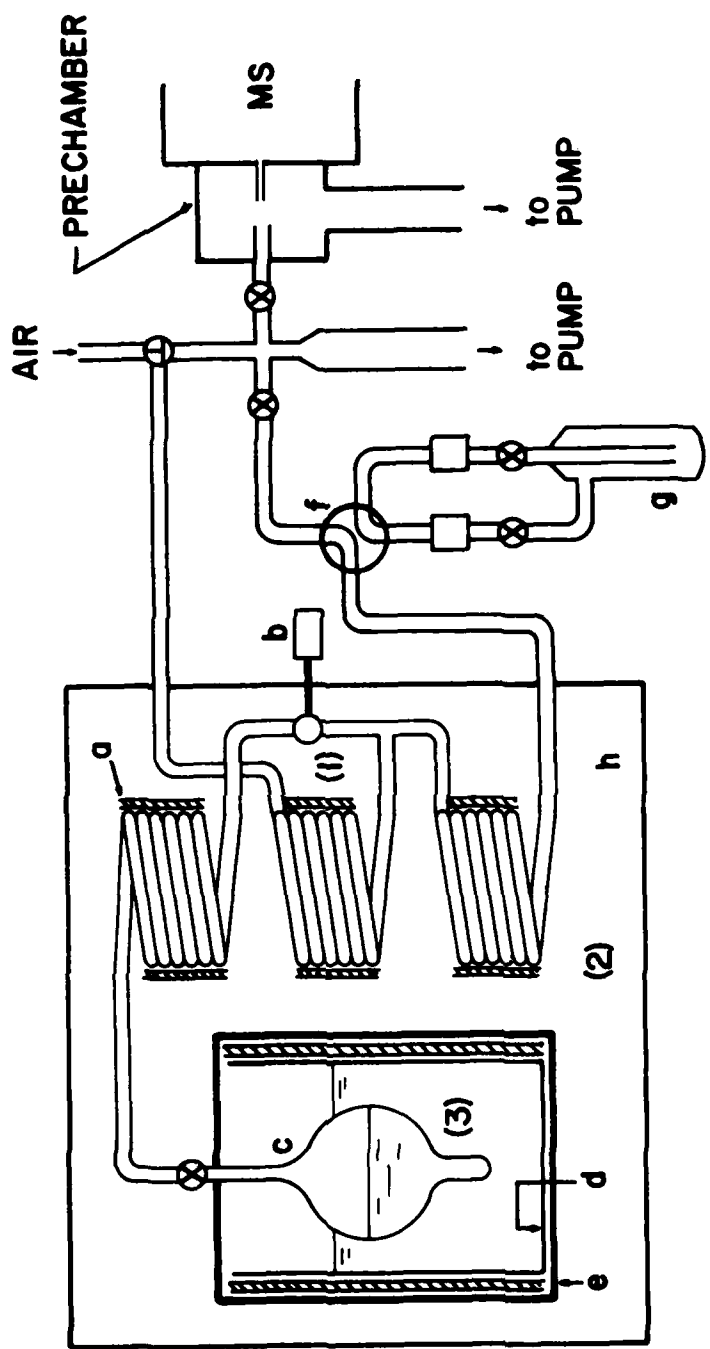


Figure 7. Schematic Diagram of the Water Inlet System for Calibration Applications.

**Legends For Figure 7.**

- a. Heating tape: one on each copper coil, and the beaker d.**
- b. Metering valve whose stem is extending outside of the oven.**
- c. Water reservoir.**
- d. Beaker containing low vapor pressure fluid.**
- e. Asbestos layer.**
- f. Four-way valve.**
- g. Detachable cold trap.**
- h. Oven.**

**1, 2, and 3 designate position where temperature is measured.**

- 1. Metering valve wall.**
- 2. Oven.**
- 3. Water reservoir wall.**

ensure that all of the water vapor (more than 99%) was condensed within the trap, while not altering the total flow rate of the nitrogen/water mixture, which could result from constriction due to formation of ice on the trap surfaces.

The results of the present calibration tests are shown in Fig. 8, which presents a plot of the ion intensity ratio  $[(I_{18} - (I_{18})_0) / (I_{14} - (I_{14})_0)]$  as a function of the flow rate ratio,  $[FR]_{H_2O} / [FR]_{N_2}$ , at a given mass spectrometer setting. The plot is clearly linear over the entire experimental range, with a slope corresponding to,

$$\frac{I_{18} - (I_{18})_0}{I_{14} - (I_{14})_0} = 11.69 \frac{[FR]_{H_2O}}{[FR]_{N_2}} \quad (1)$$

or,

$$\frac{I_{18} - (I_{18})_0}{I_{28} - (I_{28})_0} = 0.658 \frac{[FR]_{H_2O}}{[FR]_{N_2}} \quad (2)$$

for the case where  $N_2^+$  (m/e = 28) is used as the reference ion. The largest experimental error in the calibration process described above arises from the weighing of the trapped water, which is accomplished with a triple-beam balance.

Again, it should be emphasized that the results presented here were obtained solely for the purpose of developing appropriate methodology. Quantitative calibration pertinent to the determination of the water concentration in an actual flow environment must be accomplished under conditions corresponding to those of actual sampling of the flame or the combustion flowfield of interest. Some problems relating to these tasks will be discussed in a later section of this report.

B. Development of Quantitative Calibration Procedures for the Determination of the Concentrations of Gaseous Species in the Combustion Flame.

At this point, development of the methodology for monitoring gaseous species of interest in the active combustion environments has been essentially completed,

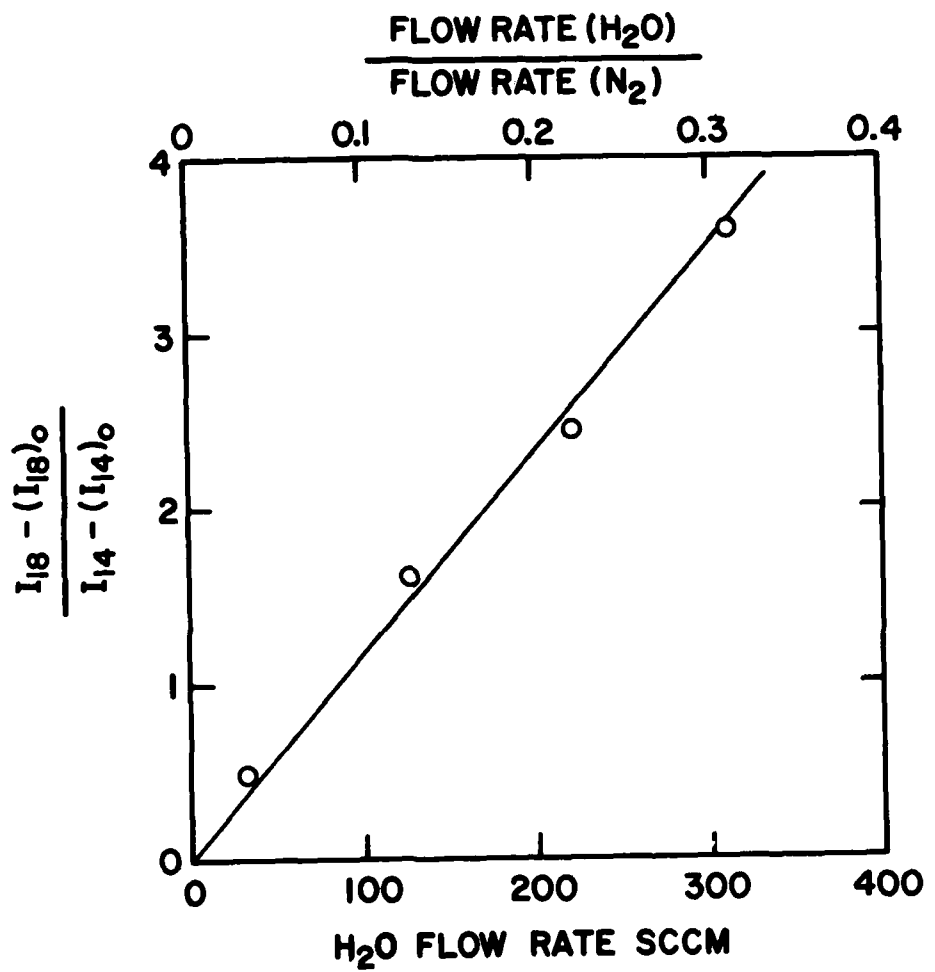


Figure 8. Plot of the ion intensity ratio  $[I_{18} - (I_{18})_0]/[I_{14} - (I_{14})_0]$  vs. the flow rate ratio  $[FR]_{\text{H}_2\text{O}}/[FR]_{\text{N}_2}$ .

as described above. However, as emphasized in the foregoing discussion, in order to obtain quantitatively significant calibration values, the experimental conditions prevailing during the calibration tests must be the same as those for the actual combustion environment to be sampled. The combustion environments of interest in the present project are those which prevail in a flame and in a ramjet combustor. Progress achieved in the present study in the development of quantitative calibration procedures for sampling a flame will now be presented.

All of the calibration results reported in this section were obtained with a flat flame burner which was constructed during the present contractual period. A detailed description of this burner will be presented in a later section. The discussion here will deal only with the quantitative aspects of calibration for this burner.

The experimental conditions described here generally refer to the operating conditions of 1) the flame burner, including the flow rate of the fuel and air, the burner pressure, burner head design, etc.; 2) the sampling probe, including the probe material, probe orifice size, position of the probe relative to the burner head; 3) interface design, such as direct/indirect interface, transfer line temperature, valve settings, etc.; and 4) the mass spectrometer, including its ion lens settings, electron multiple voltage and the ion source pressure. It is conceivable that at least some of these experimental parameters may affect the results of the quantitative calibration. Therefore, it is important that for each calibration test all of these experimental parameters be well defined. Furthermore, it is anticipated that future flame sampling studies will be conducted under a variety of experimental conditions, including several different gaseous flow rates and burner pressures, use of different sampling probe designs, and so on. The effect of these variables on the accuracy of the calibration must also be evaluated.

During a typical flame sampling test, it is expected that more than one

species will be monitored simultaneously. The previously employed data acquisition routine in which only one sample species is monitored along with a reference gas is no longer suitable. A new computer program for data acquisition and reduction was therefore written. With this program, five sample ions and one reference ion, at a maximum, are monitored sequentially. During the period of monitoring each ion, which typically lasts for one second, a small window covering the ion peak region is scanned and integrated. One complete set of data is obtained in six seconds, or less, if a lesser number of ions are monitored. Prior to actual sampling, a background scan is accomplished to obtain the background signal for each ion channel. Operation of this program allows the proper ion intensity ratio  $I_i - (I_i)_0 / I_{ref} - (I_{ref})_0$  ( $i = 1-5$ ) to be calculated. For a typical run, which lasts for one minute, a total of ten complete cycles are executed. The program automatically calculates the average of the ion intensity ratio for each ion channel and its standard deviation.

Since the ion signal line is branched into two amplifiers having different gains for A/D conversion, the dynamic range of the ion intensity is expanded by a factor of ten. This is necessary since ions of drastically different intensity levels are frequently to be monitored. The necessary conversion between these two channels' data is also properly processed by this program. Signals corresponding to the ion mass, source pressure, and flow rates of various gases are also acquired, the background is subtracted, and the data reduced with this new program.

It was discovered in the course of these studies that for monitoring of some extremely small ion signals, such as the  $C^+$  ion from  $CO$ , the detection accuracy achieved is severely distorted by random baseline drift, which is probably associated with the instability of the amplifier circuit. Unfortunately, this baseline drift cannot be properly corrected by the new data processing program just described. In view of this difficulty, a second new computer program had

to be devised. This program specifically designates one ion channel for monitoring the magnitude of the baseline signal, which is then subtracted from the sampled ion signal before any further calculations. The error due to this random baseline drift can thus be eliminated. However, it does suffer one disadvantage in that only four sample ions at most can be monitored with this arrangement, which may prove to be insufficient for future applications.

### 1. Parametric Study

As stated previously, it is anticipated that future flame sampling experiments may be conducted under a variety of experimental conditions. This requires that the calibration tests also be conducted under these same experimental conditions, since these variations may affect the calibration results. Therefore, the first task carried out was a parametric study in which the effect of each variable experimental parameter on the calibration results was evaluated.

Table III shows the results of this study, in which the values of four parameters, that is, ion source pressure, electron multiplier voltage, burner pressure, and the position of the probe were varied. During each individual test, a mixture of air, methane and carbon dioxide of known composition was introduced into the burner, for which the pressure was regulated at a given pressure, as indicated. A quartz sampling probe which has an inlet orifice of 0.005 in. diameter was placed within the burner at a preselected distance relative to the base of the burner head, as indicated by the dial indicator. All of the interface lines connecting the probe and the mass spectrometer inlet were heated with heating tapes and maintained at a temperature of 150°C. In view of the limited quantity of gas sampled, a direct interface was employed, the details of which were described in the previous report. The ion source pressure was precisely controlled by a metering valve.

During each mass spectrometric sampling test, the first four channels of the mass programmer were tuned to the m/e 15 ( $\text{CH}_3^+$ ), 28 ( $\text{N}_2^+$ ), 32 ( $\text{O}_2^+$ ) and

TABLE III  
Effects of Experimental Conditions on  
Observed Ion Intensity Ratios

Ion Source Ion Source press (torr)	Elect. Mult. Voltage (v)	Burner Press (torr)	Probe <sup>2</sup> Position (in)	$\frac{I_{32} - (I_{32})_0}{I_{28} - (I_{28})_0}$	$\frac{I_{15} - (I_{15})_0}{I_{28} - (I_{28})_0}$	$\frac{I_{44} - (I_{44})_0}{I_{28} - (I_{28})_0}$
$0.5 \times 10^{-5}$	2000	100	0	0.2145	0.01342	0.06594
	"	"	0.857	0.2164	0.01375	0.06899
	"	"	1.765	0.2162	0.01385	0.06797
$0.5 \times 10^{-5}$	2000	400	0	0.2163	0.01393	0.06976
	"	"	0.857	0.2164	0.01393	0.06948
	"	"	1.765	0.2150	0.01408	0.06801
$1.0 \times 10^{-5}$	1800	100	0	0.2257	0.01385	0.07070
	"	"	0.857	0.2243	0.01375	0.06951
	"	"	1.765	0.2253	0.01377	0.06927
$1.0 \times 10^{-5}$	1800	400	0	0.2252	0.01388	0.07095
	"	"	0.857	0.2242	0.01394	0.07056
	"	"	1.765	0.2249	0.01409	0.06857
$2.0 \times 10^{-5}$	1600	100	0	0.2413	0.01438	0.06885
	"	"	0.857	0.2396	0.01416	0.07217
	"	"	1.765	0.2391	0.01385	0.07137
$2.0 \times 10^{-5}$	1600	400	0	0.2428	0.01425	0.07175
	"	"	0.857	0.2408	0.01439	0.07339
	"	"	1.765	0.2399	0.01454	0.07098

1. The listed ratios are for a normalized flow rate of Air of 2000 SCCM, flow rate of CH<sub>4</sub> of 335 SCCM and flow rate of CO<sub>2</sub> of 70 SCCM.

2. Distance between the probe tip and the burner surface.

44 ( $\text{CO}_2^+$ ) ions, respectively. The acquired ion signals were reduced to the ion intensity ratios  $\frac{I_{32} - (I_{32})_0}{I_{28} - (I_{28})_0}$ ,  $\frac{I_{15} - (I_{15})_0}{I_{28} - (I_{28})_0}$ , and  $\frac{I_{44} - (I_{44})_0}{I_{28} - (I_{28})_0}$ , using the newly devised program. Each of the ratios listed in the table is an average of ten individual measurements with standard deviation typically in the range of  $\pm 0.5\%$ .

It is seen from Table III that, for a given ion source pressure and electron multiplier voltage setting, the observed ion intensity ratio is constant regardless of the burner pressure or the position of the probe. This indicates that the mixing of the air/ $\text{CO}_2/\text{CH}_4$  mixture is complete as the gas reaches the burner head. Furthermore, there is no appreciable effect on the calibration results due to the variation of the gas velocity (which is varied along the burner axis) or the burner pressure around the probe sampling site. This finding substantially simplifies the calibration procedure, since the calibration test will be necessary for only one sampling condition, and the results of this test will also be applicable for other conditions without appreciable error.

However, the ion intensity ratios presented in Table III are seen to vary somewhat (5-10%) as the ion source pressure increases from  $0.5 \times 10^{-5}$  torr to  $2 \times 10^{-5}$  torr, and the electron multiplier voltage is decreased from 2000 volts to 1600 volts. In a strict sense, then, any burner calibration which is conducted at a given ion source pressure and electron multiplier setting is only applicable for burner sampling at that specified ion source pressure and electron multiplier setting. Additional calibration tests must be conducted if these two experimental parameters are to be varied during future sampling tests.

2. Individual Gas Calibration. Reported here are the results of calibration tests accomplished for each gaseous species of interest in the flame combustion environment. The basic calibration methodology for most of these gases has been developed and documented previously (11).

The experimental procedures employed here are also similar to those reported previously, except that all the calibration tests described here were conducted

under flame sampling conditions such that the observed calibration results are directly applicable for the measurement of the concentrations of gaseous species in the flame sampled.

The experimental conditions chosen for these individual gas calibration tests are generally the same as those described in the parametric study. The burner pressure was maintained at 400 torr and the sampling probe (QP-III) was placed at a position 0.857 inches above the burner head. The ion source pressure was always held at  $1.0 \times 10^{-5}$  torr. However, several different electron multiplier voltage settings were utilized to permit detection of several different ions having large intensity differences. Since these voltage settings will affect the calibration results, as discovered in the previous study, all of the derived calibration constants are applicable only for the flame sampling experiments conducted with the same specified multiplier voltage settings.

In the present calibration tests, the possibility of interferences for each gas to be calibrated was also taken into consideration. If the possibility does exist that any other gaseous species found in a flame combustion environment may interfere with the detection of a given gas to be monitored, these interfering gases must also be introduced into the flame burner along with the gas to be evaluated during the calibration tests. Proper methodology must then be devised such that the ion signals contributed by the interfering gases can be separated from the true signal indicating the concentration level of the calibrated gas.

a. Methane. The calibration for methane is relatively simple, and the methodology has been well established as described in the previous report(11). The formula relating the relative sensitivity factor for the formation of  $\text{CH}_3^+$  ion from  $\text{CH}_4$ ,  $k(\text{CH}_3^+/\text{CH}_4)$ , is as follows:

$$\frac{I_{15} - (I_{15})_0}{I_{40} - (I_{40})_0} = \frac{1}{0.00934} \frac{k(\text{CH}_3^+/\text{CH}_4)}{k(\text{Ar}^+/\text{Ar})} \frac{[(\text{FR})_{\text{methane}}]}{[(\text{FR})_{\text{air}}]} + \frac{0.78}{0.00934}$$
$$\frac{k(\text{N}_\text{15}^+/\text{air})}{k(\text{Ar}^+/\text{Ar})} \quad (3)$$

The above formula is accurate for a methane flame system, since  $N_2$  is the only known stable gas present in the methane flame that may interfere with the observed  $CH_3^+$  ion signal (owing to the formation of  $^{15}N^+$  ion, which has the same nominal mass as that of the  $CH_3^+$  ion).

During the calibration test, a stable flow of air at 2000 SCCM was mixed with a flow of methane for which the flow rate ranged from zero to 350 SCCM, and introduced into the flat flame burner. Subsequently, the mixture gas was sampled through the sampling probe and analyzed in the mass spectrometer, the electron multiplier being set at 1800 volts. Figure 9 shows a plot of the measured values of  $\frac{I_{15} - (I_{15})_0}{I_{40} - (I_{40})_0}$  as a function of  $\frac{[FR]_{methane}}{[FR]_{air}}$ , in which each data point represents an average of ten individual measurements. According to Eq. (3), the slope of this plot yields a value of 0.4577 for the relative sensitivity factor,  $\frac{k(CH_3^+/CH_4)}{k(Ar^+/Ar)}$ , which can be readily used for deriving the mole fraction ratio,  $\frac{(MF)_{methane}}{(MF)_{argon}}$ , during future flame sampling experiments. Apparently, the zero intercept indicates that the contribution of  $^{15}N^+$  is very small and can be ignored.

b. Carbon Dioxide. As is the case for methane, the calibration methodology for carbon dioxide has also been established previously, with the corresponding calibration formula given as follows:

$$\frac{I_{44} - (I_{44})_0}{I_{40} - (I_{40})_0} = \frac{1}{0.00934} \frac{k(CO_2^+/CO_2)}{k(Ar^+/Ar)} \frac{[(FR)CO_2]}{[(FR)Air]} + \frac{0.00033}{0.00934} \frac{k(CO_2^+/CO_2)}{k(Ar^+/Ar)} \quad (4)$$

Figure 10 shows the results of the calibration test, in which a steady flow of air at 2000 SCCM was mixed with a flow of carbon dioxide, with the flow rate ranging from zero to 350 SCCM, and subsequently introduced into the burner and sampled. The sampled gas was then analyzed by the mass spectrometer with the electron multiplier voltage was set at 1800 volts. The plot of the ion intensity

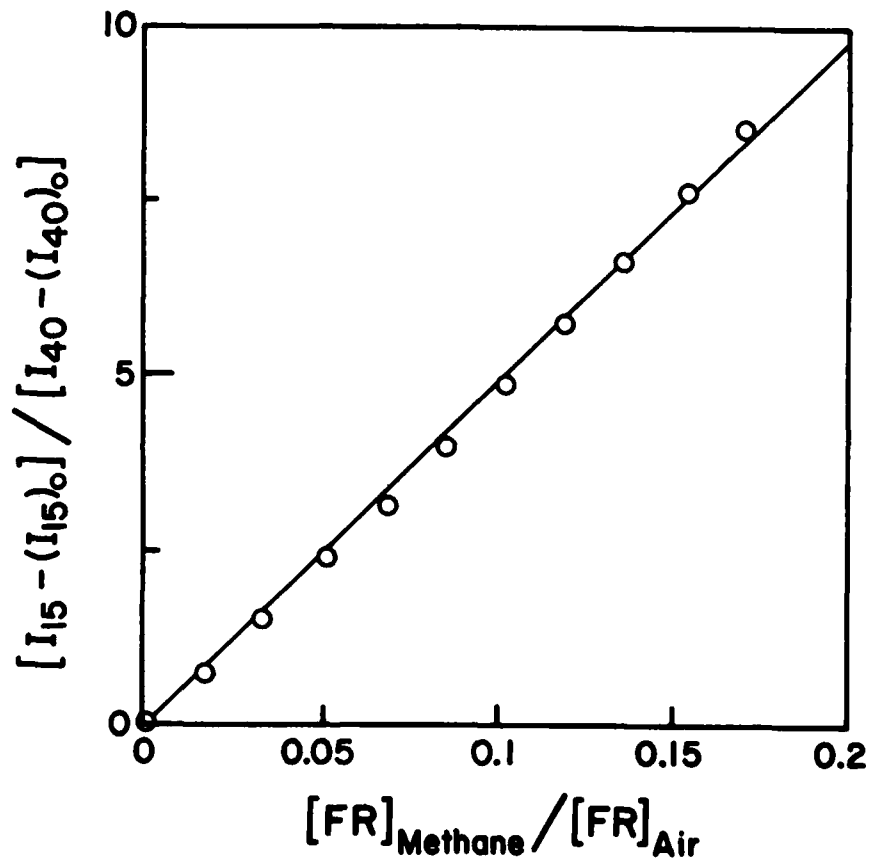


Figure 9. Plot of the relative ion intensity ratio  $[I_{15} - (I_{15})_0] / [I_{40} - (I_{40})_0]$  vs. the gas flow rate ratio  $[FR]_{\text{Methane}} / [FR]_{\text{Air}}$ .

ratio  $\frac{I_{44} - (I_{44})_0}{I_{40} - (I_{40})_0}$  vs the flow rate ratio  $\frac{(FR)CO_2}{(FR)Air}$ , shown in Figure 10, yields a slope which corresponds to the relative sensitivity factor,  $\frac{k(CO_2^+/CO_2)}{k(Ar^+/Ar)}$ , of 0.990.

No significant known interference exists for the present monitoring methodology except for the trace amount of natural  $CO_2$  present in the air which can be readily corrected for. Other minor interferences include nitrous oxide ( $N_2O$ ), which yields an ion,  $N_2O^+$ , of m/e 44. The natural abundance of  $N_2O$  in air is very low (<0.01%) and can be ignored. The formation of  $N_2O$  in a methane-air flame is also not very significant and can be ignored for the measurement of  $CO_2$  formation.

c. Oxygen. The present calibration involved the use of a mixture of oxygen, nitrogen, and argon, with the flow rate of each of these gases individually monitored and controlled. During this test, it was found that the oxygen source (a cylinder of  $O_2$ ) contains a trace amount of argon, whose concentration ( $x$ ) is unknown. To properly correct for this, the calibration formula previously developed should be modified and written as follows:

$$\frac{I_{40} - (I_{40})_0}{I_{32} - (I_{32})_0} = \frac{k(Ar^+/Ar)}{k(O_2^+/O_2)} \frac{[FR]Ar}{[FR]O_2} + x \frac{k(Ar^+/Ar)}{k(O_2^+/O_2)} \quad (5)$$

Figure 11 shows the results of the present calibration test which was conducted with the electron multiplier voltage set at 1800 volts. This plot of the ion intensity ratio,  $\frac{I_{40} - (I_{40})_0}{I_{32} - (I_{32})_0}$ , vs the flow rate ratio  $\frac{[FR]Ar}{[FR]O_2}$ , appears to be quite linear, the slope corresponding to a relative sensitivity factor,  $\frac{k(O_2^+/O_2)}{k(Ar^+/Ar)}$ , of 0.625.

d. Carbon Monoxide. A preliminary attempt at calibration for  $CO$ , based on the  $CO^+$  ion (m/e = 28), was conducted previously. Unfortunately, the experimental errors involved in this calibration proved to be too large to be acceptable

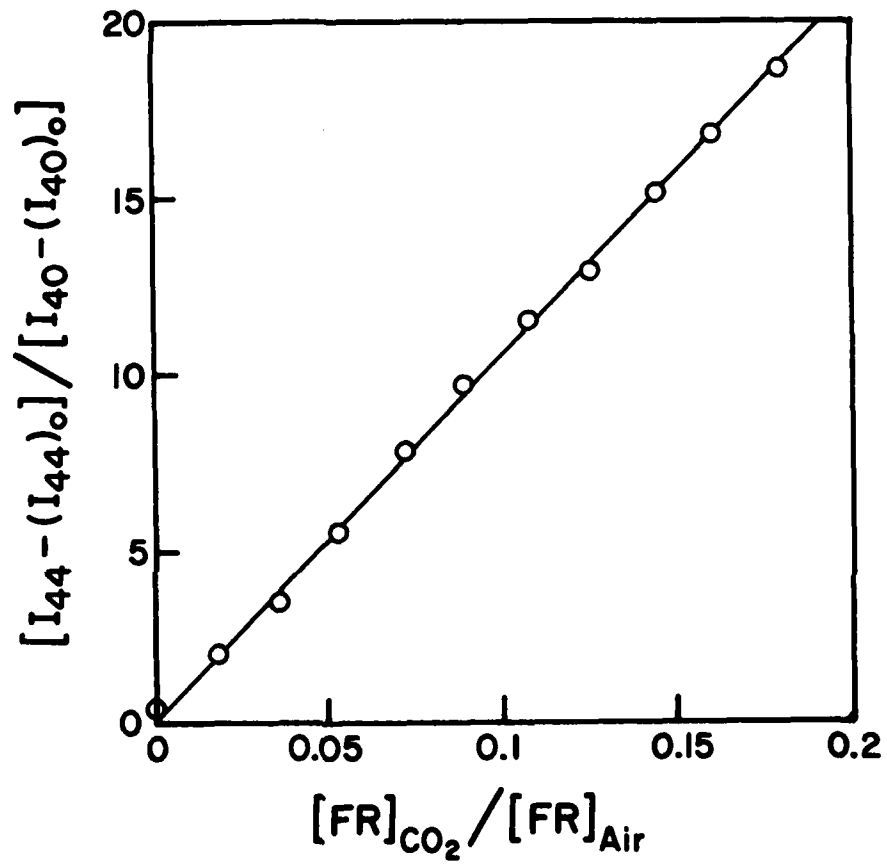


Figure 10. Plot of the relative ion intensity ratio  $[I_{44} - (I_{44})_0] / [I_{40} - (I_{40})_0]$  vs. the gas flow rate ratio  $[FR]_{CO_2} / [FR]_{Air}$ .

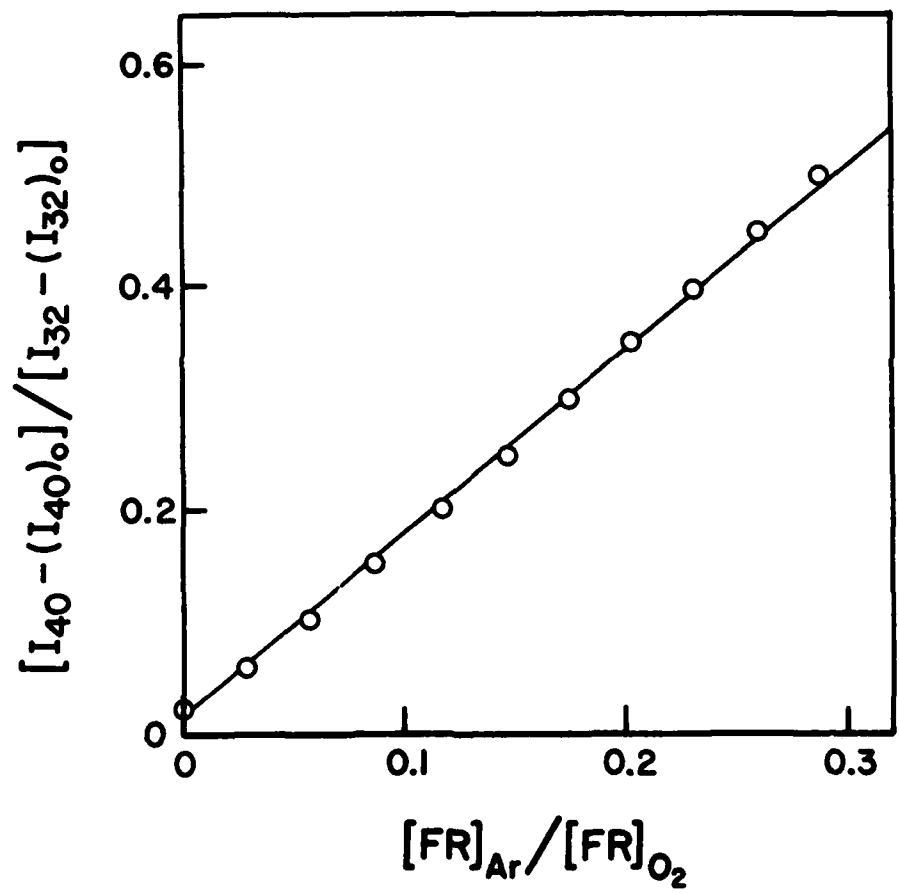


Figure 11. Plot of the relative ion intensity ratio  $[I_{40} - (I_{40})_0] / [I_{32} - (I_{32})_0]$  vs. the gas flow rate ratio  $[FR]_{Ar} / [FR]_{O_2}$ .

for mixtures containing less than 1-2% of CO in air. This is due to the presence of nitrogen which yields an ion,  $N_2^+$ , having the same nominal mass as that of the  $CO^+$  ion. The intensity of  $N_2^+$  ion is several orders of magnitude larger than that of the  $CO^+$  ion and cannot be separated in the quadrupole mass spectrometer system presently employed.

It is unlikely that the  $O^+$  ion, the second most abundant ion in CO, can be used for the monitoring of CO either. The interference caused by  $O^+$  ions from other species, such as  $O_2$  and  $CO_2$ , or  $CH_4^+$  ion from  $CH_4$ , can easily overwhelm the true  $O^+$  ion signal from CO, owing to the large difference in the ion intensities.

The only remaining ion that can be formed from CO is  $C^+$  ion. The adoption of this ion for the detection of CO is also difficult for the following two reasons. The first one is the low abundance of  $C^+$  ion intensity from CO, while the second one is the interference of  $C^+$  ions originating from other species, such as  $CO_2$ , and  $CH_4$ , as well as any C-containing species that also exist in the flame environment. Fortunately, those two difficulties are not insurmountable, especially when the concentration of CO is at least 1%, at which level the  $C^+$  ion intensity from CO is probably comparable with that from other sources just mentioned.

Assuming that, in a methane flame combustion system, the  $C^+$  ion is mainly derived from the gases CO,  $CO_2$  and  $CH_4$  only, one can write a calibration formula as follows:

$$\frac{I_{12} - (I_{12})_0}{I_{40} - (I_{40})_0} = \frac{k(C^+/CO)}{k(Ar^+/Ar)} \frac{(FR)CO}{(FR)Ar} + \frac{k(C^+/CO_2)}{k(Ar^+/Ar)} \frac{(FR)CO_2}{(FR)Ar} + \frac{k(C^+/CH_4)}{k(Ar^+/Ar)} \frac{(FR)CH_4}{(FR)Ar} \quad (6)$$

The above three relative sensitivity factors,  $\frac{k(C^+/CO)}{k(Ar^+/Ar)}$ ,  $\frac{k(C^+/CO_2)}{k(Ar^+/Ar)}$ , and  $\frac{k(C^+/CH_4)}{k(Ar^+/Ar)}$ , can therefore be individually derived through proper calibration

procedures. The above equation can also be rewritten in the form of relative mole fractions, that is,

$$\frac{I_{12} - (I_{12})_0}{I_{40} - (I_{40})_0} = \frac{k(C^+/CO)}{k(Ar^+/Ar)} \frac{(MF)CO}{(MF)Ar} + \frac{k(C^+/CO_2)}{k(Ar^+/Ar)} \frac{(MF)CO_2}{(MF)Ar} + \frac{k(C^+/CH_4)}{k(Ar^+/Ar)} \frac{(MF)CH_4}{(MF)Ar} \quad (7)$$

Therefore, during a flame sampling experiment, one can readily arrive at the needed relative mole fraction information,  $\frac{(MF)CO}{(MF)Ar}$ , through the measurement of the relative ion intensity,  $\frac{I_{12} - (I_{12})_0}{I_{40} - (I_{40})_0}$ , assuming that the other two relative mole fraction data,  $\frac{(MF)CO_2}{(MF)Ar}$  and  $\frac{(MF)CH_4}{(MF)Ar}$ , can be obtained simultaneously through the monitoring of the ions  $CO_2^+$  and  $CH_3^+$ , respectively. During the first set of calibration tests, a sample mixture of Ar and CO was chosen for calibration, and Eq. (6) can therefore be simplified, that is,

$$\frac{I_{12} - (I_{12})_0}{I_{40} - (I_{40})_0} = \frac{k(C^+/CO)}{k(Ar^+/Ar)} \frac{(FR)CO}{(FR)Ar} \quad (8)$$

In view of the low intensity of the  $C^+$  ion signal, a somewhat higher electron multiplier voltage setting (3000 volts) was chosen during this initial test. However, at this high voltage, the  $Ar^+$  ion signal was saturated. Therefore, the doubly charged  $Ar^{++}$  ion was chosen as the reference ion, so that,

$$\frac{I_{12} - (I_{12})_0}{I_{40} - (I_{40})_0} = \frac{k(C^+/CO)}{k(Ar^{++}/Ar)} \frac{(FR)CO}{(FR)Ar} \quad (9)$$

Of course, once the relative sensitivity factor,  $\frac{k(C^+/CO)}{k(Ar^{++}/Ar)}$ , is derived, one can readily obtain the other factor,  $\frac{k(C^+/CO)}{k(Ar^+/Ar)}$ , by multiplying the former factor

by the term,  $\frac{k(\text{Ar}^{++}/\text{Ar})}{k(\text{Ar}^+/\text{Ar})}$ , which is the same as  $\frac{I_{20} - (I_{20})^o}{I_{40} - (I_{40})^o}$ , measured for a pure argon system (at lower input resistor resistance setting to avoid  $\text{Ar}^+$  signal saturation).

One other complication encountered during the CO calibration is that the only CO gas currently available is from a cylinder reportedly containing 10% CO and 90% Ar. For better accuracy, this reported composition needs to be rechecked independently. For this reason, the terms  $(\text{FR})\text{CO}$  and  $(\text{FR})\text{Ar}$  in Eq. (9) should be rewritten as follows.

$$(\text{FR})\text{CO} = x \cdot [\text{FR}]\text{CO/Ar mixture cylinder} \quad (10)$$

$$(\text{FR})\text{Ar} = [\text{FR}]\text{Ar from Ar} + (1 - x) [\text{FR}]\text{CO/Ar mixture} \quad (11)$$

in which  $x$  is the mole fraction of CO in the CO/Ar mixture cylinder. Furthermore, due to this uncertainty in the CO/Ar mixture cylinder composition, the actual flow rate  $[\text{FR}]\text{CO/Ar}$  from the mixture cylinder cannot be directly measured from the reading of the linear mass flow meter ( $R$ ), but can be related to this reading through the following formula.

$$[\text{FR}]\text{CO/Ar mixture cylinder} = [1.43 (1-x) + 1.0 (x)]R \quad (12)$$

In the above equation, the numbers 1.43 and 1.0 are the gas conversion factors, if the linear mass flow meter is employed for monitoring the flow rates of pure argon and carbon dioxide, respectively. A rearrangement of the Eqs. (9), (10), (11) and (12) will yield

$$\frac{I_{20} - (I_{20})^o}{I_{12} - (I_{12})^o} = \frac{k(\text{Ar}^+/\text{Ar})}{k(\text{C}^+/\text{CO})} \frac{1-x}{x} + \frac{1}{x} \frac{1}{(1.43-0.43x)} \frac{[\text{FR}]\text{Ar from Ar}}{R} \quad (13)$$

A plot of the intensity ratio,  $\frac{I_{20} - (I_{20})^o}{I_{12} - (I_{12})^o}$ , vs  $[\text{FR}]\text{Ar from Ar}/R$  should yield a straight line having a slope of,

$$\text{Slope} = \frac{k(\text{Ar}^{++}/\text{Ar})}{k(\text{C}^+/\text{CO})} \cdot \frac{1}{x} \frac{1}{(1.43 - 0.43x)} \quad (14)$$

And an intercept,

$$\text{Intercept} = \frac{k(\text{Ar}^{++}/\text{Ar})}{k(\text{C}^+/\text{CO})} \cdot \frac{1-x}{x} \quad (15)$$

The solution of these two equations finally yields the value of  $x$ , and the relative sensitivity factor,  $\frac{k(\text{Ar}^{++}/\text{Ar})}{k(\text{C}^+/\text{CO})}$ .

Shown in Fig. 12 is a plot of the ion intensity ratio  $[I_{20} - (I_{20})_0] / [I_{12} - (I_{12})_0]$  vs the term  $[\text{FR}]_{\text{AR}}$  from  $\text{Ar}/R$ , as dictated by the Eq. (13). The derived value of  $x$  is 0.1075, which is in reasonable agreement with the reported value, (0.1). The relative sensitivity factor,  $\frac{k(\text{C}^+/\text{CO})}{k(\text{Ar}^{++}/\text{Ar})}$ , was found to be 0.395. The measurement of the other two relative sensitivity factors shown in Eq. (6) is still to be accomplished.

e. Water. The development of the calibration procedure for water, based on its flow rate relative to that of the reference gas, nitrogen, was accomplished during the previous reporting period and documented in the report for that period. Since there is no known interference that can significantly affect the accuracy for determining the water concentration, based on the characteristic ion  $\text{H}_2\text{O}^+$  ( $m/e = 18$ ), the derived calibration coefficient should be applicable for a real flame combustion environment.

As described previously, the water calibration was achieved with the use of a specially designed water oven inlet system. This system was designed for overcoming a series of technical problems, including the precise water flow rate control, fluctuation of water vapor flow due to condensation, accurate measurement of the water flow rate, etc. Strictly speaking, the calibration results obtained with this system will not necessarily agree with those obtained under true flame sampling conditions. Uncertainty may arise due to a new set of complications, such as the differences in the water sampling conditions, mass spectrometer inter-

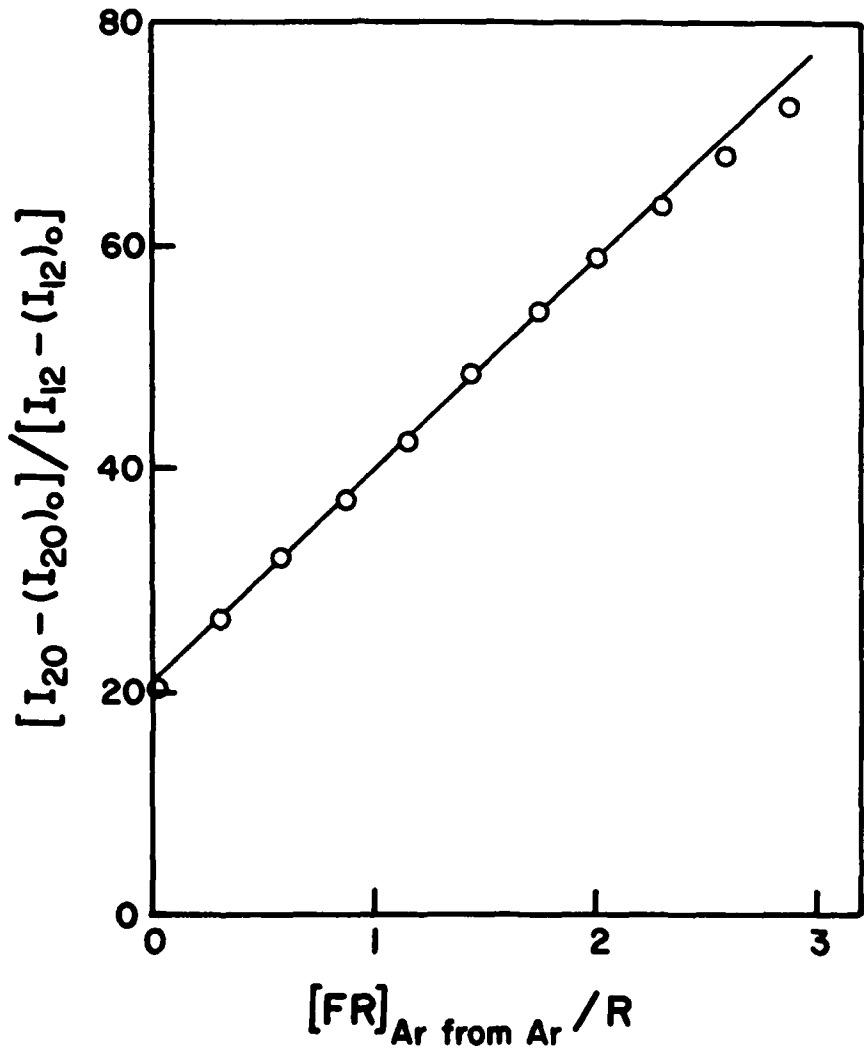


Figure 12. Plot of the relative ion intensity ratio  $[I_{20} - (I_{20})_0] / [I_{12} - (I_{12})_0]$  vs. the ratio  $[FR]_{\text{Ar from Ar}} / R$ .

facing structures, and so on. This uncertainty can only be resolved by future flame sampling tests, in which the theoretical water concentration can be estimated on the basis of the measured consumption of the fuel.

### 3. Summary.

Table IV summarizes the mathematical relations which can be used for calculating the relative mole fractions of various gaseous species in the combustor, on the basis of the mass spectrometrically measured ion intensities and the calibration coefficients. Detailed discussion of these relations, as well as consideration of the interferences encountered in measuring the intensities of the various ions have been presented in the foregoing.

Also presented in Table V. is a listing of the calibration coefficients measured from the calibration tests described in the preceding discussion. Also shown here are the results of a complete new series of gas calibration tests in which the voltage of the mass spectrometer electron multiplier detector was set at 2500 V (higher than previously). It is seen that operation of the electron multiplier at this increased voltage yields adequate sensitivity for the detection of even quite small intensity ion signals, such as the  $C^+$  ion derived from CO, while at the same time, the signals of other larger ions, such as  $CH_3^+$  from  $CH_4$  and  $O_2^+$  from  $O_2$ , are not saturated.

## IV. MEASUREMENT OF GAS SPECIES CONCENTRATION PROFILES IN A ONE-DIMENSIONAL FLAT FLAME

Prior to conducting actual monitoring of gaseous species in a reactive ramjet combustor system, it is desirable to test the gas monitoring apparatus by using a smaller-scale reactive combustion environment. A flat-flame burner, for which the flame characteristics and the combustion product distributions have already been well established in several instances, is well suited for this purpose. Experiments with this burner are also useful in assessing various

TABLE IV

FORMULAE FOR THE CALCULATION OF THE RELATIVE  
MOLE FRACTIONS OF GASEOUS SPECIES

<u>Species</u>	<u>Formula</u>	
CH <sub>4</sub>	$\frac{[MF]_{CH_4}}{[MF]_{Ar}} = \frac{k(Ar^+/Ar)}{k(CH_3^+/CH_4)}$	$\frac{I_{15} - (I_{15})_0}{I_{40} - (I_{40})_0}$
CO <sub>2</sub>	$\frac{[MF]_{CO_2}}{[MF]_{Ar}} = \frac{k(Ar^+/Ar)}{k(CO_2^+/CO_2)}$	$\frac{I_{44} - (I_{44})_0}{I_{40} - (I_{40})_0}$
O <sub>2</sub>	$\frac{[MF]_{O_2}}{[MF]_{Ar}} = \frac{k(Ar^+/Ar)}{k(O_2^+/O_2)}$	$\frac{I_{32} - (I_{32})_0}{I_{40} - (I_{40})_0}$
H <sub>2</sub> O	$\frac{[MF]_{H_2O}}{[MF]_{Ar}} = \frac{k(Ar^+/Ar)}{k(H_2O^+/H_2O)}$	$\frac{I_{18} - (I_{18})_0}{I_{40} - (I_{40})_0}$
CO	$\frac{[MF]_{CO}}{[MF]_{Ar}} = \frac{k(Ar^+/Ar)}{k(C^+/CO)}$	$\frac{I_{12} - (I_{12})_0}{I_{40} - (I_{40})_0}$
	$- \frac{k(C^+/CO_2)}{k(Ar^+/Ar)}$	$\frac{[MF]_{CO_2}}{[MF]_{Ar}}$
	$- \frac{k(C^+/CH_4)}{k(Ar^+/Ar)}$	$\frac{[MF]_{CH_4}}{[MF]_{Ar}}$

TABLE VCALIBRATION COEFFICIENTS DERIVED FROM THE GAS CALIBRATION TESTS

<u>Coefficient</u>	<u>Electron Multiplier Voltage (V)</u>		
	<u>1800</u>	<u>3000</u>	<u>2500</u>
$\frac{k(\text{CH}_3^+/\text{CH}_4)}$	0.4577	-	0.4810
$\frac{k(\text{Ar}^+/\text{Ar})}$			
$\frac{k(\text{CO}_2^+/\text{CO}_2)}$	0.990	-	1.053
$\frac{k(\text{Ar}^+/\text{Ar})}$			
$\frac{k(\text{O}_2^+/\text{O}_2)}$	0.625	-	0.5976
$\frac{k(\text{Ar}^+/\text{Ar})}$			
$\frac{k(\text{C}^+/\text{CO})}$	-	0.395	0.3633
$\frac{k(\text{Ar}^{++}/\text{Ar})}$	-	-	0.0662
$\frac{k(\text{Ar}^+/\text{Ar})}$			
$\frac{k(\text{C}^+/\text{CO})}$	-	-	0.2405
$\frac{k(\text{Ar}^+/\text{Ar})}$			
$\frac{k(\text{C}^+/\text{CH}_4)}$	-	-	0.01074
$\frac{k(\text{Ar}^+/\text{Ar})}$			
$\frac{k(\text{C}^+/\text{CO}_2)}$	-	-	0.03425
$\frac{k(\text{Ar}^+/\text{Ar})}$			

probe designs, and yield an indication of the overall capabilities of the analytical system, in its present configuration, for monitoring reactive environments.

Among the various types of flames which could be sampled, a premixed laminar flat flame is the best suited for the present evaluation. This is essentially a one-dimensional flame, in which the flame species concentration profiles can be readily monitored by moving the sampling probe (or the flame burner itself) along the direction perpendicular to the flame front. The gas mixture selected for the initial flame sampling experiments was methane-air and methane-oxygen, since such flames have previously been extensively studied (13,14,15).

#### A. System Description

Figure 13 shows a schematic diagram of the flat flame burner assembly designed and constructed for the present project. The burner assembly is housed within a 6" stainless steel cross which is mounted on a stand (not shown). The front side of the cross is sealed with a glass viewing port while the other three ends are sealed by stainless steel blank flanges. Pumping is accomplished through the top flange, which is connected to a mechanical pump via a throttle valve. This permits precise control of the pressure within the housing, as measured by a pressure gauge. The latter is also mounted on the top flange.

The design of the flat flame burner assembly shown here is similar to that currently employed at APL for monitoring the concentrations of gaseous species using the Coherent Anti-Stokes Raman Scattering (CARS) technique (15). Use of the same burner in our tests will thus make it possible to directly compare experimental data obtained on essentially identical flames using the two different monitoring techniques. As seen in Figure 13, the burner body is supported by an 0.5" O.D. stainless steel tube (Fuel/air inlet) which is mounted on the bottom flange but can be moved to alter the burner position. The position of the burner

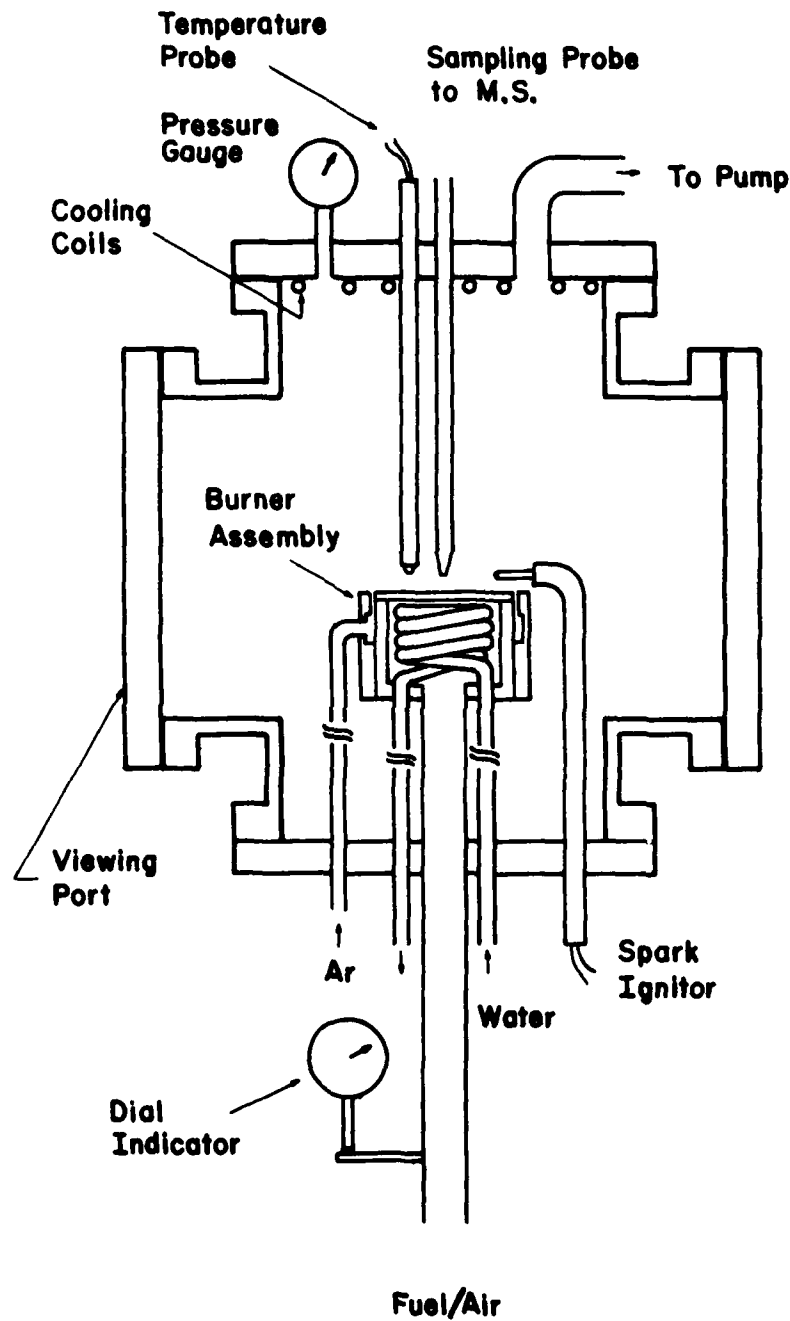


Figure 13. Schematic Diagram of the Flat Flame Burner Assembly.

with respect to the bottom flange is indicated by a dial indicator which has a range of 6 inches and an accuracy of  $\pm 0.001$  inches. A copper tubing cooling coil is placed within the burner body cavity, and the remainder of the cavity volume is filled with heat conductive beads, to provide efficient heat transfer between the cooling coil and the burner body. The top of the burner body is covered by a porous stainless steel disk (2.5" diameter x 1/8" thickness). Disks having various pore sizes ranging from 0.5 to 100 microns will be experimentally tested to achieve the best burner performance. Surrounding the burner body is a ring through which argon can be injected in order to form an outer argon sheath (0.03" thick) which shields the flame and ensures better flame stability. Both the argon and water feed lines are stationary and pass through the bottom flange, where connections to the proper sources are made.

The burner is ignited under vacuum by an ignitor, which consists of a copper rod and a ceramic insulator tube (1/4" OD). During ignition, a high voltage is applied to the copper rod which causes an electric arc to be formed between the rod and the burner top surface. After the burner is ignited, the ignitor can be rotated and pulled back to a recessed position. The required high voltage is provided to the ignitor by a suitable supply, such as a Tesla coil.

The top flange of the burner assembly is cooled by a water cooling coil which is welded to the underside of the flange surface. Further cooling of the cross can also be achieved with some simple modifications, should this be necessary. The flame temperature is monitored by a thermocouple probe. A platinum - platinum, 10% Rhodium bare wire thermocouple probe and accessory components are used for this purpose. Since the smallest diameter wire commercially available for use in the thermocouple probe is 0.0125 inches (30 gauge), which is still too large to achieve the desired resolution in the flame temperature measurement, further modification of the probe tip may be necessary. In addition, conditioning of the thermocouple probe tip will also be required in order to prolong the

usable lifetime of the probe in the combustion environment.

Several additional components associated with the burner which were installed to facilitate operation include, a) a mechanical-drive system, which was designed and fabricated for the purposes of accurately moving and adjusting the burner; b) an exhaust pipe, which is connected to the burner pump in order to direct the burner exhaust gas through the building exhaust fan; c) a modification of the burner pumping line, which was accomplished to provide better protection of the throttle valve from the heat produced by the burner; d) a modification of the fuel/air mixing system, which was accomplished to provide additional safety in the event of an unlikely, but still possible, flame flash-back; and e) a direct interface line and the associated heating and valving system, which was established between the sampling probe and the mass spectrometer inlet.

Several quartz microprobes were fabricated during this program for use in flame sampling. These probes are typically 6mm. in diameter and 35 cm. in length, with tip diameters ranging from 0.001 to several thousandths of an inch. An important parameter that must be assessed for each of these probes is its sampling rate (from a given sampling environment), which is dependent on the probe tip geometry as well as its diameter. This parameter was experimentally determined for several probes in the course of the present project. In these experiments, the tip of a probe was attached to a manifold, in which the pressure ( $P$ ) was monitored by a pressure gauge (0 - 1 atm). A regulated air flow, for which the flow rate ( $Q$ ) was accurately measured by a linear mass flow meter, was introduced into the manifold. This flow enters the probe tip and is subsequently removed by a pumping system, which is connected to the other side of the probe. With this arrangement, the main restriction in the flowing stream is at the probe tip, and, therefore, a measurement of the values,  $Q$  and  $P$ , should yield a value,  $C$ , which is the conductance of the probe tip. Figure 14 shows a typical plot of the measured air flow rate  $Q$  (sccm) as a function of the manifold pressure,  $P$ .

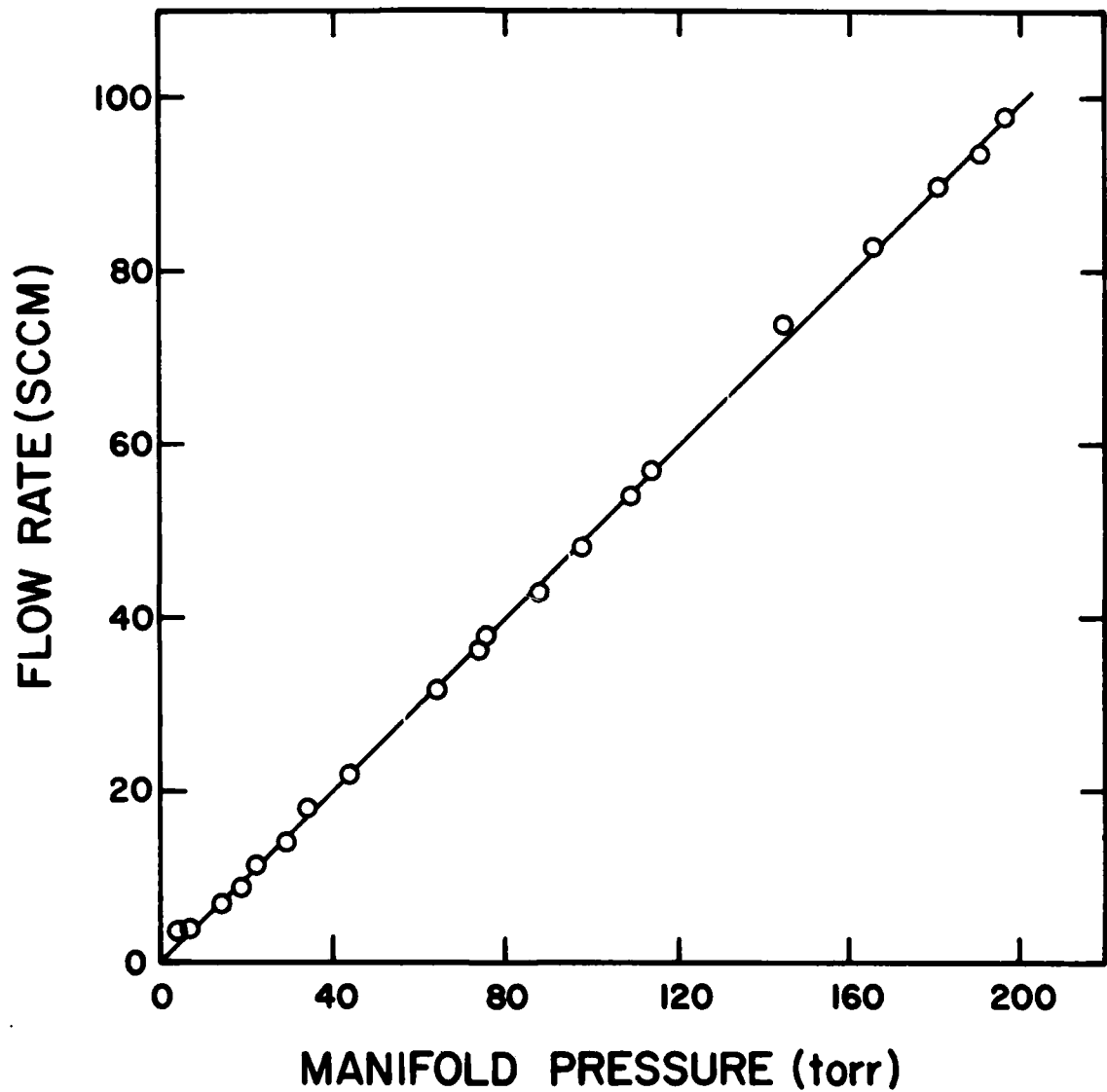


Figure 14. Plot of air flow rate through the quartz microprobe vs. the manifold pressure.

(torr.) for one quartz microprobe (QP-I). The plot is quite linear and yields a constant value of  $C = 6.28$  cc/sec, that is,

$$Q \text{ (cc-torr/sec)} = 6.28 \text{ (cc/sec)} \times P \text{ (torr)} \quad (16)$$

A direct inspection of this same probe, using microscopic magnification, indicated that this particular probe has an inside diameter of 0.0084 inches. It is of interest to calculate the theoretical conductance of this probe based on the measured diameter, for comparison with the experimentally measured conductance. This may be of use in achieving a better understanding of the probe-tip geometry characteristics. The standard expression for the calculation of the adiabatic isentropic flow rate ( $Q$ ) through a nozzle of area  $A$  is,

$$Q = \gamma^{\frac{1}{2}} \left(\frac{1}{R}\right)^{\frac{1}{2}} \left(\frac{2}{\gamma+1}\right)^{\frac{\gamma+1}{2(\gamma-1)}} \cdot (A) \cdot (P) \left(\frac{1}{T}\right)^{\frac{1}{2}} \quad (17)$$

in which  $\gamma$  is the ratio of the specific heat (1.4 for air),  $R$  is the gas constant and  $P$  and  $T$  are the upstream pressure and temperature of the gas respectively. This equation assumes that sonic flow prevails at the nozzle throat, which is true if the downstream pressure  $P'$  meets the following requirement,

$$P' \leq \left(\frac{2}{\gamma+1}\right)^{\gamma/\gamma-1} P \quad (18)$$

In the present experimental arrangement, the above criteria is fulfilled, since the probe on the downstream side is constantly pumped to vacuum. By inserting the measured probe diameter of 0.0084" (which in turn yields the value  $A$ ) into the nozzle equation, one obtains,

$$Q \text{ (cc-torr/sec)} = 6.45 \text{ cc/sec} \times P \text{ (torr)} \quad (19)$$

This calculated value of  $c = 6.45$  cc/sec is in excellent agreement with the experimentally measured value of 6.28 cc/sec. This indicates that the geometry

of the probe tip, as fabricated using standard glass blowing techniques, closely resembles that of an ideal nozzle, and no correction factor is required to determine either the flow rate or the probe diameter, by using the nozzle equation, if either one of these two parameters can be experimentally measured. It is also interesting to note that a calculation of the probe conductance based on the molecular-flow pin-hole equation yields a value which is approximately 50% lower than the measured value.

As stated previously, one important function of the present flat flame burner system is to evaluate the performance of various probe designs, and to identify an acceptable probe design for future ramjet combustor sampling application. In view of the hostile environment which generally prevails in a ramjet combustor flow field, the only type of sampling probe which is applicable is a water-cooled metal probe. However, prior to the actual construction such a probe for ramjet sampling applications, it is vitally important that the performance of probes of this type be carefully evaluated, since several potential problems are known to be associated with water-cooled metal probes in general (this is discussed further in the following section). The procedure for evaluation entails comparison of the flat flame species concentrations obtained by sampling the flame using the water-cooled metal probe with the corresponding results obtained by using a quartz microprobe under identical operating conditions. For the purpose of the evaluation just described, a miniature water-cooled metal probe that can be fitted into the present flat flame burner system was designed and fabricated. A schematic diagram of this probe is shown in Fig. 15. It consists of three stainless steel concentric tubes properly welded together. The outside diameters and wall thicknesses of these tubes are respectively: 0.125", 0.012" (outside tube); 0.083", 0.010" (middle tube); and 0.042", 0.00775" (inner tube). The inner tube is welded to the probe tip, the composition and shape of which are still to be decided, subject to future experimental testing. Important

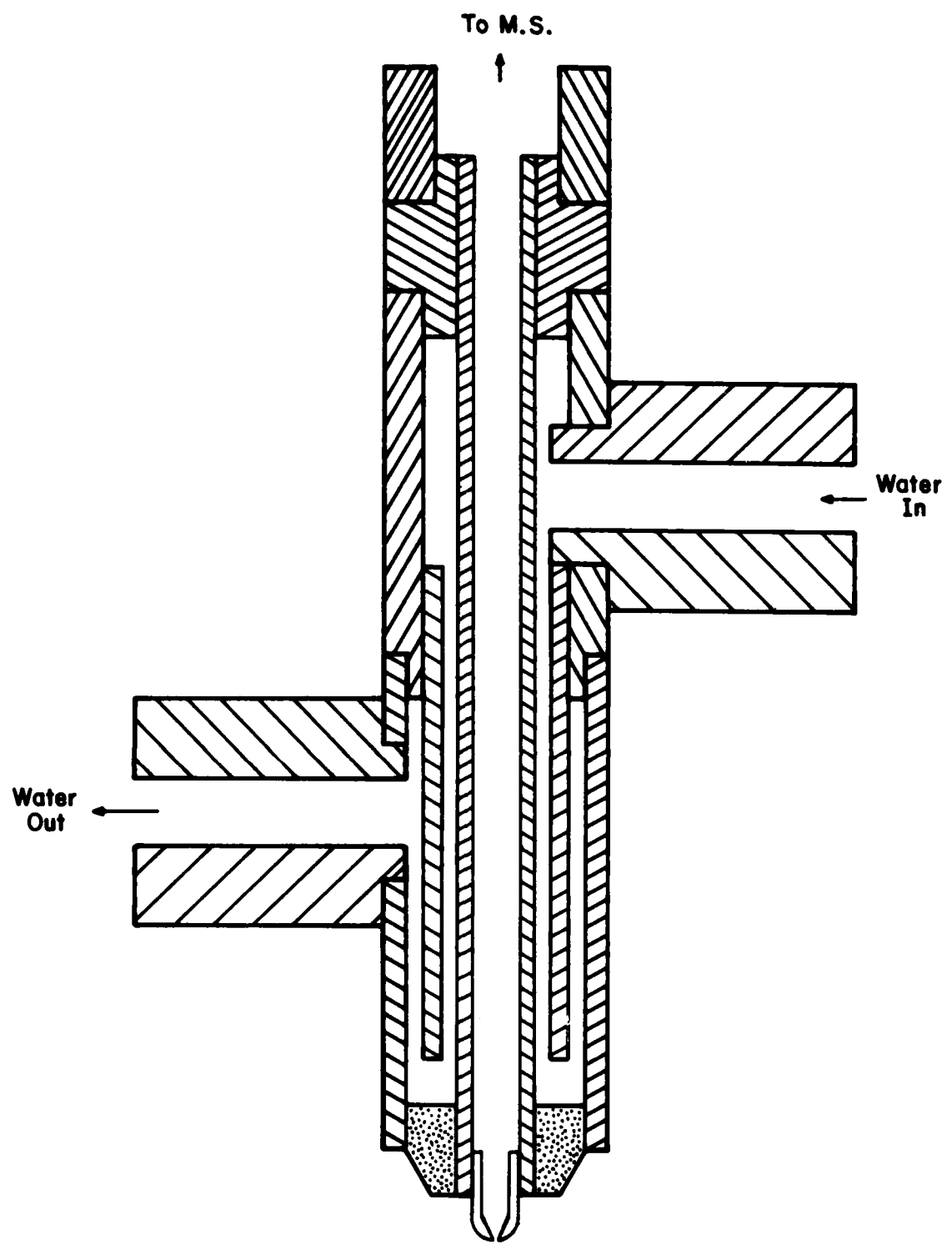


Figure 15. Schematic Diagram of the Miniature Water-Cooled Metal Probe.

design requirements for the probe tip include the following: 1) the orifice of the probe must be as small as possible, but not so small as to permit excessive plugging by soot produced from the flame during a typical sampling period; 2) the design of the interior of the probe tip must be such that efficient aerodynamic cooling of the sampled gas is achieved; and 3) the material used in construction of the probe tip must be chemically inert to the flame environment, and physically capable of withstanding the flame sampling temperature.

The evaluation of this initially developed miniature metal probe was subsequently interrupted because a drastically new concept in the design of a sampling probe for ramjet combustor sampling was conceived. With this new design, the critical probe tip portion is constructed of quartz, while the probe body section is fabricated from a suitable metal material and is equipped for water cooling. In this manner, the advantages associated with the use of a quartz microprobe for sampling are retained, and at the same time adequate support for the probe is realized. A detailed discussion of this probe will be provided in later sections of this report. With this new design, all of the sampling problems normally associated with the use of a conventional metal probe are virtually eliminated and evaluation of such a probe as that shown schematically in Fig. 15 is no longer necessary for the present project.

#### B. Experimental Results

Prior to the flame sampling experiments several preliminary tests were conducted to observe the general performance of the burner itself. One such test was conducted under conditions similar to those employed previously with a Battelle-fabricated burner which is also installed at the APL laboratory (15). The flow rates of nitrogen, oxygen, and fuel ( $\text{CH}_4$ ) were set at 3900, 1248, and 528 sccm, respectively. It was observed that a stable flame was produced over a wide range of burner pressures, ranging from 1 atm. down to 10 torr. The pressure was readily controlled by adjusting the setting of the pump throttle

valves. At higher pressures (above 400 torr.), the flame appears to be greenish-blue in color, and turns completely green as the flame becomes richer in fuel. The flame was observed to attach to the burner base with a very flat bottom. At medium pressures (100-400 torr.), the flame was observed to be blue in color. The bottom of the flame was still attached to the burner base, but its edge was curved slightly upward. At lower pressures (below 100 torr.) the flame was purple in color, with its bottom completely detached from the burner base. The extent of detachment and the thickness of the luminous zone become greater with further decrease of the burner pressure, and finally the flame can no longer be sustained when the pressure is decreased much below 10 torr.

Another preliminary burner test was carried out with a sampling probe inserted into the flame. A quartz microprobe (QP-III) was chosen for this test. During this test, a mixture of nitrogen (at 3900 SCCM), oxygen (at 1248 SCCM) and methane (528 SCCM) was introduced into the burner, while the burner housing pressure was varied between 50 and 600 torr. Three different probe positions (0.1, 0.5, and 1.0 cm, respectively, above the burner base) were chosen. The flame was ignited in the manner previously described. The gas sampled through the probe was directly introduced into the mass spectrometer ion source without differential pumping. There was no visual disturbance of the flame due to the presence of the probe. The probe was very clean after sampling the burner for a period of about two hours. The ion signals observed for the sampled gas were very stable, although no quantitative measurement was made.

After these preliminary burner tests several series of flame sampling tests were accomplished. In each of these tests, a gaseous mixture, formed from separately monitored streams of air (or oxygen) and fuel (methane), was introduced into the flat flame burner inlet. The pressure within the burner housing was maintained at a given pressure by adjusting the opening of a valve connecting the housing with a mechanical pump. The burner was ignited, and the gaseous species

present in the burner flame were then sampled through a quartz microprobe, which was inserted into the burner housing along the centerline of the flat flame burner. Quartz microprobes of several different internal diameters, ranging from 0.003 to 0.008 inches, were employed in these tests. The gas sampled was then introduced into the mass spectrometer for analysis.

Prior to each series of flame sampling tests, two individual test runs were conducted. The first run entailed sampling of the background ion signal in each ion mass channel, with the valve leading to the ion source inlet closed. These ion signals ( $I_i$ )<sub>0</sub>, correspond to the instrument background and must be subtracted from the total ion signals ( $I_i$ ), respectively, prior to any subsequent calculation. The second run was conducted prior to flame ignition, and entailed sampling of the unburned gas mixture through the quartz probe, and analysis of this mixture by the mass spectrometer. Since the composition of this gas mixture is known as a result of the flow rate measurements for the feed gas, the ion signals observed can be used for the derivation of the calibration coefficients of the unburned gaseous species ( $\text{CH}_4$ , Ar and  $\text{O}_2$ ) in this mixture.

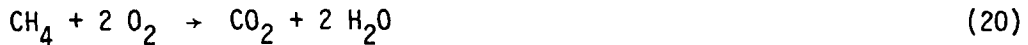
After completion of the two above-mentioned test runs, the burner was ignited, using the ignition system described earlier. Flame sampling tests were then initiated, after the flame had been properly stabilized. Typically 20-30 sampling runs were conducted in a given test, with the sampling probe positioned at various levels above the burner base. Vertical movement of the burner was achieved by using the mechanical traversing system, and the position of the burner was measured by a dial indicator ( $\pm 0.001"$  accuracy). Both of these devices were described in the previous section of this report. Due to the pressure variation across the flame center line, the amount of gas sampled through the probe may vary with the relative probe position. Proper adjustment must be made prior to each run to ensure that the ion source pressure is maintained at  $1 \times 10^{-5}$  torr.

The details of the operation of the mass spectrometer-computer in scanning

selected ion masses, ion signal integration, and data reduction, in order to determine the values of the relative ion intensities,  $\frac{I_i - (I_{i0})}{I_{40} - (I_{400})}$ , in each flame sampling run, have been described previously and will not be repeated here. The relative ion intensities, used in conjunction with the calibration coefficients (from Table V), then yield the relative mole fractions of all the gaseous species present at each flame sampling position, when the formulae listed in Table IV are utilized. However, there is a difficulty in actually using these previously derived calibration coefficients in the present calculations. As a consequence of day-to-day variations in the system, it was found necessary to make minor daily mass spectrometer adjustments (ion focusing setting, resolution dial,  $\Delta m$  control) in order to obtain ion signals having the desired peak shape and resolution. These adjustments will inevitably change the calibration coefficient values slightly. As a result, new calibration coefficients,  $\frac{k(\text{CH}_3^+/\text{CH}_4)}{k(\text{Ar}^+/\text{Ar})}$  and  $\frac{k(\text{O}_2^+/\text{O}_2)}{k(\text{Ar}^+/\text{Ar})}$ , were actually determined for each test based on the known gas composition (determined from flow rate measurements) of the unburned gas mixture. It was found that these numbers generally fluctuate within  $\pm 5\%$  which is undoubtedly due mainly to the system adjustments just mentioned. In order to achieve the most accurate results, these newly derived coefficients must obviously be employed, (instead of the previously obtained values shown in Table V) for calculation of the relative mole fractions of  $\text{CH}_4$  and  $\text{O}_2$  in the flame.

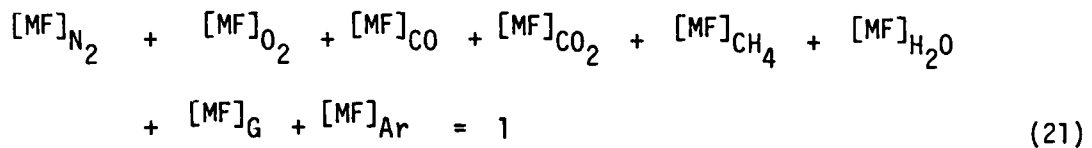
It is likely that the daily instrument adjustments mentioned above will also affect the calibration coefficients for other species including  $\text{CO}_2$ ,  $\text{H}_2\text{O}$ , and  $\text{CO}$ . For purposes of internal consistency, therefore, a new calibration coefficient for each of these gases is calculated during each test, based on the assumption that complete combustion is achieved at a location 0.5 inch or more above the burner base under the present experimental conditions. This assumption is

verified by the observation that the relative ion intensity,  $\frac{I_{15} - (I_{15})_0}{I_{40} - (I_{40})_0}$ , has reached zero even before the probe reaches the 0.5 inch position, while other relative ion intensities, such as  $\frac{I_{32} - (I_{32})_0}{I_{40} - (I_{40})_0}$  (for  $O_2$ ),  $\frac{I_{18} - (I_{18})_0}{I_{40} - (I_{40})_0}$  (for  $H_2O$ ), and  $\frac{I_{44} - (I_{44})_0}{I_{40} - (I_{40})_0}$  (for  $CO_2$ ), remain constant when the sampling probe is positioned 0.5 inch or more above the burner base. The chemical equation which describes complete combustion is,



From this equation, the final gas composition under conditions of complete combustion can be derived from the known initial gas composition of the unburned gas mixture. The calibration coefficients,  $\frac{k(CO_2^+/CO_2)}{k(Ar^+/Ar)}$ ,  $\frac{k(H_2^+/H_2)}{k(Ar^+/Ar)}$ ,  $\frac{k(C^+/CO_2)}{k(Ar^+/Ar)}$ , and  $\frac{k(C^+/CH_4)}{k(Ar^+/Ar)}$  for each of these tests can thus be calculated. However, the coefficient,  $\frac{k(C^+/CO)}{k(Ar^+/Ar)}$ , must be taken from Table V, since it cannot be derived under the present scheme.

In order to determine the absolute mole fractions of the species of interest, it is desirable that the relative mole fractions of all other non-monitored species also be estimated. This can be achieved by assuming that the flame composition at any location consists solely of  $N_2$ ,  $O_2$ ,  $CO$ ,  $CO_2$ ,  $CH_4$ ,  $H_2O$ , Ar and G. The symbol "G" stands for the total quantity of other minor gaseous species present at trace levels (0.06%, not including  $CO_2$ ) in the dry air, but which do not participate in the combustion process. The above assumption can be mathematically expressed by the relation,



This assumption is, of course, a crude one since it is known from reports in the literature that many other species, including stable molecules such as  $H_2$ , and  $H_2CO$ , radicals such as  $CHO$ ,  $OH$ ,  $O$ , and ions of various kinds, are all present within the flame at various stages. It is anticipated that more of the stable molecules which are present can be experimentally monitored by improving the present detection system. However, it is doubtful that the free radical and ionic constituents can be successfully sampled using the system in its present configuration. Modifications incorporating molecular beam sampling will be required to monitor such unstable species.

As noted in Table IV, the present mass spectrometric detection system is only capable of determining the relative mole fractions of the species indicated, that is, the mole fractions with reference to the mole fraction of Ar. In order to obtain the absolute mole fraction of each of these species, the mole fraction of Ar must be known independently. In dry air, the mole fraction of Ar is known to be 0.00934. But in a flame system, the value of  $[MF]_{Ar}$  is no longer a constant owing to the occurrence of the combustion processes. A new approach was therefore adopted here for solving this problem. It is noted that if Eq. (21) is divided by the term  $[MF]_{Ar}$ , a new expression is obtained,

$$\begin{aligned}
 \frac{[MF]_{N_2}}{[MF]_{Ar}} + \frac{[MF]_{O_2}}{[MF]_{Ar}} + \frac{[MF]_{CO}}{[MF]_{Ar}} + \frac{[MF]_{CO_2}}{[MF]_{Ar}} + \frac{[MF]_{CH_4}}{[MF]_{Ar}} \\
 + \frac{[MF]_{H_2O}}{[MF]_{Ar}} + \frac{[MF]_G}{[MF]_{Ar}} + \frac{[MF]_{Ar}}{[MF]_{Ar}} = \frac{1}{[MF]_{Ar}}
 \end{aligned} \tag{22}$$

If every term on the left side of this equation is known, either by direct

measurement or from other methods, the value of the absolute mole fraction of  $[MF]_{Ar}$  can thus be calculated. Consequently, the absolute mole fractions of all other species can also be derived, once the value of  $[MF]_{Ar}$  at each probe location is known.

In Eq.(22) there are three terms not affected by the flame combustion processes, and which remain constant, regardless of the probe position. The values of these terms are,

$$\frac{[MF]_{N_2}}{[MF]_{Ar}} = 84.58 \quad (23)$$

$$\frac{[MF]_G}{[MF]_{Ar}} = 0.06 \quad (24)$$

$$\frac{[MF]_{Ar}}{[MF]_{Ar}} = 1.00 \quad (25)$$

The relative mole fractions of  $O_2$ ,  $CO$ ,  $CO_2$ ,  $CH_4$  and  $H_2O$  are directly measurable, since their corresponding ion signals can be monitored, in each individual flame sampling test. As discussed in a later section, this is indeed true for data obtained using the newly acquired 16-channel digital mass programmer. This permits direct derivation of the absolute mole fraction of Ar using Eq. (22).

Shown in Table VI are the experimental conditions for four sets of flame sampling tests conducted during an earlier stage of the present project. The data presented in this table were obtained with the previously utilized 6-channel analog mass programmer which is capable of acquiring only 5 ion signals at a time, for reasons discussed previously. As a result, a direct experimental measurement of the relative mole fraction of  $O_2$  was achieved only for tests 2 and 3, since the indicator ion,  $O_2^+$ , was not monitored during the other two

TABLE VI

EXPERIMENTAL CONDITIONS FOR FLAME SAMPLING TESTS

<u>Parameter</u>	<u>Test No.</u>			
	<u>1</u>	<u>2</u>	<u>3</u>	<u>4</u>
Air flow rate (SCCM)	4980	4988	5010	4960
Methane flow rate (SCCM)	480	481	492	481
Burner pressure (torr)	115	115	115	115
Probe	QP-II	QP-II	QP-IV	QP-IV
Probe tip I.D. (in)	0.008	0.008	0.003	0.003
Probe position range (in)	0-0.55	0-0.74	0-1.00	0-1.10
Ion Source pressure (torr)	$10^{-5}$	$10^{-5}$	$10^{-5}$	$10^{-5}$
Electron multiplier voltage (Volt)	2500	2500	2500	2500
Ions monitored (m/e)	12	15	15	12
	15	18	18	15
	18	32	32	18
	40	40	40	40
	44	44	44	44
Flame temperature measurement	No	No	Yes	Yes

tests. Similarly, the experimentally measured value of  $[MF]_{CO}/[MF]_{Ar}$  was obtained only from tests 1 and 4, since the  $C^+$  ion signal was not monitored in tests 2 and 3. In order to derive the complete mole fraction profiles of all major flame species, an additional procedure, involving the material balance of the elements O and C, must be applied. This procedure, as well as the resultant mole fraction profiles obtained in four flame sampling tests were described in previous reports. No further discussion of these is given here, since several other more complete flame sampling tests were subsequently accomplished, for which the results are described below.

Several flame sampling tests were conducted in which data were acquired with a new 16-channel digital mass-programmer, which allows all major flame species to be directly monitored during each test. Table VII provides a brief listing of the experimental conditions employed for the latter flame tests. The initial composition of the fuel mixtures used in these tests, prior to flame ignition, is also shown in this table. A quartz microprobe with nominal I.D., 0.005 inch, was used in all of these tests. The ions monitored include m/e 2, 12, 14, 15, 16, 17, 18, 28, 30, 32, 40, and 44. One background channel was also monitored. The mass spectrometer ion source was maintained at a pressure of  $1 \times 10^{-5}$  torr, and the electron multiplier voltage was set at 3000 volts. Other mass spectrometric parameters, such as resolution and DM, were adjusted prior to each test, in order to obtain optimum performance. For this reason, the signal response for each measured component must be recalibrated during each test. The calibration procedure is essentially the same as that described previously.

Shown in Fig. 16 are the measured profiles of the mole fractions of all major flame species in a methane/air flame sampled using the system described. The species monitored include  $N_2$ ,  $O_2$ ,  $CH_4$ ,  $H_2O$ ,  $CO_2$ , CO and Ar. Each profile applies to a flame region spanning the range from 0 to 2 inches above the flame base. Also shown in this figure is the initial composition of the methane/air mixture.

Table VII

EXPERIMENTAL CONDITIONS FOR FLAME SAMPLING TESTS

<u>Parameters</u>	<u>Test No.</u>			
	<u>1</u>	<u>2</u>	<u>3</u>	<u>Ref. 1</u> <sup>a</sup>
Figure In Which Data Presented	16	17	19	19
Air flow rate (SCCM)	5000	0	0	---
O <sub>2</sub> flow rate (SCCM)	0	4850	8051	---
Methane flow rate (SCCM)	500	414	690	---
Argon flow rate (SCCM)	0	71.5	140	---
Burner pressure (torr)	115	110	50	76
Gas Velocity (cm/sec)	20.0	19.4	71	~65
Initial Composition (Mole Fraction)				
N <sub>2</sub>	0.7067	0	0	0.0008
O <sub>2</sub>	0.1896	0.8970	0.8934	0.9143
CH <sub>4</sub>	0.0905	0.0712	0.0766	0.0785
CO <sub>2</sub>	0.0022	0.0099	0.0058	0.0022
H <sub>2</sub> O	0.0009	0.0075	0.0087	0.0006
CO	0.0000	0.0000	0.0000	0
Ar	0.0085	0.0146	0.0156	0.0034
Initial Temperature °C	25	25	25	77

a. R. M. Fristrom, C. Grunfelder and S. Favin, "Methane Oxygen Flame Structure. I. characteristic Profiles in a Low-pressure Laminar Lean, Premixed Methane-Oxygen Flame", J. Phys. Che. 64, 1386 (1960)

b. Not reported

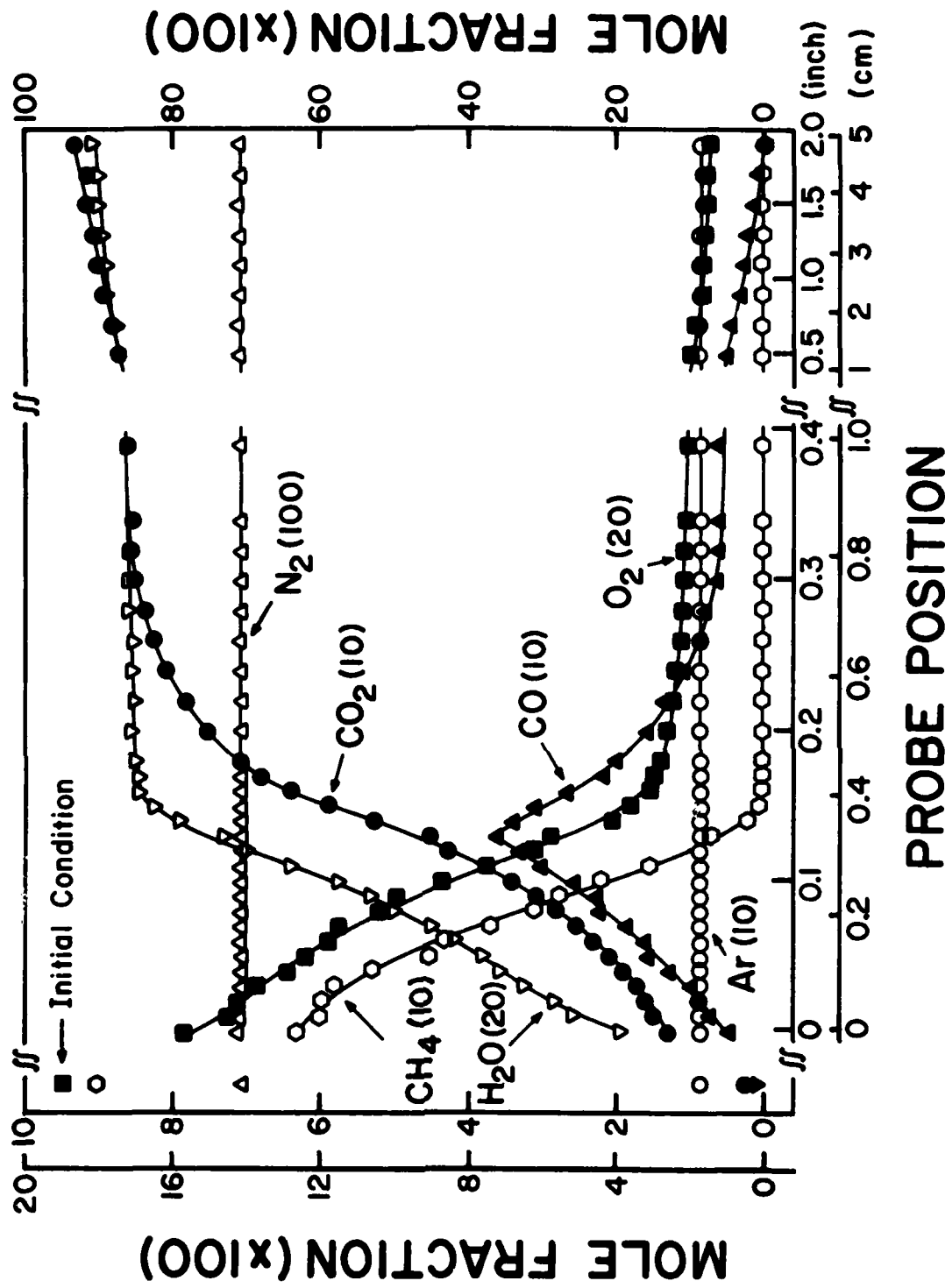


Figure 16. Mole fraction profiles in the methane/air flame. Test No. 1.

## PROBE POSITION

It is seen from Fig. 16 that the mole fraction of methane rapidly drops to zero at a distance within approximately 0.15 inch from the burner base. This is accompanied by a sharp rise in the mole fraction of water. Within this region, the rate of increase of the mole fraction of water is almost exactly twice as large as the rate of decrease of the methane mole fraction, as suggested by their stoichiometric relationship. The mole fraction of CO also rises within this region with increasing distance from the burner base, until a maximum is reached, the position of which coincides with that corresponding to complete depletion of the methane fuel. At still greater distances, the CO concentration gradually decreases until it is zero. In a manner similar to the water profile, the mole fraction of  $\text{CO}_2$  also increases sharply with increasing distance from the burner base, within this first region. However, even after the methane fuel is depleted, the mole fraction of  $\text{CO}_2$  continues to rise, although at a much slower rate. This is consistent with a two-stage combustion process, the first stage being the region where  $\text{CH}_4$  is converted to CO and  $\text{H}_2\text{O}$ , and the second stage, that where CO is converted to  $\text{CO}_2$ . This is also confirmed by the profile of the  $\text{O}_2$  mole fraction, which also consists of an initial region in which  $\text{O}_2$  decreases sharply and a second region in which a slower decrease occurs.

It should be noted that in both the present (Fig. 16) and previous flame sampling experiments, the CO concentration was derived on the basis of the measured m/e 12 ion intensity. Because of the extremely small intensity of this ion, the results are subject to a relatively large experimental error. More importantly, the derivation assumes that all of the observed m/e 12 ions (after background subtraction) are derived solely from CO,  $\text{CO}_2$ , and  $\text{CH}_4$ . This assumption is not necessarily correct, of course, and its validity is examined further later in this report in connection with the  $\text{CH}_4/\text{O}_2$  flame data.

Fig. 17 presents the first set of mole fraction data obtained in a  $\text{CH}_4/\text{O}_2$  flame system. Owing to the absence of a buffer gas in this system, such as  $\text{N}_2$

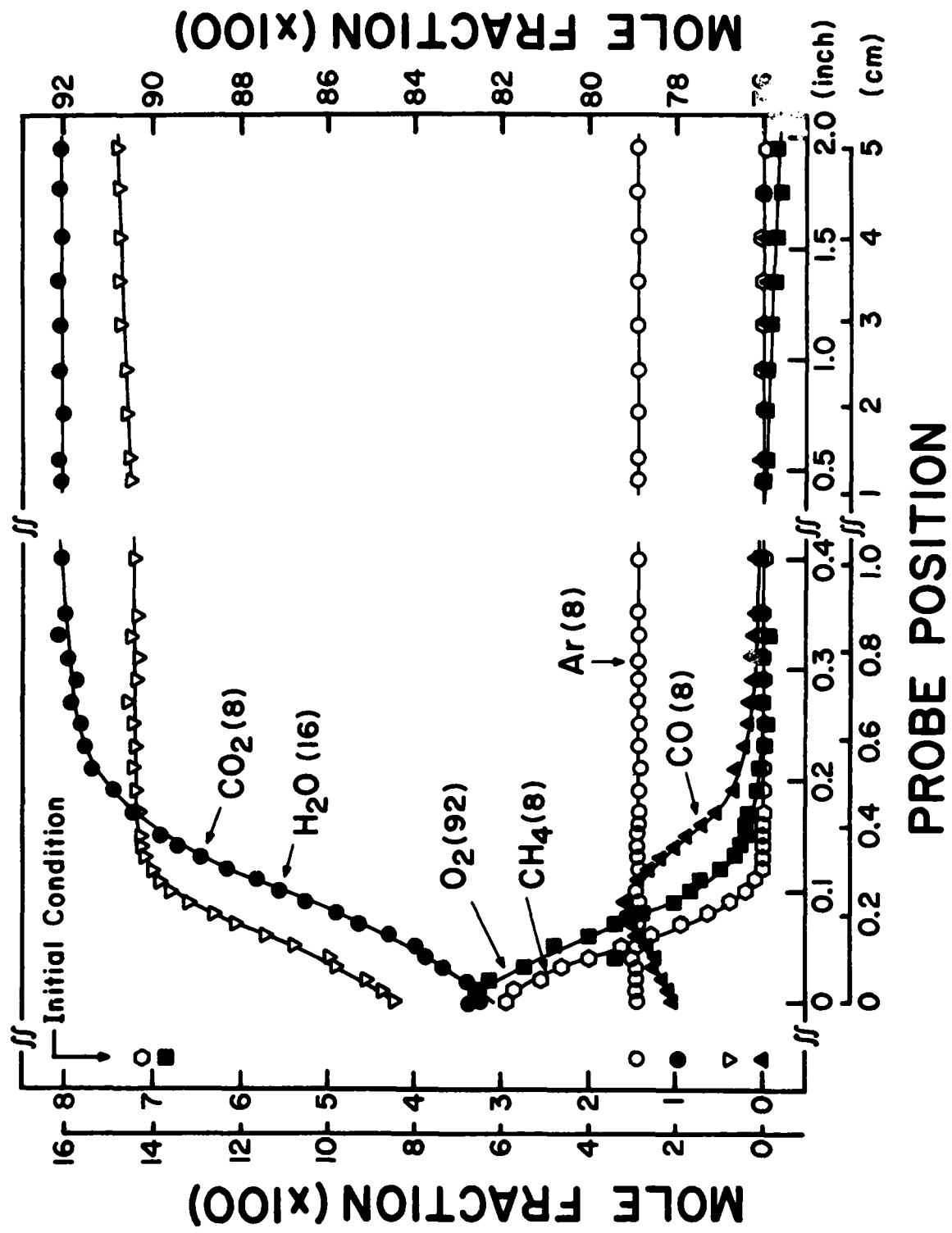


Figure 17. Mole fraction profiles in the methane/oxygen flame. Test No. 2.

in the case of a  $\text{CH}_4$ /Air flame, faster burning is expected here than in systems in which a large quantity of unreactive gas is present. This expectation was confirmed during the present experiments. During this test, the total gaseous flow rate, as well as the burner pressure were adjusted to the same values as were used previously in the  $\text{CH}_4$ /Air flame tests (Fig. 16). It was observed in the  $\text{CH}_4/\text{O}_2$  flame, that the luminous zone begins somewhere below the burner base (porous disk). Consequently, the inner edge of this zone cannot be clearly defined.

The observation with respect to the rate of burning in the  $\text{CH}_4/\text{O}_2$  flame was further confirmed by the observed mole fraction profiles for the products. As shown in Fig. 17, more than 50% of the introduced fuel ( $\text{CH}_4$ ) has been consumed even at the zero probe position. This was accompanied by the formation of  $\text{H}_2\text{O}$  and  $\text{CO}_2$ . In essence, the presently obtained mole fraction profiles yield only a partial picture of the flame structure, since the flame region underneath the porous disk is experimentally inaccessible. This situation can be improved by adjusting the experimental conditions as will be discussed in later.

The mole fraction profile of CO is also shown in Fig. 17. It is seen here that the maximum in the CO mole fraction is only 0.016, which is considerably lower than the maximum value observed in the  $\text{CH}_4$ /Air flame (Fig. 16). This is understandable since CO is a reaction intermediate, the steady-state concentration of which is expected to be much lower when excess oxygen is present, as in the case of the  $\text{CH}_4/\text{O}_2$  system.

The CO mole fraction profile shown in Fig. 17 was derived on the basis of the measured m/e 28 ion signal, after subtracting the contribution to this peak from  $\text{CO}_2$  and from the trace quantity of  $\text{N}_2$  present in the system. This method should afford more accurate determination of the CO concentration, since the observed  $\text{CO}^+$  intensity from CO is much higher in abundance than that of the

$C^+$  ion from CO (which was used in the previous CO concentration determination). The presently used method is also less susceptible to interference, although some  $CO^+$  could be formed from the trace amount of  $CH_2O$  present, which is a known combustion product.

In the present tests, the intensities of both m/e 12 and m/e 28 were measured in order to compare the CO mole fractions determined on the basis of both ion signals. Shown in Fig. 18 is a comparison of the CO mole fraction profiles (presented on a somewhat expanded scale) determined on the basis of these two ion measurements. It is seen that the data based on the m/e 12 ion signal exhibits considerable scatter. However, the agreement between the two sets of data is still reasonably good, especially for the overall peak shapes and the peak positions. The absolute values based on these two methods appear to differ by approximately 20%, which can result from the presence of any other carbon-containing species (soot, radicals, etc.) not accounted for. However, in view of the large experimental errors associated with the m/e 12 measurement, the above conclusion is somewhat ambiguous.

It was mentioned earlier that the mole fraction profiles shown in Fig. 17 correspond to only a portion of the  $O_2/CH_4$  flame. This is due to the fact that the gas velocity above the burner was set too low in comparison with the flame velocity. As a result the flame front propagates backward until it is anchored on the burner base. To alter this situation, the gas velocity must be increased. For a given burner pressure, the gas velocity is increased by increasing the total gas flow rate (in SCCM). Alternatively, for a given total gas flow rate, the gas velocity is increased by decreasing the burner pressure. During the next  $CH_4/O_2$  flame test (No. 3 in Table VII) the gas velocity was increased, both by increasing the total gas flow rate and by decreasing the burner pressure. As seen in Table VII, the total gaseous flow rate was set at 8881 SCCM while the burner pressure was set at 50 torr (0.066 atm). This corresponds to a gas velocity of

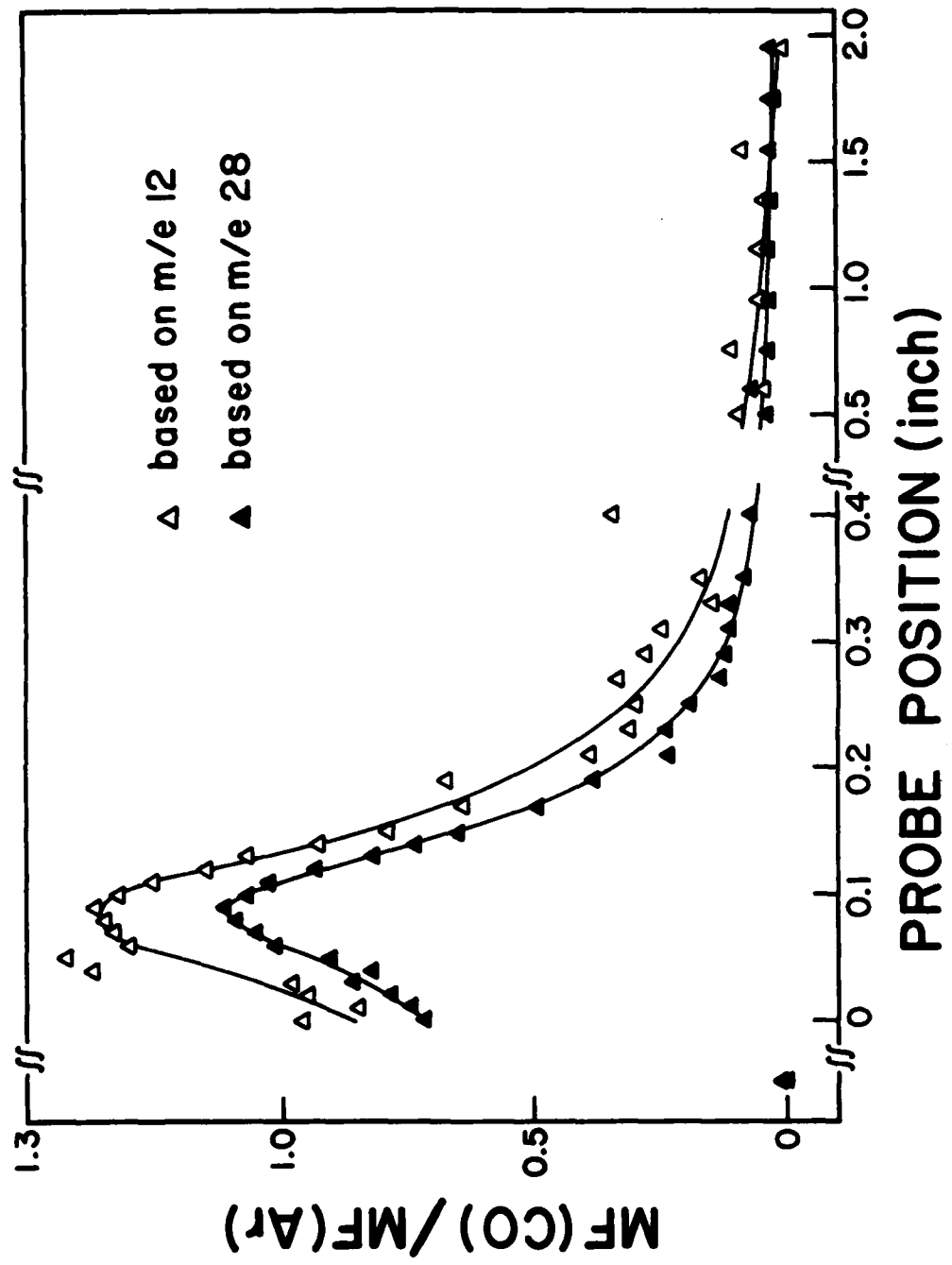


Figure 18. Comparison of the derived CO mole fraction profiles based on two different methods.

71.0 cc/sec. As also seen in Table VII, the initial experimental conditions for this flame test are similar to those reported by Fristrom and co-workers, (also listed in the table). The data obtained in the present study can thus be compared with established literature values. However, there are two notable differences in the initial experimental parameters for the two experiments. The burner pressure used in the present test is 50 torr, whereas that used in Fristrom's study was 76 torr. Also, the burner surface in the present work is 2.5 inches in diameter (the same as for Battelle's burner), which is substantially larger than the burner surface (3.2 cm diameter) used in Fristrom's experiment. As a result, if the burner pressure were set at 76 torr in the present experiment, in order to raise the gas velocity, then the gaseous flow rate would have to be increased to more than 10,000 SCCM, the maximum which can be monitored by the linear mass flow meter used in the present work.

The mole fraction profiles obtained for this  $\text{CH}_4/\text{O}_2$  flame are shown in Fig. 19. It is clearly seen that these mole fraction profiles are markedly different than those presented in Fig. 17. The inner edge of the luminous zone was clearly observable in the flame in this case. Relatively little  $\text{CH}_4$  and  $\text{O}_2$  were consumed, and no combustion products ( $\text{CO}_2$ ,  $\text{CO}$ ,  $\text{H}_2\text{O}$ ) were observed when the probe was placed at the zero position. When the probe enters the flame zone, the mole fractions of both methane and oxygen are sharply decreased, with concurrent increases in the  $\text{H}_2\text{O}$  and  $\text{CO}$  mole fractions. The  $\text{CO}$  product is subsequently oxidized further to yield  $\text{CO}_2$ . As observed in the  $\text{CH}_4/\text{Air}$  flame system, the position of the peak of the  $\text{CO}$  mole fraction profile generally corresponds to that at which the  $\text{CH}_4$  fuel is completely consumed and the  $\text{H}_2\text{O}$  mole fraction profile reaches a steady level. The decrease in the  $\text{CO}$  concentration also corresponds to the increase in the  $\text{CO}_2$  profile, although this was not observed in its entirety.

It should be noted that the mole fraction profiles obtained by Fristrom and coworkers (13) are also reproduced in Fig. 19 (dashed-curves) for direct com-

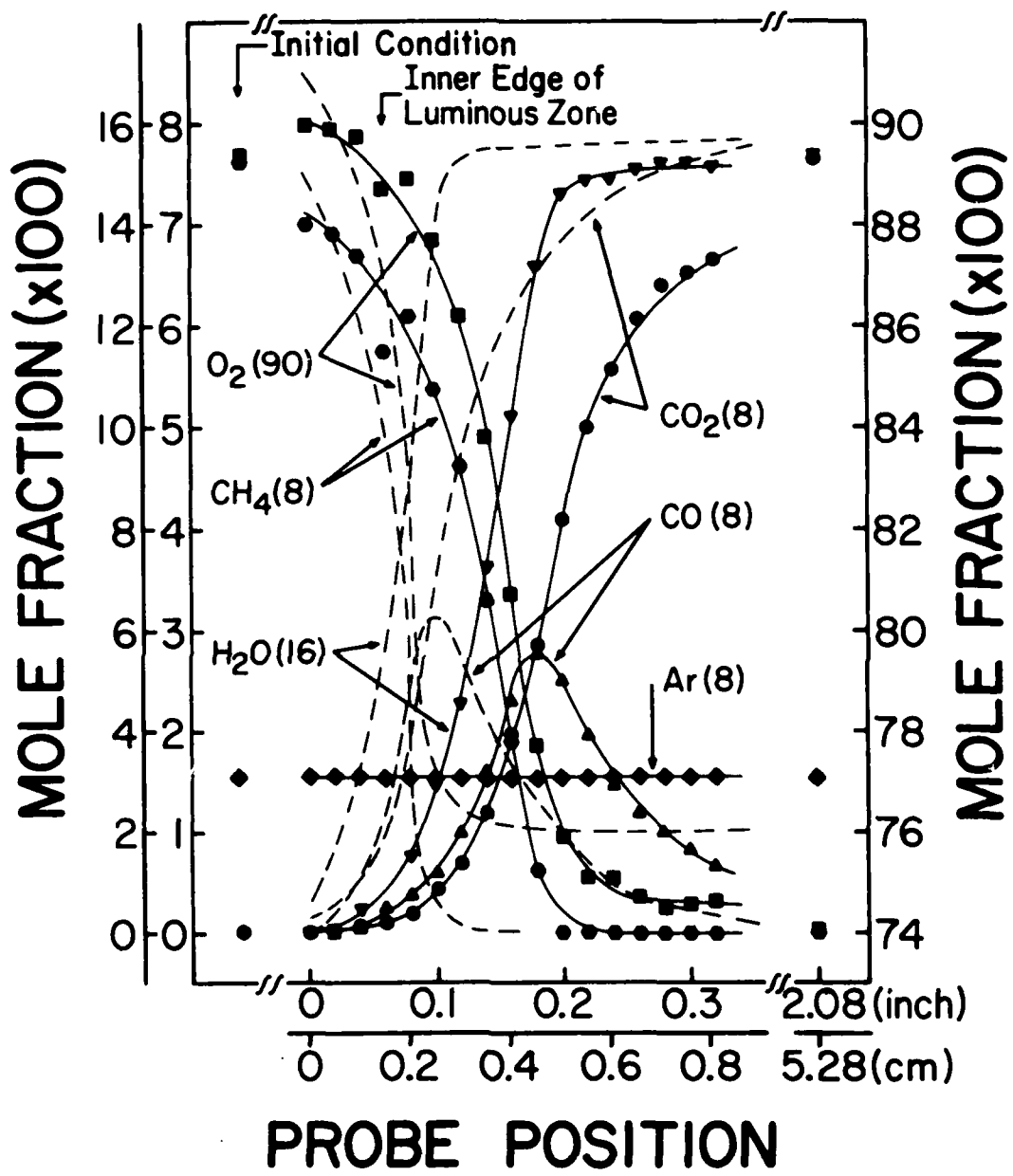


Figure 19. Mole fraction profiles in the methane/oxygen flame. Test No. 3.

parison with those observed in the present measurements. It is seen here that the overall patterns of those two sets of profiles are remarkably similar, except for the fact that the distribution of the profiles in the present flame is considerably broader. Clearly, this is due to the large differences in the burner pressures (50 torr vs 76 torr) used in these two experiments. It is well known that the flame thickness is approximately inversely proportional to the burner pressure. A discussion of the errors in the present flame species concentration measurements is presented in Appendix F.

## V. GAS SAMPLING PROBE SYSTEM FOR RAMJET COMBUSTOR SAMPLING - THEORETICAL ANALYSIS

### A. Introduction

Undoubtedly, most previously accomplished measurements of gas species concentrations in combustion environments have involved some type of probe measurements, in which a portion of the gas was sampled or withdrawn from the combustion environment for analysis. However, probe sampling methods are not entirely without problems. Although sampling of a simple flame using a quartz microprobe is generally considered to yield reliable and valid data (16), questions have been raised with respect to the use of a conventional water-cooled metal probe in a complex combustion environment such as that present in a ramjet combustor flowfield. It has been reported that the concentration data obtained for CO (17) and nitrogen oxides (17, 18) using various types of probes in an otherwise identical combustion environment are inconsistent. The sources of these discrepancies are hard to pinpoint, but may be due to aerodynamic or thermal effects, and/or to inadequate quenching, surface catalysis, or other factors associated with the inherent design of the probe.

Sampling probes traditionally used in combustor sampling are generally of the isokinetic type (19) so that the sampling rate corresponds to the streamline flow and thereby minimizes flow disturbance. However, this type of probe measures the flux, and is not a point measurement device. Recent research (20) indicates that in many sampling environments, inadequate quenching is often a

more serious problem than that of flow disturbance. For this reason, a probe of aerodynamic design has become the preferred type more recently (20). This type of probe consists of an aerodynamic sampling orifice which results in rapid quenching of the sampled gas in the critical sampling tip region. The effective quenching rate is often two orders of magnitude or more greater than that achievable by convective cooling (20). All chemical reactions of the sampled gas are essentially frozen as a result of this rapid quenching, and thus the probe is, for all practical purposes, a point measurement device. Unfortunately, in certain combustion environments, the use of a conventional aerodynamic probe appears to be impractical because of various technical difficulties which arise, such as soot formation. Thus, a probe of isokinetic design (17) must still be used for these applications.

It is believed that many problems associated with the probe sampling methods previously discussed can be eliminated or at least minimized by innovative probe designs. As discussed in more detail later in this report, a radically new probe design was conceived during the course of present research. This probe consists of a quartz microprobe tip coupled with a water-cooled stainless steel body to provide the necessary physical support and protection. With this design, many of the important advantages of a quartz microprobe are retained.

These include the features that such a probe provides, namely, ideal nozzle configuration for rapid quenching, lower soot accumulation, highly inert surface, and minimum thermal effects. Presented in the rest of this section is a theoretical analysis of this probe, while the following section will present some experimental aspects of this probe system and its application for ramjet combustor sampling.

#### B. Analysis of the New Probe Design

Presented in the following is a theoretical analysis of the new probe design, in connection with its use for sampling a hostile combustion environment, which

is characterized by high temperature, high gas velocity and high pressure, as is typically the case in a ramjet combustor flowfield. A detailed account of this analysis is presented in Appendix I to IV, so only a brief summary will be provided here. Emphasis is placed on interpretation of the results of this analysis to gain insight into the potential improvements which can be made in order to minimize the problems associated with the probe sampling technique.

The first part of the analysis deals with the characterization of the flow-field within the new probe sampling system, with reference to a typical ramjet combustion environment. Shown in Fig. 20 is a schematic representation of this system and the calculated profiles of the gas velocity ( $V$ ), temperature ( $T$ ), pressure ( $P$ ), and density ( $\rho$ ), along the entire sampling path. The sampling probe is assumed to consist of a quartz microprobe (between points "b" and "d") and a stainless steel body (between "d" and "e"). The entire wall of the body section is maintained at a constant temperature of 150°C. The probe has a sonic sampling orifice (at "b") with an assumed orifice diameter of 0.015 inch. This probe is placed in a combustion flowfield with conditions as defined in the figure. The sampled gas, after traveling the entire length of the probe, will enter the detector (mass spectrometer) which is located in the vicinity of point "e". The gas at point "e" is also assumed to be directly accessible to a pumping system.

In the probe sampling system described, all incoming gas will pass through five distinctively different regions before reaching the detector. These five regions are represented by a-b, b-c, c-c', c'-d and d-e, as shown in Fig. 20 in relation to the sampling probe configuration. Owing to the strong suction exerted by the sampling orifice (point b), it can be calculated that all incoming gas that passes through an imaginary disc having a diameter of 0.037 inch, at "a", will be deflected toward the center line. Calculations also indicate that the range of this flow field disturbance (that is, between "a" and "b") is 0.033

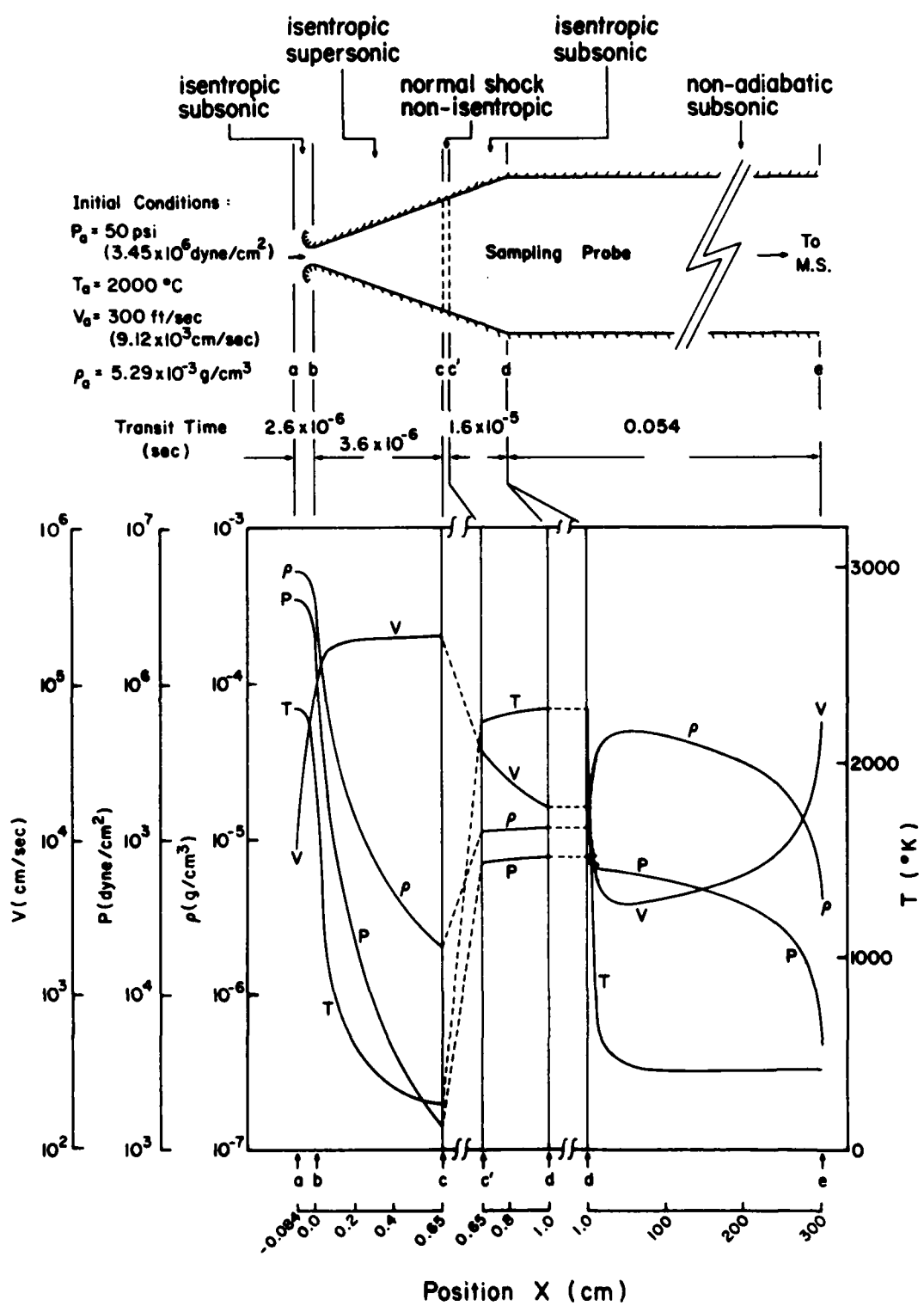


Figure 20. Schematic Diagram of the Gas Probe Sampling System and the Profiles of the Gas Velocity, Temperature, Pressure, and Density of the Sampled Gas Within the Probe Sampling System.

inch, which is approximately two times larger than the diameter of the probe orifice. Within this region, the velocity of the gas will be rapidly increased, with a concurrent decrease of the gas density, pressure and temperature, in an isentrophic process. Eventually, all of this gas will pass through the sampling orifice at point "b".

It has been shown experimentally (16) that a quartz probe orifice constructed by a standard fabrication process closely resembles an ideal nozzle, which means that the gas velocity at the orifice will reach sonic velocity in an isentropic process, provided that the down stream pressure conditions can meet a given requirement. The gas sampling rate can be readily calculated to be 0.0333 g/sec under the present sampling conditions. The temperature, velocity, density and pressure of the sampled gas at point "b" can also be determined as shown in Fig. 20. The gas transit time within the region (a-b) can then be calculated to be  $2.6 \times 10^{-6}$  sec. It can be shown that the gas sampled within this interval has been aerodynamically cooled at a rate of  $1.5 \times 10^8$  °K/sec, which is in good agreement with a reported estimated value of  $\sim 10^8$  °K/sec (20).

Due to the geometry of the nozzle, once the sampled gas passes through the orifice, it further experiences an aerodynamic expansion with a rapid increase in velocity (supersonic), at the expense of the gas temperature, in an isentropic process. Eventually, a point is reached ("c"), beyond which no further increase of velocity can be sustained, and a series of non-isentropic shock waves are initiated. In the region following this shock (c-c'), the gas velocity is restored to subsonic speed, which is accompanied by a sharp rise in the gas temperature, pressure and density.

It is assumed that the sampling probe head has a simple cone-shaped configuration. This information, used in combination with the equations of conservation of energy and mass, and the standard equations for a normal shock and isentropic flow, allows the exact location of the shock to be determined, and the flowfield within the regions b-c, c-c' and c'-d to be characterized. The results of these

calculations are shown in Fig. 20, along with the calculated gas transit times within these regions.

The assumption of an isentropic process is no longer valid once the gas passes point "d", beyond which the gas temperature will be gradually cooled by the probe wall, which is maintained at a constant temperature of 150°C. The gas flow within the entire region between "d" and "e" is largely viscous, and is dictated by the probe line configuration and the pumping system. The cooling of the sampled gas (by wall-convective cooling) in this region can be treated quite accurately as an incompressible laminar flow, for which the Nusselt number is known to be 3.658. This allows the derivation of the gas temperature profile within the region, taking into account the variation of the thermal conductivity as a function of the gas temperature.

From the known gas temperature profile, the distribution of the gas pressure along the transfer line (d-e) can also be derived, by using Poiseuille's law in its basic form, allowing for the variation of the gas viscosity with respect to the gas temperature. The initial drop of the gas pressure, shown in Fig. 20, within the first few centimeters, is due to the cooling of the gas by wall convective cooling, while the broad decrease of the pressure in the latter portion is largely due to the pumping action at the outlet (point "e"). To complete the calculation, the profiles of the gas density and velocity within this region are subsequently obtained from the equation for an ideal gas and the continuity equation, respectively.

The flowfield characterization derived from these calculations, as shown in Fig. 20, provides a detailed understanding of the sampling in the probe system described. The results of this characterization also provide a basis for the evaluation of various effects, including the aerodynamic disturbance, thermal disturbance, and reaction quenching, on the validity of the gas species concentration measurements. In the following a general discussion of the effectiveness of this probe design in resolving several of these potential problems is presented.

Emphasis is placed on the understanding of the significance of these problems, with respect to applications of the proposed probe sampling system for a high-temperature and high-pressure combustion environment.

As seen in Fig. 20, the existence of the probe in the combustor flow field does cause a certain degree of aerodynamic disturbance in a region immediately in front of the probe aperture. This region extends upstream a distance approximately twice the length of the aperture diameter, and encompasses a cross sectional area having a diameter approximately twice the aperture diameter. Within this region the flow is significantly distorted, while the gas velocity is substantially increased, with a concurrent decrease of the gas pressure, density and temperature. Obviously this will have a pronounced effect on the chemical reactions occurring within the combustor gas in this region. Further upstream from this region, the flow is largely undisturbed, just as if no probe were present. Of course, the presence of the probe will cause the gas flow in the region surrounding the probe to be disturbed to some degree. But this disturbance is generally not "seen" by the probe because the disturbed gas will not be sampled by the probe aperture, provided that the probe is placed in line with the combustion gas flow. However, in a highly turbulent region, additional sampling errors may be induced by this type of disturbance.

The best way to reduce the aerodynamic disturbance effect of course, is to reduce the probe aperture and utilize a probe having a very slender body. With the present quartz microprobe design, the size of the aperture can be readily maintained at 0.010 inch or less without encountering problems such as blockage of the aperture by soot. This corresponds to a flow disturbance region less than 0.02 inch, which does not appear to be significant.

With respect to the problem of quenching, substantial improvement is also achieved with the present probe design, since it utilizes a sampling aperture having an ideal nozzle configuration. Rapid quenching due to aerodynamic cooling

in the critical sampling front should essentially freeze all chemical reactions, once the sampled gas passes through the probe aperture. Even after the sampled gas enters the post-shock region, reactions of the gas should not be reinitiated to any significant degree, despite the sharp rise in the gas temperature. As seen in Fig. 20, the gas pressure within this region is approximately 1-2 orders of magnitude smaller than that of the combustion environment. This translates into a reduction of 2-4 orders of magnitude in the chemical reaction rates for most bimolecular reactions.

As seen in Appendix III, the problem of quenching in the new probe system was further evaluated, using CO afterburning as an example. Based on the result of the present flowfield characterization, and the known oxidation rate of CO as a function of temperature and pressure, it was shown that the measured CO concentration will correspond to the true average concentration of CO within a sampling zone which has a diameter of 0.037 inch and a thickness of 0.009 inch, and which is located 0.022 inch upstream of the probe aperture. This result was obtained by assuming a well-defined streamline flow of the combustion gas in line with the probe. But it is also applicable, without significant error, for a highly turbulent flow, provided that the flow velocity is significantly less than sonic velocity.

It is interesting to note that this sampling zone coincides approximately with the onset of the aerodynamic disturbance region previously discussed. This means that there is really no sampling error caused by the aerodynamic disturbance in the proposed sampling system, since the flow disturbance in this very region has been taken into account explicitly in the determination of the sampling zone, and, in addition, there is no further aerodynamic disturbance upstream from the sampling zone. This concept of the sampling zone will be similarly applied in the consideration of the thermal effects in the probe, which are discussed next.

A major concern in the use of a sampling probe, especially a water cooled

probe, is that the probe represents a heat sink which can perturb the temperature distribution around the probe area. This perturbation produces changes in chemical reaction rates, which results in changes in species concentration profiles. Prior to further discussion of these thermal effects, a conceptual distinction should be made between the thermal effects in the sampling zone and the thermal effects in the "pre-sampling" zone (that is, the region upstream from the sampling zone). Any cooling of the gas in the sampling zone due to thermal effects is actually a desirable feature because the probe is intended to sample the gas within this region. It is desirable that when the gas has entered this zone, a sharp drop in the gas temperature occur, such that no further change of the gas composition will occur thereafter. However, thermal effects in the pre-sampling zone are undesirable, because these may alter the composition of the gas before it enters the sampling zone. Cooling of the gas in the presampling zone in the presence of a heat sink (such as a probe) can occur as a result of thermal conduction, convection, and radiation. In view of the high-pressure, high mass flow which is typical of an operating combustor, the net effect on the gas temperature distribution which results from these three heat transfer mechanisms may be quite different from that of a low-pressure and low mass-flow flame.

Considering first conduction cooling, it is known that the heat flux per unit area transferred from the gas in the presampling zone to the heat sink (probe) is the same for a given temperature gradient, regardless of the pressure. This flux may be quite significant in a low-pressure flame and can cause a substantial drop in the temperature of the presampling zone. However, the same flux will cause hardly any temperature drop in the presampling zone in the present case, because of the much higher pressure and mass flow normally encountered in a combustor system.

On the basis of similar considerations, it can be shown (see Appendix III) that the cooling in the presampling zone due to heat transfer by radiation is also

insignificant in a high-pressure combustion system. According to the basic law of radiation (Beer's Law), the attenuation of radiation through a gas medium is proportional to the pressure of the gas medium. It has been reported (20) that the disturbance of the gas temperature profile in a low pressure flame (<0.1 atm), as a result of the presence of a probe, can extend to a region about 5 mm from the probe. This means that the same disturbance, if due to radiation effects, could extend no more than 0.05 mm. from the probe, in the present high-pressure combustion environment. This length is considerably less than the resolution achievable with the probe, which is dictated primarily by the aerodynamic sampling environment.

Cooling of the presampling region as a result of convection is not a problem in the present case, since, in a streamlined flowfield, it is assumed that once the bulk flow of the gas leaves the presampling region, it will no longer return to the original region. However, for gas sampling in a recirculation region, the above assumption is no longer valid, and a portion of the sampled gas may have come into contact with the probe wall before entering the sampling orifice. If the probe wall is maintained at a very low temperature, as is typically the case in a conventional water-cooled metal probe, significant premature cooling of the sampled gas will likely have occurred, which will undoubtedly affect the validity of the sampling data. On the other hand, in the sampling system described here, the temperature of the quartz probe can be maintained at a much higher value (typically 1500°K - 2000°K). The problem of premature cooling due to convection can thus be largely minimized, although not entirely eliminated.

Problems arising from surface-induced composition changes (such as surface catalysis) are also a prime concern for probe measurements. The significance of these effects is largely dependent on the nature of the species and cannot be generalized. Considerable research has been devoted to the complex subject of the catalytic activity of various probe materials (21, 22). The general consensus is that quartz exhibits a lower catalytic activity, and is therefore a preferred

material for the probe. This is one of the major reasons for the use of quartz in the sampling probe described here.

The formation and accumulation of soot on the probe can also seriously degrade the sampling efficiency. The aperture of the probe can be virtually plugged if a large quantity of soot is allowed to accumulate at the probe's orifice. This problem has resulted in various compromises in probe designs (17). Quartz, because of its surface smoothness, higher working temperature, and above all, its remarkably low surface affinity, is a much better probe material, with respect to the problem of soot accumulation, than is metal. This was experimentally verified in tests in which a quartz probe and a stainless steel probe were compared by inserting both into a Bunsen burner flame, which was deliberately adjusted to produce a large quantity of soot. After immersion in such flame for a period of 20-30 minutes, the stainless steel probe was almost completely plugged with carbon deposits, while the quartz probe was essentially clean and free of any soot accumulation.

## VI. GAS SAMPLING PROBE SYSTEM FOR RAMJET COMBUSTOR SAMPLING - SOME EXPERIMENTAL ASPECTS

### A. Description of the Probe

The next task undertaken as part of the combustor sampling project was the development of gas sampling probes for in-situ sampling of gaseous species in a hostile combustor flowfield. Proper design of this system is important from both practical and theoretical viewpoints. As already mentioned, many factors associated with the design of such probes, including physical strength, chemical inertness, cooling capacity, and resistance to soot formation must all be considered and adequately taken into account. Also, various aerodynamic, thermal and chemical effects caused by the presence of the probe in the combustion plasma must be minimized in order to assure the validity of the sampling data obtained. No prior probe design has adequately satisfied all of these

requirements, and development of an acceptable probe thus represents a major challenge in this program.

In the course of our previous efforts to develop a superior sampling probe several novel improvements in design were conceived. A probe was developed which consists of a quartz section as the tip, coupled with a water-cooled stainless-steel body to provide the necessary mechanical strength and protection. The choice of a quartz microprobe tip was largely based on consideration of the several important advantages which are thus realized, including the capacity for rapid quenching, minimization of soot formation, surface inertness, less severe thermal perturbations, and superior sampling resolution. However, there are also some inherent problems associated with the use of the quartz microprobe tip, which include difficulties in achieving leak-tight coupling to the probe body, fragility of the quartz materials, and high temperature resistance, which must be solved before such a probe can be successfully applied for combustor sampling.

After a series of probe torch test evaluations, which will be discussed later, and which suggested several other improvements, a design finally evolved for a probe which exhibits considerable promise for adequate performance in combustor sampling. A schematic diagram of this probe is shown in Fig. 21. It consists of three main sections. The first section is a quartz microprobe tip which can be readily fabricated using a commercially available quartz male joint. The second section is an L-shaped stainless-steel probe body, which consists essentially of two concentric tubes. Two cooling water inlet coils are located within the space between these two tubes. The front end of the inner tube is in the form of a female tapered joint. A threaded stainless-steel base is sealed to the two tubes using a high temperature nickel brazing material as indicated in Fig. 21.

To assemble this probe the quartz microprobe is inserted into the cavity

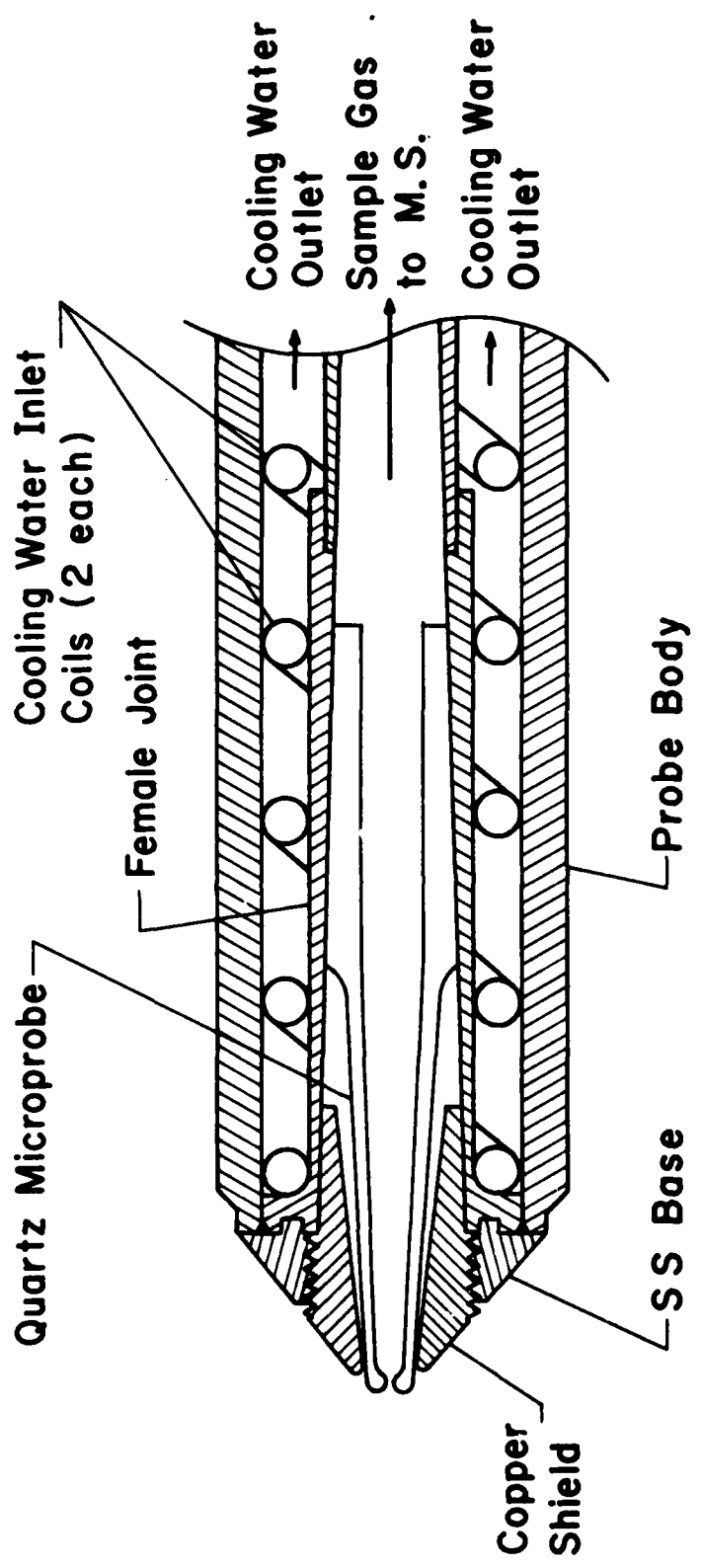


Figure 21. Schematic of the quartz/S.S. sampling probe

provided by the female joint of the metal probe body. A copper shield, which is the third section of the probe assembly, is then inserted into the same cavity forming a protective shield for the quartz microprobe tip. It is noted that the lower portion of the copper shield is tapered, so that it mates closely with the female tapered section of the probe body. This close contact facilitates efficient cooling of the copper shield during a sampling experiment.

Unfortunately after the fabrication of this probe had been completed, a water leak developed in the cooling coil in the lower part of the female joint. Although this leak was subsequently repaired by using a short stainless-steel sleeve, the female joint became partially damaged in this process, and the seal between the metal joint and the probe tip was no longer tight. As a result, it was necessary to use several Viton O-rings to effect a good seal between the quartz microprobe and the probe body.

A series of torch tests were conducted to examine the durability of this new probe under various heating conditions. In these tests, a torch flame was brought into contact with various portions of the probe. A thermocouple wire was placed at the probe wall immediately following the heating area to monitor the probe wall temperature for each heating and cooling cycle. A second thermocouple was also placed at the water return line to monitor the overall heat exchange rate. Distilled water at a flow rate up to 200 cc/min was allowed to circulate through the cooling loop of the probe. The sampling line was connected to a vacuum pump during these tests to simulate sampling by the probe.

Two types of torches were used in the present study. The first one was a portable propane-air torch which provide a concentrated flame in a small area. The second torch was a methane-oxygen torch normally used in a glass fabricating shop. With adequate methane and oxygen flow rates, the latter torch provided a flame large enough to encompass the entire probe front. The maximum temperature attainable at the flame tip with such torches has been reported to be more than

2000°C (3600°F), which is approximately the temperature which prevails in a ramjet combustion chamber. However, in terms of the localized heating rate, conditions in the combustion chamber environment are still more severe than those approximated by the torch because the ramjet combustion is normally conducted at much higher pressures and gaseous flow velocities.

Numerous torch tests, such as those just described, were accomplished in the preliminary assessment of the new probe and these tests resulted in several refinements in the probe design. The results of these tests have been described in detail previously. In this report, only a brief description on the result of one such torch test will be provided. The probe used in this torch test was subsequently employed for actual ramjet combustor sampling. Prior to the torch test, the probe was assembled so that its configuration was essentially the same as shown in Fig. 21, except that the seal between the quartz microprobe and the probe body was achieved by using a set of three Viton-O-rings, as mentioned earlier. These O-rings were carefully positioned to minimize the contact between the sampled gas and the O-ring body. The front end of the quartz tip was in direct contact with the copper shield and extended outward from the copper shield a distance of about 0.3 mm. The aperture of this probe was approximately 0.5 mm. diameter. The flow rate of the cooling water in this case was set at 200 cc/min.

The torch used for this test was the oxygen-methane torch which, as already noted, has a flame large enough (12 in.) to encompass the entire front portion of the probe. Twelve torch test heating runs were conducted in all, each test lasting at least 2 minutes. The parameters varied during these tests included the length and heating rate of the flame, the location of the torch flame (including distance and orientation) relative to the probe, the downstream pumping conditions, and the duration of heating.

After the 12 heating tests, no apparent damage to the probe body or the copper

AD-A114 854 WRIGHT STATE UNIV DAYTON OHIO  
MASS SPECTROMETRIC MEASUREMENTS OF THE CONCENTRATIONS OF GASEOU--ETC(U)  
APR 82 C CHANG, T O TIERNAN

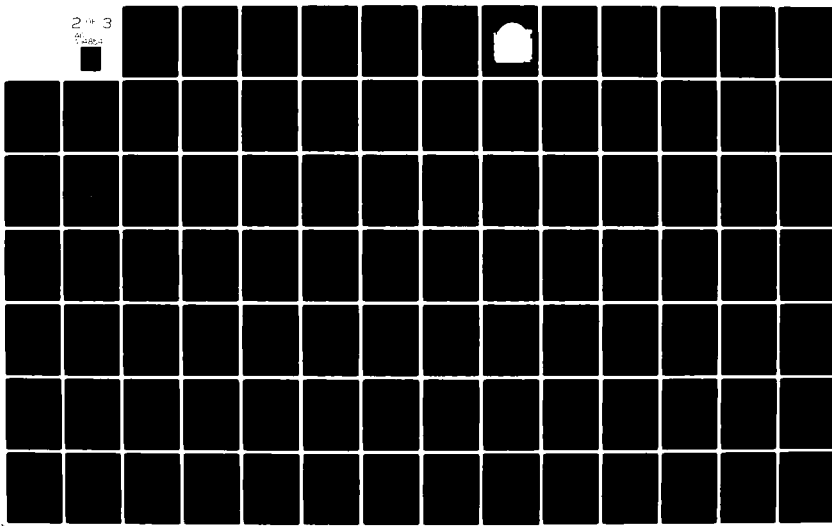
F/G 7/4  
F33615-78-C-2066

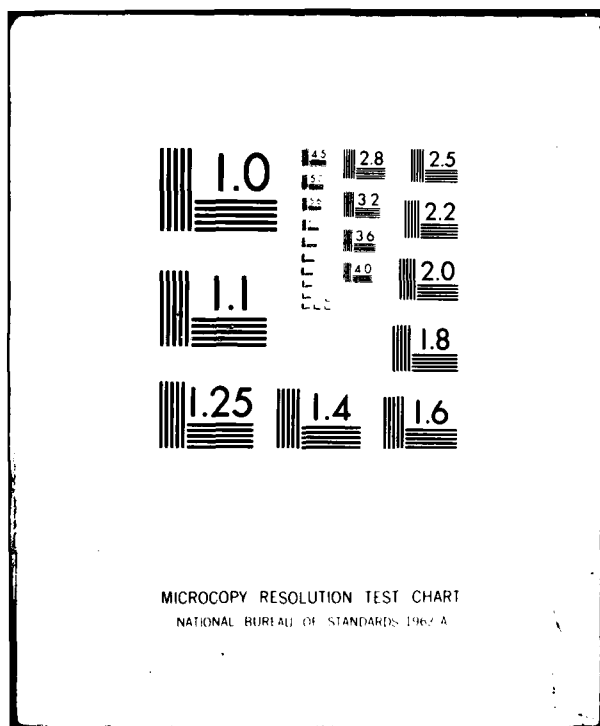
AFWAL-TR-81-2139

ML

UNCLASSIFIED

2 + 3  
M  
14854





shield was visually observed. The copper shield showed no indication of melting during the heating. The maximum detectable temperature of the probe wall approximately 2 inches below the torch flame was 100°C during the heating procedure.

The exposed portion of the quartz section remained colorless during most of the torch heating process, but the extreme end of the tip became slightly red in color when the intensity of the torch flame was increased. This observation suggested that the temperature of the glass tip was probably higher than 1000°C. Such a high temperature is actually desirable because, under such conditions, the probe tip will not be an effective heat sink during gas sampling. However, during the last torch test run, which lasted for more than 5 minutes and during which the flame intensity was at a maximum, the outer layer of the quartz tip became bright red in color and the aperture size was reduced to less than 0.25 mm diameter (from 0.5 mm). This observation apparently indicated that a further increase in the cooling capacity of the probe is needed.

It is also interesting to note that after the initial reduction in the size of the probe tip aperture, the orifice did not change further upon continued heating at the maximum heating rate attainable with the torch. This suggests that after the initial softening of the probe tip, it conformed better to the copper shield. This apparently resulted in closer contact between the probe tip and the copper shield, which in turn improved the cooling efficiency of the probe tip. Upon close examination under a microscope, the probe tip aperture was observed to be very symmetric and round, which indicates that it should behave as an ideal aerodynamic sampling orifice. This somewhat unexpected finding indicates that torch heating of the probe can actually be used as an effective preparation procedure for the newly assembled probe prior to use in actual sampling. It is not yet clear, however, whether or not this procedure can be accomplished in a reproducible manner.

### B. Combustor Batch Sampling and Analysis

Prior to the application of the in-situ, on-line mass spectrometer gas sampling system to the APL ramjet combustor, it was desirable to conduct several preliminary combustor sampling tests in an off-line mode. For these experiments, gases from the combustor were simply sampled through the sampling probe and collected in a sealable bottle, which was then transported to the mass spectrometer analysis system at a later time and analyzed. Compared with on-line sampling, the analysis of batch samples collected off-line is obviously much more tedious and error-prone. Therefore this type of analysis was only conducted on a short-term basis, the main purpose being to evaluate the overall performance of the sampling probe system rather than to obtain an accurate quantitative analysis of the combustor species.

Fig. 22 shows a schematic illustration of a portable batch-sampling system which was constructed and interfaced with the ramjet combustor located in Bldg. 18 of AFAPL. In this system, the sampling probe is mounted on a flange which is inserted between two sections of the combustor. Since such combustor sections are available in various lengths, it is possible to place the probe flange at any one of several different locations with respect to the combustor configuration. It is seen from the schematic (Fig. 22) that the probe is confined and sealed within a Conax fitting so that it can be moved horizontally. This fitting is fastened to a flange, which, in turn, is fastened to a mounting block. A position indicator will be provided to permit determination of the position of the probe. The lower end of the sampling probe is connected to a flexible tube which, in turn, leads to a vacuum line. The vacuum line incorporates a mechanical pump, vacuum joints, solenoid valves, and a pressure gauge, as well as several reservoirs for collecting the sampled gases. For water-cooled sampling probes, a distilled water cooling system is also provided, which consists of a 20 gallon water reservoir, water pump and motor, water pressure gauge, safety switch, flow meter, filter and plumbing lines.

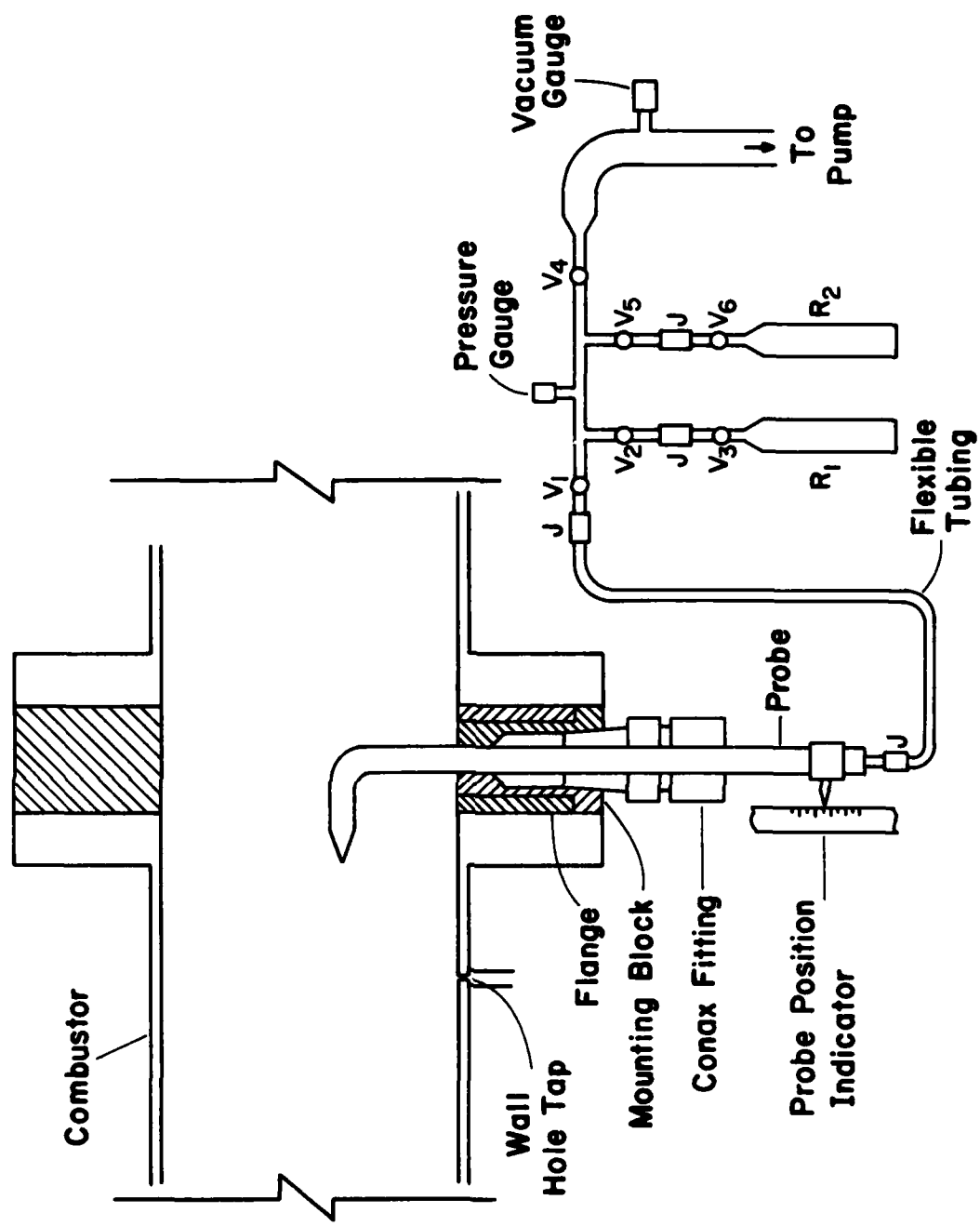


Figure 22. Schematic of the Batch Combustor Sampling Stand.

Samples collected in the reservoirs during the ramjet combustion test are analyzed in batch mode using the mass spectrometer which is currently located at Bldg. 450. In order to facilitate this batch mode analysis, a new sample inlet system was constructed. A schematic diagram of this system is shown in Fig. 23. As seen in this figure, the sample reservoir, as well as all the sample transfer lines, are located within an oven. The temperature of this oven can be controlled accurately over the range from ambient to 140°C, which is necessary in order to assure that all the components (such as fuels) are properly vaporized before being introduced into the mass spectrometer for analysis.

With the present sample inlet system the sample in the reservoir can be analyzed by either of two methods. The first method simply entails introduction of the sample into the mass spectrometer for analysis. The rate of sample introduction is controlled by a metering valve which is located within the oven. This method depends solely on the mass spectrometer for the sample analysis. However, the mass spectrometer presently employed is incapable of measuring certain components such as CO with high precision. This is due to the fact that the major ion produced from CO is  $\text{CO}^+$  (nominal m/e = 28) which cannot be resolved from the ion  $\text{N}_2^+$  (nominal m/e = 28), which results from  $\text{N}_2$ , by the quadrupole mass spectrometer used in these studies. (Resolution of these ions requires a higher resolution mass spectrometer.) It is thus desirable that, prior to mass spectrometric analysis, the CO component of the gaseous mixture be separated from the  $\text{N}_2$  component. This separation is most readily accomplished by using a gas chromatographic column. Such a column is normally a simple glass tube which is packed with solid sorbent materials such as molecular sieves or Porapak Q, or a combination of these. The sorbents mentioned are known to provide good separation of CO from  $\text{N}_2$ ,  $\text{CO}_2$ ,  $\text{O}_2$  and common hydrocarbons (23, 24). The second sample analysis method thus entails the use of a gas chromatographic (GC) column which is directly interfaced with the mass spectrometer (GC-MS). As seen in Fig. 23, this GC

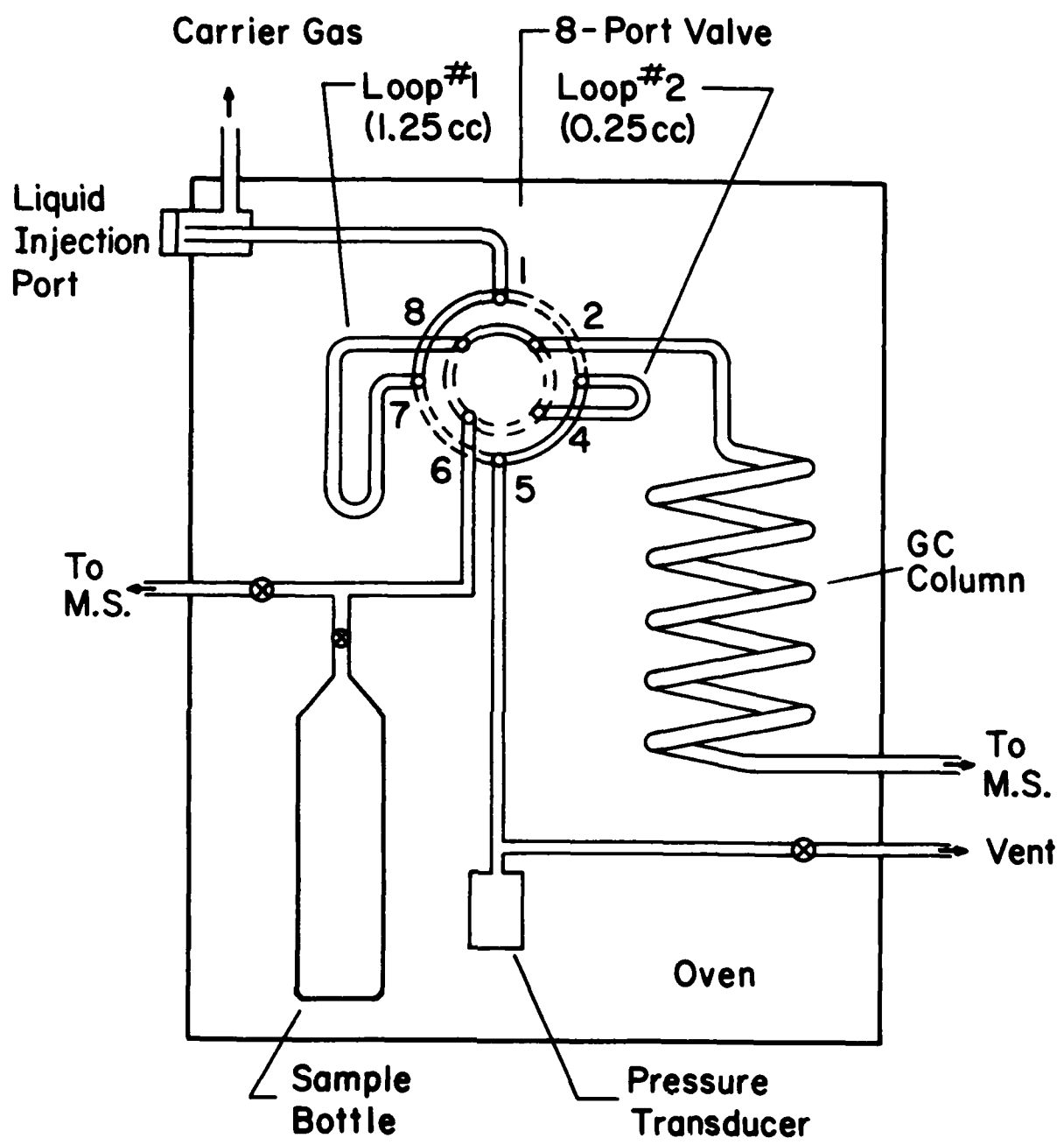


Figure 23. Schematic of the sample inlet system.

column is also located within the oven. To properly transfer the sample onto this column, an eight-port valve (also located within the oven) is employed. Attached to this valve are two sampling loops of known volume (0.25 cc and 1.25 cc). Prior to the analysis, a predetermined quantity of sample from the reservoir is transferred to one of these loops. This sample is subsequently swept out of the sample loop and carried onto the GC column by a carrier gas (typically helium). The components of the sample are separated as they migrate through the GC column and are then individually detected by the mass spectrometer.

### C. Experimental Results.

Toward the end of present contracting period, a ramjet combustor sampling experiment was carried out using the quartz stainless-steel probe and the portable batch sampling system, both of which were described in the foregoing sections of this report. The combustor test facility (5) is essentially a coaxial dump combustor which consists of a 6 in. I.D. x 18 in. long stainless-steel combustion chamber, an inlet section of 3 in. I.D., and a nozzle of 4.24 in. I.D. Liquid fuel (JP4) is injected into the inlet section through a set of 8 injection ports (0.055 in. I.D. orifice) at a point located 4.75 inches upstream of the inlet duct exit. The entire combustor device is mounted on a thrust stand, which permits the absolute levels of thrust of the combustor during the test to be directly measured. This, in turn, yields the total temperature rise across the combustor through which the combustion efficiency can be derived.

A total of six combustion tests were carried out during this sampling experiment. The experimental parameters varied during these tests included fuel/air ratio (0.027 and 0.046), inlet air temperature, and the air mass flow rate. The combustor temperature derived from the thrust measurement ranged from 2360 to 3408°R, while the combustion efficiency was found to vary between 79.9% and 94.4%. During the entire experiment, the sampling probe was placed within the combustion chamber with the probe mounting flange sandwiched between the combustor and the

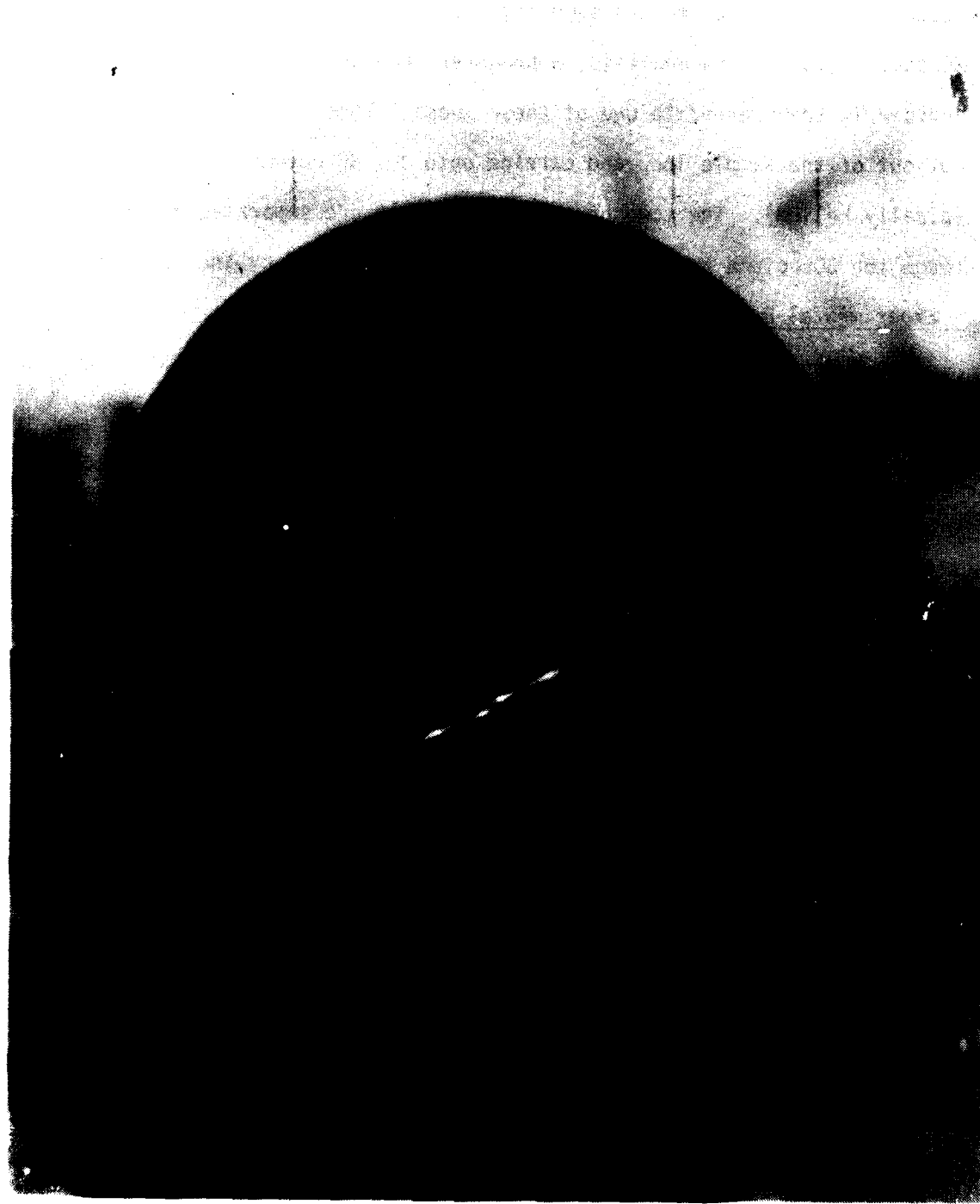


Figure 24. Probe tip photograph of the sampling probe after the ramjet combustor sampling tests.

Description of Figure 24.

Outside Layer: S.S. Probe body

Middle Layer: Copper Shield

Inner Layer: Quartz Sampling Probe Tip (The size of the  
orifice is approx. 0.005" dia. The wire  
with 0.010" dia. is shown for reference) .

exit nozzle. Due to limited number of sample reservoirs available, the combustor gas was sampled only during two of the six tests conducted. For the other four tests, the reservoir inlet valves were closed, although the probe was still located within the combustor, in order to test its durability.

The results of this preliminary combustor probe sampling experiment appear to be quite satisfactory. During each of the six tests, the pressure reading on the vacuum gauge with valves  $V_1$  and  $V_4$  in open position (see Fig. 22) was monitored. No abrupt changes or fluctuations of this pressure were observed, which would have indicated the occurrence of problems such as blockage of the probe due to soot accumulation, or collapse of the probe glass tip due to intensive heating. The highest temperature observed at the probe wall (immediately outside the combustor) was 120°C, and the exhausted probe cooling water temperature was 90°C at the maximum. The sampling of combustor gas into the reservoirs was also accomplished without problems.

Following the combustion tests, the probe was removed from the probe mounting flange for closer inspection. Fig. 24 is a photograph of the front portion of the sampling probe after the combustion tests. It is seen that the quartz microprobe tip remains symmetrically round in shape and free from soot deposits, although at the aperture portion a slight yellow coloration is observed. The diameter of the aperture is approximately 0.005 in., (the diameter of the attached wire for reference is 0.01 in.) virtually unchanged from the orifice size prior to the combustion tests. The copper shield showed no sign of melting or deformation after the test, which indicates that the cooling of this component is adequate. However, the surface of the copper shield was severely corroded. Copper was originally selected as the material for the shield because of its excellent heat conductivity properties. Replacement of the copper with some other more inert material (but with poorer heat conductivity) may necessitate further improvements in the probe design.

Shown in Fig. 25 is the mass spectrum of the sample collected during the combustor sampling test. This spectrum was obtained during the last month of this reporting period and is presented here only to demonstrate the general capability of the present probe sampling system as employed in a real ramjet combustion environment. For more complete qualitative and quantitative analysis further experiments in the future are still required. The mass spectrum shown here covers the mass range up to m/z 250 which is adequate for the analysis of JP4 fuel, since the later has an average molecular weight of 128. The ions observed in the low mass range were identified, as indicated in the figure. Most of the higher mass ions recorded in this spectrum are due to residue gases (from pump oil and/or dirty ion source) rather than the unburned fuel in the collected sample.

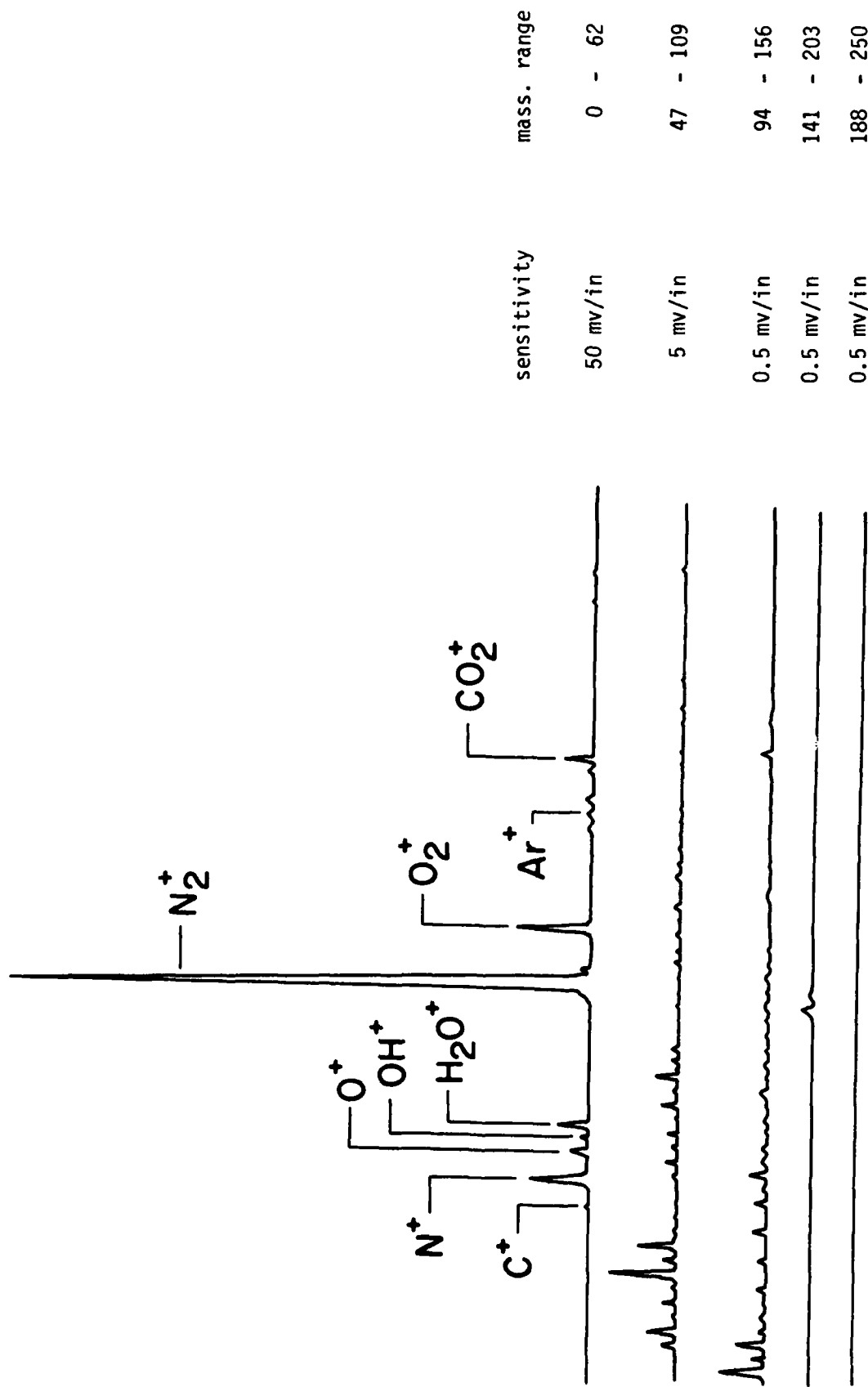


Figure 25. Mass Spectrum of the Ramjet Combustor Gas Sample.

## REFERENCES

1. Stull, F.D., Craig, R.R., and Hojnacki, J.T., "Dump Combustor Parametric Investigations", ASME Fluid Mechanics of Combustion, Joint Fluid Engineering and CSME Conference, Montreal, Quebec, May 13-15, 1974.
2. Stull, F.D. and Craig, R.R., "Investigation of Dump Combustors with Flameholders", AIAA paper 75 - 165, AIAA 13th Aerospace Science Meeting, Pasadena, California, January 20-22, 1975.
3. Craig, R.R., Buckley, P.L., and Stull, F.D., "Large Scale Low Pressure Dump Combustor Performance", AIAA Paper 75-1303, AIAA/SAE 11th Propulsion Conference, Anaheim, California, September 29 - October 1, 1975.
4. Buckley, P.L., Craig, R.R. and Obleski, B.M., "The Effect of Swirl on A Ramjet Dump Combustor", 4th International Symposium on Air Breathing Engines, Orlando, FL., April 1-6, 1979.
5. Craig, R.R., Drewry, J.E. and Stull, F.D., "Coaxial Dump Combustor Investigations", AIAA paper 78-1107, AIAA/SAE Fourteenth Joint Propulsion Conferences, Las Vegas, July 25-27, 1978.
6. Drewry, J.E., "Fluid Dynamic Characterization of Sudden-Expansion Ramjet Combustor Flowfields", AIAA Journal, Vol. 16, April 1978, pp. 313-319.
7. Boray, R.S. and C. Chang, "Flow field Studies of Dump Combustors", Fifth International Symposium on Air Breathing Engines, Bangalore, India, February 16-22, 1981.
8. Viets, H. and Drewry, J.E., "Quantitative Predictions of Dump Combustor Flowfields", AIAA paper 79-1481, AIAA 12th Fluid and Plasma Dynamics Conference, Williamsburg, VA, July 1979.
9. Boray, R.S. and Drewry, J.E., "Experimental Studies of Sudden Expansion Dump Combustor Configuration", AFWAL/PORT (to be published).
10. Chang, C., Sides, G.D. and Tiernan T.O., "In-Situ Measurements of Gas Species Concentrations in Simulated Dump Combustor Flow fields", Air Force Aero Propulsion Lab., AFAPL-TR-76-105, November 1976.
11. Chang, C., Sides, G.D. and Tiernan, T.O., "In-Situ Measurements of Gas Species Concentrations", Air Force Aero Propulsion Lab., AFAPL-TR-78-64, August, 1978.
12. Chang, C. and Tiernan, T.O., "Application of A Sampling Probe - Mass Spectrometric Technique For Measurement of The Concentrations of Gases in Ramjet Combustor Flowfields", 30th Annual Conference on Mass Spectrometry and Allied Topics, Honolulu, Hawaii, June 6-11, 1982.
13. Fristrom, R.M., Grunfelder, C., and Favin, S., J. Phys. Chem. Vol. 64, 1386 (1960).

14. Biordi, J.C., Lazzara, C.P., and Papp, J.F., Combustion Flame 23, 73 (1974).
15. Merryman, E.L., Kircher, J.F., and A. Levy, AFAPL Contract No. F33615-76-M-2103, February, 1977.
16. Fristrom, R.M. and Westenberg, A.A., "Flame Structure", McGraw-Hill, Inc., N.Y. 1965.
17. Clark, J.A., Peters, J.E., and Mellor, A.M., "Probe Effects in Gas Turbine Combustor Emissions Measurements", Technical Report AFAPL-TR-79-2041, 1979.
18. Cernansky, N.P., in "Experimental Diagnostics in Gas Phase Combustion Systems", ed. by B.T. Zinn, Progress in Astronautics and Aeronautics, Vol. 53, 1976, p. 83.
19. Tine, G., "Gas Sampling and Chemical Analysis in Combustion Processes", AGARDograph 47, 1961.
20. Bowman, C.T., in "Experimental Diagnostics in Gas Phase Combustion Systems", Ed. by B.T. Zinn, Progress in Astronautics and Aeronautics, Vol. 53, 1976 p. 3.
21. Sampson, R.J., and Shooter, D., in "Oxidation and Combustion Reviews", Vol. 1, July 1965, p. 225.
22. Shelef, M., Otto, K., and Gandhi, H., J. of Catalysis, Vol. 12, Dec. 1968, p. 361.
23. Marrillet, L., and Tranchant, M., Methods Phys. Anal., 1965, pp. 37-39.
24. Dilorenzo, A., J. Chromatog. Sci., 8, 4 (1970) pp. 224-226.

## APPENDIX A

### OVERALL HEAT TRANSFER CONSIDERATIONS FOR A QUARTZ/STAINLESS STEEL PROBE

In the design of the sampling probe described here, an important consideration is the heat transfer which occurs during the sampling of gaseous species from a combustor, such as the ramjet dump combustor located AFAPL. Adequate cooling of the probe must be provided in order to prevent overheating (and melting) of the probe body, and also, in order to maintain the desired mechanical strength of the probe during sampling. In the present discussion, only the overall heat transfer in the probe is considered. This differs from the heat transfer which occurs solely in the quartz probe tip. During sampling, it is generally desirable that the probe body be maintained at a low temperature through adequate water cooling. On the other hand, the temperature in the quartz probe tip must be maintained at a much higher value (close to, but not above the softening temperature, 1200-1500°C of the quartz probe). This is necessary in order to prevent premature cooling of the gas which is being sampled, that is, so that the probe tip does not act as a major heat sink. By keeping the probe tip very hot, the accumulation of soot can also be prevented.

Heat transfer in the probe described here can conveniently be considered to occur in three phases. In the first phase, heat is transferred from the combustion gas to the exterior wall of the probe. This process is largely dominated by forced convection. In the second phase, heat is transferred from

the exterior probe wall to the interior probe wall, which occurs by conduction. In the third phase, heat is transferred from the interior wall of the probe to the cooling water, again via forced convection.

In order to calculate the heat transfer which occurs in each of these three phases, the temperatures of the interior and exterior probe walls must be known. These two parameters are dependent on the following factors: 1) the combustor operating conditions including pressure, temperature, gas velocity, etc.; 2) cooling water flow rate and inlet water temperature; and 3) physical configuration of the sampling probe, including its size, geometry, material content, etc. All of the above information is known, except for the cooling water flow rate, which is to be determined based on the overall heat transfer rate.

In view of the complexity of the calculation, some simplifications are necessary. It is first assumed that the entire exterior probe wall is maintained at a uniform temperature. Similarly, the temperature is assumed to be the same over the entire interior wall of the probe. These assumptions are reasonable since only the overall heat transfer rate is to be calculated here.

In order to reduce the cooling water load requirement, the flow rate of the cooling water can be adjusted such that the inlet water is at ambient temperature (20°C), while at the outlet, the water can be completely vaporized steam (100°C) at normal atmospheric pressure. Therefore for each cc of water introduced, a total of 160 cal of heat can be carried away. Since the interior

wall of the probe is in direct contact with the cooling water, with very efficient cooling, it is reasonable to assume that the steady state temperature of the probe's interior wall can be maintained at 100°C ( $T_{p,i}$ ). The temperature of the probe's exterior wall ( $T_{p,o}$ ), on the other hand, is more difficult to determine since it is dependent on the overall heat transfer rate to be calculated. As a first approximation, this temperature is arbitrarily defined as 200°C (850°R). The calculated heat transfer rate based on this initial condition is then subsequently tested in an energy balance calculation, from which a better approximation of the  $T_{p,o}$  value is obtained. Similar computational procedures are repeated until an internally consistent value of  $T_{p,o}$  is obtained.

Consider now that the probe is inserted into a ramjet combustor (6" diameter) flow field which is operated with the following parameters:

Combustor pressure ( $P_g$ ) = 50 psi

Combustor gas temperature ( $T_g$ ) = 2000°C = 4090°R

Combustor gas velocity ( $U$ ) = 300 ft/sec

These parameters correspond to one set of typical AFAPL ramjet combustor operating conditions. With respect to heat transfer considerations, the probe under consideration can be considered to consist of three sections (Sections I, II and III) as shown in Fig. A-1. Although heat transfer in each of these sections is characterized by forced convection, the detailed mechanisms are considerably different in the three sections and each must be treated separately.

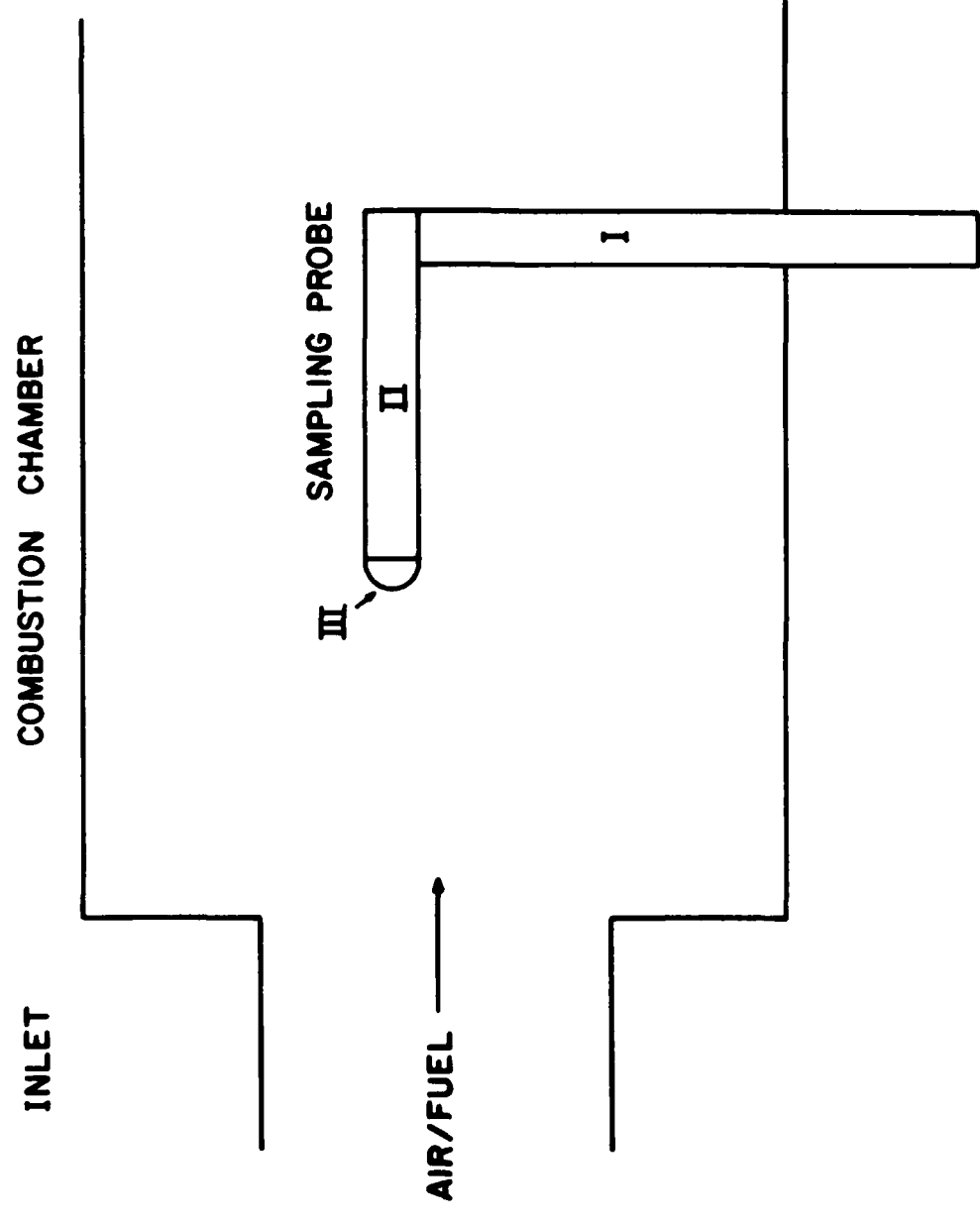


Figure A-1. Schematic representation of the sampling probe for the calculation of the heat transfer rate.

The first section (I) of the probe is positioned perpendicular to the directions of gaseous flow. Heat transfer from the flowing gas as it passes over the cylindric probe (Section I) is controlled by the fact that there exists a point of flow separation on the probe cylinder, beyond which, a pattern of eddies develops, giving rise to a turbulent wake. No analytical solution to this problem exists, but a large quantity of data has been obtained for correlating the mean Nusselt number,  $N_d$ , with the Reynolds number,  $R_d$ . These are related by the expression,

$$N_d = C R_d^n \quad (A-1)$$

where  $C$  and  $n$  are constants, the values of which vary with the Reynolds number.  $R_d$  may be expressed as,

$$R_d = \frac{\rho U d}{\mu} \quad (A-2)$$

in which  $U$  and  $d$  are the gas velocity (300 ft/sec) and the diameter (0.5") of the probe, respectively.  $\rho$  and  $\mu$  are the density and dynamic viscosity, respectively, of the combustion gas to be evaluated, at a mean temperature  $T_m$ , given by

$$T_m = \frac{1}{2} (T_g + T_{p.o.}) \quad (A-3)$$

In the present example,  $T_m$  is found to be 2470°R based on the specified values of  $T_g$  (4090°R) and  $T_{p.o.}$  (850°R).

In order to reduce the complexity of the present analysis it is assumed that the thermodynamic properties of the combustion gas are the same as those of

dry air, the properties of which have been well documented. Obviously, some error will be induced by this assumption since a typical combustion gas consists of many species (CO, CO<sub>2</sub>, H<sub>2</sub>O) in addition to dry air. However, this error is probably only on the order of 10%, which is acceptable for the present purposes.

From standard thermal property tables it is known that,

$$\rho \text{ (air, 50 psi, } 42470^{\circ}\text{R}) = 0.0545 \text{ lb/ft}^3$$

$$\mu \text{ (air, 50 psi, } 2470^{\circ}\text{R}) = 1.14 \times 10^{-4} \text{ lb/ft} \cdot \text{sec}$$

Therefore, the corresponding Reynolds number is,

$$R_d = \frac{\rho U d}{\mu} = \frac{0.0545 \times 300 \times 0.5}{12 \times 1.14 \times 10^{-4}} = 5976$$

For this Reynolds, N<sub>d</sub> is,

$$N_d = 0.174 R_d^{0.618} \quad (A-4)$$

$$= 37.53$$

Consequently, the mean heat transfer coefficient ( $\bar{h}$ ) can be calculated from the expression,

$$\bar{h} = N_d \cdot \frac{k}{d} \quad (A-5)$$

in which k is the thermal conductivity of the combustion gas (again assumed to be dry air) at temperature, T<sub>m</sub>. From this relation, the value of k is found to be,

$$k_{\text{air}}, 50 \text{ psi}, 2470^{\circ}\text{R} = 0.164 \text{ btu/ft} \cdot \text{hr} \cdot {}^{\circ}\text{R}$$

substituting this value into equation (A-5) yields,

$$\bar{h} = 37.53 \times \frac{0.164 \times 12}{0.5} = 147.7 \text{ btu/ft}^2 \cdot \text{hr} \cdot {}^{\circ}\text{R}$$

The only additional information needed for the calculation of the heat transfer rate is the surface area of the probe (Section I),  $A_I$ , which is,

$$A_I = \pi d l = \pi \left(\frac{0.5}{12}\right) \left(\frac{6.0}{12}\right) = 0.065 \text{ ft}^2$$

A maximum length of 6 in. is taken for  $l$ , which is the case when the probe is extended to the opposite side of the combustor wall. Thus the heat transfer rate in Section I is,

$Q_I$  = heat transfer rate (Section I)

$$\begin{aligned} &= \bar{h} \cdot A_I (T_g - T_{\text{p.o}}) \\ &= 147.7 \times 0.065 \times (4090 - 850) \\ &= 31109 \text{ Btu/hr} \\ &= 2178 \text{ cal/sec} \end{aligned} \tag{A-6}$$

Section II of the probe is positioned in line with the flow of the combustion gas. The heat transfer in this case can be treated similarly to that for flow over a plate (which is curved in the present case) for which the standard mean Nusselt number applicable to the present flow conditions is,

$$N_1 = 2 \times 0.332 \text{ } Pr^{1/3} \cdot R_1^{1/2} \tag{A-7}$$

for  $0.6 < \text{Pr} < 10$  and  $R_1 < 3 \times 10^5$ .

$\text{Pr}$  is the Prandtl number, as defined by,

$$\text{Pr} = \frac{\mu \text{Cp}}{k} \quad (\text{A-9})$$

in which  $\text{Cp}$  is the heat capacity of the combustion gas (air).  $R_1$  is the Reynolds number, given by,

$$R_1 = \frac{\rho U L}{\mu} \quad (\text{A-9})$$

in which  $L$  is the length of the probe (4" Section II) along the direction of the gas flow. All terms on the right hand sides of eqs (A-8) and (A-9) are known except  $\text{Cp}$  which can also be obtained from thermal property tables, that is,

$$\text{Cp}_{\text{air}, 50 \text{ psi}, 2470^\circ\text{R}} = 0.286 \text{ Btu/lb} \cdot {}^\circ\text{R}$$

Therefore,

$$\text{Pr} = \frac{1.14 \times 10^{-4} \times 0.286}{0.164/3600} = 0.716$$

and

$$R_1 = \frac{0.0545 \times 300 \times 4}{12 \times 1.14 \times 10^{-4}} = 4.78 \times 10^4$$

It is clear that the  $\text{Pr}$  value obtained is well within the range between 0.6 and 10, and the  $R_1$  value is less than  $3 \times 10^5$ , which indicates that the boundary layer is laminar and the use of equation (A-7) is indeed justified. Consequently, the other parameters needed to determine the heat transfer rate in Section II can be calculated as shown below.

$$\bar{N}_1 = 2 \times 0.332 \times (0.716)^{1/3} \times (4.78 \times 10^4)^{1/2} = 129.9$$

$$\bar{h} = \bar{N}_1 \frac{k}{L} = 129.9 \times \frac{0.164}{4/12} = 63.9 \text{ Btu/ft}^2 \cdot \text{hr} \cdot {}^\circ\text{R}$$

$$A_{II} = \pi d L = \pi \left(\frac{0.5}{12}\right) \left(\frac{4}{12}\right) = 0.0436 \text{ ft}^2$$

The heat transfer rate is then,

$$Q_{II} = \text{heat transfer rate (Section II)}$$

$$= \bar{h} A_{II} (T_g - T_{p.o})$$

$$= 63.9 \times 0.0436 \times (4090 - 850)$$

$$= 9027 \text{ Btu/hr} = 632 \text{ cal/sec}$$

The front portion of the quartz/stainless-steel probe is cone-shaped and directly opposes the combustion gas flow. The heat transfer rate per unit area in this section is expected to be much greater than that in the probe body. The calculation of the heat transfer rate here is further complicated by the fact that the center portion of nose cone consists of a quartz probe with an aperture. The greatest heat transfer must occur on the very tip of the quartz probe, owing to the strong impinging gas flow which prevents the formation of a boundary buffer layer in this region. This, coupled with the fact that the heat conduction coefficient of the quartz probe is several orders of magnitude lower than that of the probe body, causes this region to exhibit the greatest steady state temperature, and the largest temperature gradient. Neither a theoretical model nor experimental data

are available for this situation which would, permit detailed analysis of such a complicated structure environment.

However, if one is only concerned about the overall heat transfer rate in this region, then by assuming a uniform surface temperature, it is possible (at least semi-quantitatively) to obtain an understanding of this region. In addition to this approximation, it is further assumed that the front portion of the probe can be represented as a hemisphere (Section III in the figure) for which the heat transfer phenomenon has been treated previously (as for space re-entry vehicles or on the leading edges of missiles, aircraft, etc.).

For subsonic flow over a hemispherical body, characterized by flow impingement, a semi-empirical equation has been recommended for the calculation of the overall heat transfer rate,

$$N_d = 1.32 R_d^{0.5} Pr^{0.4} \quad (A-10)$$

In the present case both the Reynolds number,  $R_d$ , and Prandtl number,  $Pr$ , have been provided in the previous section, that is, 5976 and 0.716, respectively. Therefore,

$$N_d = 1.32 (5976)^{0.5} (0.716)^{0.4} = 89.28$$

Consequently,

$$\bar{h} = N_d \cdot \frac{k}{d} = 89.28 \times \frac{0.164 \times 12}{0.5}$$

$$= 351.4 \text{ Btu/ft}^2 \cdot \text{hr} \cdot {}^\circ\text{R}$$

$A_{III}$  = surface area of the semi-sphere

$$= 1/2 \pi d^2 = 1/2 \pi \left(\frac{0.5}{12}\right)^2 = 0.0027 \text{ ft}^2$$

And finally, the heat transfer rate in this third section is,

$$Q_{III} = \text{heat transfer rate (Section III)}$$

$$= \bar{h} A_{III} (T_g - T_{p.o.})$$

$$= 351.4 \times 0.0027 \times (4090 - 850)$$

$$= 3074 \text{ Btu/hr}$$

$$= 215 \text{ cal/sec}$$

It is interesting to note that the ratio of the mean heat transfer coefficients ( $\bar{h}$ ) for the three sections is,

$$(\bar{h})_I : (\bar{h})_{II} : (\bar{h})_{III} = 147.7 : 63.9 : 351.4$$

$$= 2.3 : 1 : 5.5 \quad (A-11)$$

This ratio appears to be reasonable, although there is apparently no means of actually testing this. Based on the previous calculation, the total heat transfer rate for the probe is thus,

$$Q_{\text{total}} = Q_I + Q_{II} + Q_{III} \quad (A-12)$$

$$= 2178 + 632 + 215$$

$$= 3025 \text{ cal/sec}$$

Consequently the required cooling water flow rate will be,

$$F_{\text{water}} = \frac{3025 \text{ cal/sec}}{160 \text{ cal/cc}}$$

$$= 18.9 \text{ cc/sec}$$

$$= 1134 \text{ cc/min}$$

The maximum attainable water flow rate for the existing quartz/stainless-steel probe is approximately 200 cc/min, with the water head pressure set at 50 psi, using the existing water pump. A greater flow rate will require raising the water head pressure, which can be increased up to 100-150 psi with the existing water pump. The major limitation on the water flow rate in the present quartz/stainless-steel probe arises from the use of two long spiral tubes (1/10" OD x 0.01" wall) with relatively small flow conductance for the water inlets. It is worth noting that a newly designed probe, in which three concentric tubes are used, will permit much higher flow conductance.

It should be mentioned again that the calculated total heat transfer rate ( $Q_{\text{total}}$ ) derived above is based on the assumption that the probe's exterior wall temperature ( $T_{p.o}$ ) and interior wall temperature ( $T_{p.i}$ ) are 200°C and 100°C, respectively. Further energy balance calculations are still required in order to justify the validity of this assumption, or to suggest a second set of  $T_{p.o}$  and  $T_{p.i}$  for further iteration calculations. As mentioned in the earlier discussion of the second step in the heat transfer process, the quantity of heat transferred ~~through~~ the combustion gas is the same as that transferred to the cooling water through the probe wall, according to the well known heat conduction equation,

$$Q_{\text{total}} = - k A \frac{dT}{dX} \quad (\text{A-14})$$

In this equation the value  $k$  is the heat conduction coefficient, or 8.67 Btu/ft.hr.°R for stainless steel, within the temperature range between 100°C and 200°C.  $A$  is the total surface area of the probe (0.109 ft<sup>2</sup>, the sum of A section I and A section II).  $dT/dX$  is the temperature gradient across the wall of the probe. Integration of eq. (A-14) yields

$$Q_{\text{total}} \int_0^s dx = -k A \int_{T_{p,o}}^{T_{p,i}} dT$$

or

$$Q_{\text{total}} = \frac{kA}{s} (T_{p,o} - T_{p,i}) \quad (A-15)$$

The thickness (s) of the wall of the present quartz/stainless-steel probe is 0.065". Therefore, the right hand side of eq. (A-15) is found to be

$$\begin{aligned} & \frac{kA}{s} (T_{p,o} - T_{p,i}) \\ &= \frac{8.67 \times 0.109 \times 12 \times (850 - 670)}{0.065} \\ &= 31404 \text{ Btu/hr} \\ &= 2198 \text{ cal/sec} < Q_{\text{total}} \end{aligned}$$

Apparently, the originally defined value for  $T_{p,o}$  (200°C) is slightly lower than the actual value which is believed to be within the range 230°C to 240°C. However, further iterations are not necessary in view of this small temperature difference.

## APPENDIX B

### CHARACTERIZATION OF THE FLOWFIELD IN THE PROBE SAMPLING SYSTEM

In utilizing a probe-mass spectrometer gas monitoring system for the measurement of gas species concentration in a combustor flow field, a major concern is the design of the sampling probe. Proper design of this system is important from both practical and theoretical standpoints. Many potential problems associated with the design of this system such as the probe's physical strength, chemical inertness, cooling, and resistance to the soot formation, as well as various other factors including aerodynamic, thermal, and chemical considerations, must all be solved. However, the solution to many of these problems can be achieved only through in-depth analysis of the performance of the probe system. The first such analysis to be accomplished is a characterization of the flow field of the sampled gas within the probe. Detailed profiles of the velocity, temperature, pressure, and density of the sampled gas within the entire probe sampling system are obtained, subject to several necessary approximations.

Shown in Fig. B-1 is a schematic illustration of the proposed quartz/stainless-steel sampling probe which is placed in a combustor flow field comparable to that typically found in a ramjet combustor. Due to the size of the sampling probe, the gas flow field in the vicinity of the probe tip will be disturbed. For simplicity, it is assumed that the unperturbed gas flow at some distance away from the sampling probe (region I) is maintained at a

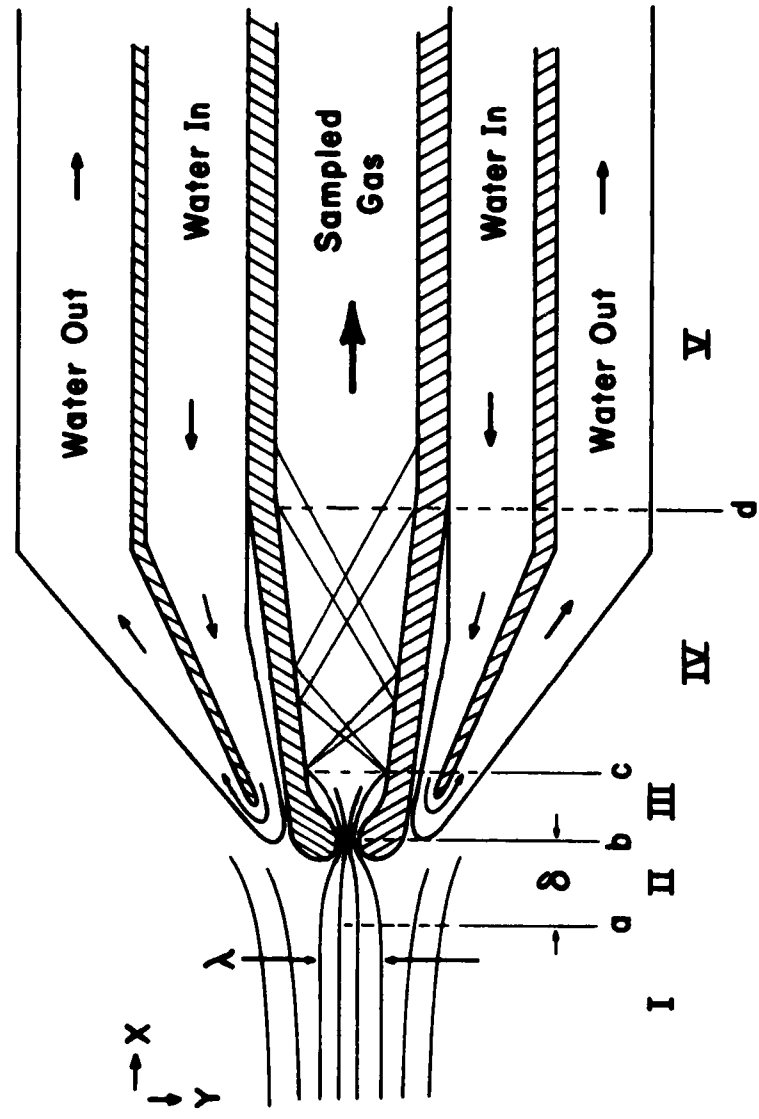


Figure 3-1. Schematic illustration of the gas flowfield within the present probe sampling system.

direction parallel to the axis of the sampling probe. As indicated in the figure, the disturbance of the flow field will begin at line "a" which is at a distance,  $\delta$ , (between lines "a" and "b", region II) away from the probe inlet (line "b"). Due to the strong suction exerted by the sampling probe, it is seen that all incoming gas that passes through a disc having a diameter,  $\lambda$ , at the line "a", will be deflected toward the center line. The velocity of the gas will be rapidly increased as it approaches the probe inlet, and concurrently the gas density, pressure and temperature will decrease. Eventually, all of this gas will pass through the sampling probe aperture at line "b".

As will be confirmed in later discussion, the gas velocity at the throat of the sampling probe (with an assumed diameter of 0.015" at line "b") will reach sonic velocity in an isentropic process. Beyond line "b" (region III), as a result of the sudden expansion process, the velocity of the gas will be further increased, and thus attain supersonic speed. However, as the gas reaches line "c", this supersonic velocity can no longer be sustained. Beyond this line (region IV), a series of shock waves are initiated, during which, a substantial portion of the gas kinetic energy is lost in collisions with the wall of the probe. Following these shock waves, the gas velocity again returns to subsonic. Within this region (region V, between line "d" and the mass spectrometer pump inlet), the velocity of the sampled gas will be slowly increased due to the pumping while gas temperature will be decreased until the temperature is equilibrated with that of the probe wall, as controlled by the cooling water, and/or equilibrated with that of the transfer line as controlled by the heating tape.

Obviously, it is practically impossible to provide a detailed description of the flowfield in the present probe sampling system without some simplifications. In the following analysis several simplifications and assumptions are employed in order to facilitate the analysis. However, it is felt that these assumptions do not result in significant errors and a true physical picture of the sampling process is still essentially obtained.

In the present probe sampling, it is assumed that the sampling probe having an aperture of diameter,  $D$ , (0.015") is placed in a combustion gas flowfield (region I) defined as follows:

$$P_I = 50 \text{ psi (static pressure)}$$

$$T_I = 2000^\circ\text{C (gas temperature)}$$

$$V_I \text{ (or } V_a) = 300 \text{ ft/sec (linear gas velocity along } x \text{ axis)}$$

$$\rho_I = 0.529 \times 10^{-3} \text{ g/cm}^3 \text{ (gas density)}$$

The above values correspond to those typical of the combustion environment in a ramjet combustor. For simplicity, it is also assumed that the combustion gas is an ideal gas, for which the thermodynamic properties are similar to those of air.

The information initially desired in the present analysis is the gas sampling rate through the sampling probe which is characteristic of the combustion environment described above. For an ideal nozzle with downstream pressure lower than approximately one half of the upstream pressure, the gas sampling

rate,  $Q$  in g/sec, through the nozzle, is given by the well-known relation,

$$Q = \gamma^{1/2} A_b P_I \left(\frac{M}{RT_I}\right)^{1/2} \left(\frac{2}{\gamma + 1}\right)^{\frac{\gamma + 1}{2(\gamma - 1)}} \quad (B-1)$$

in which  $\gamma$  is the ratio of the specific heat of the gas at constant pressure to that at constant volume (1.4 for air);  $A_b$  is the area of the aperture of the sampling probe ( $1.14 \times 10^{-3} \text{cm}^2$ );  $M$  and  $R$  are respectively, the molecular weight and gas constant of the combustion gas. The above equation is derived on the basis of the assumption that the flow is isentropic and has sonic speed at the nozzle's throat. Both of these assumptions will be verified in later discussion.

In an earlier experiment, the gas sampling rate through a quartz microprobe with nominal aperture diameter of 0.008" was measured, and compared with that calculated from eq. (B-1). Excellent agreement between the two values was observed, which indicates that the fabricated quartz microprobe can be considered as an ideal nozzle. This conclusion is also applicable to the present quartz/stainless-steel probe since the probe tip is identical in geometry to the previously tested probe, and was fabricated using the same procedures.

It should be noted that in calculating the gas sampling rate using equation (B-1), it is also assumed that the gas environment outside of the sampling probe is static. This equation is not strictly applicable in the present case since the gas stream outside the sampling probe is not actually static, and in fact, has a linear velocity of 300 ft/sec. However, this velocity is only approximately one-tenth of sonic speed, and will not significantly affect the flow field in the probe-tip area, which has a velocity in

the sonic regime. Therefore no significant error is expected from this approximation. A more exact calculation of the gas sampling rate, taking into account the initial gas velocity, will also be described.

Upon inserting into equation (B-1) the values of all parameters applicable for the present case, the calculated gas sampling rate,  $Q$ , is found to be 0.0333 g/sec. From the continuity equation,

$$Q = \rho_I A_I V_I \quad (B-2)$$

the area,  $A_I$ , of the sampling disk is then determined to be  $6.89 \times 10^{-3} \text{ cm}^2$ , which corresponds to a sampling disk diameter ( $\lambda$ ) of 0.037 inch.

The next task in the present analysis is to locate the position designated by line "a" (or the distance  $\delta$ ) in Figure B-1. This is very difficult, since a detailed knowledge of the flowfield distribution within region II is required. A simplified treatment suitable for this purpose was documented by Rosen, ("Potential Flow of a Fluid into a Sampling Probe", Johns Hopkins Univ. Appl. Phys. Lab. Report CF-2248, Silver Spring, Md 1954), in which the probe was approximated by a disc sink of radius,  $r$ , and the incoming flow was assumed to be an incompressible flow. A plot of  $z/r$  as a function of sampling rate ratio  $x$  was provided by Rosen, where,

$z$  = distance from the disc sink at which a distortion ( $V_y/V_x$ ) of 5% was found

$V_x$  = unperturbed gas velocity along x-axis.

$V_y$  = resultant gas velocity along y-axis due to the field disturbance.

$$x = \frac{0}{\rho(\pi r^2) V_x} \quad (B-3)$$

Using the same approximations as suggested by Rosen, the sampling rate ratio  $x$  calculated for the present case is 6.0, which corresponds to a  $z/r$  value of 4.4, using Rosen's plot. Consequently, the value of  $z$  is 0.033 inch, which can be considered to be the distance  $\delta$  in Fig. B-1.

The above calculations reveal some quantitative information with respect to the aerodynamic disturbance to the flowfield in the vicinity of the probe, resulting from the presence of the sampling probe. This disturbance, however, does not appear to be very significant and is acceptable for the present application. Of course, as seen in the figure, additional disturbance of the flow is also observed outside the sampling column. This disturbance may affect the overall combustion but will not affect the validity of the sampling data because it is not "seen" by the sampling probe.

On the basis of the calculated results discussed above, it can be concluded that the sampling probe is capable of detecting an average concentration of gas which issues from a disc having a diameter of 0.037 inch at a distance of 0.033 inch away from the sampling probe, which has an aperture with a diameter of 0.015 inch. However, this does not imply that the sampled gas concentration actually corresponds to the average

concentration of the gas in the disc located exactly 0.033 inch away from the probe. This is due to the fact that further chemical reactions may still occur in the gas after it passes through the disc and before it actually enters the sampling probe.

In order to provide a more definitive answer to the question of probe sampling resolution, the following two extreme cases can be considered. In the first case, it is assumed that after the gas passes through the disc located at line "a", all further chemical reactions are quenched owing to the rapid drop of the gas temperature and the concurrent decreases in gas density. In such a case, the concentration of the sampled gas will correspond to the average concentration of the gas within the disc at a distance exactly  $\delta$  (0.033 inch) away from the probe. However, the above assumption is valid only in certain cases. As will be discussed later, both the gas temperature and gas density even at the probe aperture (line b) can still be sufficient to cause further chemical reactions.

In the second extreme case, it is assumed that after passing through the disc, the gas still undergoes chemical reactions, and that these occur at exactly the same rates as those which characterized the reactions in the absence of the sampling probe. In this case, it is first necessary to calculate the transit time ( $\Delta t$ ) for the gas to move from the disc to the probe inlet. After obtaining  $\Delta t$ , the distance ( $\beta$ ) that the gas would travel from the disc within this time, if the probe were not present, can be obtained. In this case, the

concentration of sampled gas will correspond to the average concentration of the gas within a disc (of same size as that previously described) at a distance exactly ( $\delta - \beta$ ) away from the probe inlet. Again, this assumption is not realistic since some reduction of the reaction rates (either rates of formation or rates of disappearance) will always occur with the decreasing gas temperature and density.

For the calculation of  $\Delta t$ , it is assumed that the gas velocity,  $V_x$ , increases linearly from the line "a" (with  $V_a$  or  $V_I = 300$  ft/sec) to the line "b" (with  $V_{II} = 10 V_I$ , the exact value of which will be given later). The value of  $\Delta t$  is therefore given by,

$$\begin{aligned}\Delta t &= \int_0^\delta \frac{dx}{V_x} = 0.256 \frac{\delta}{V_I} \\ &= 0.256 \times \frac{0.033}{12 \times 300} = 2.35 \times 10^{-6} \text{ sec}\end{aligned}\quad (B-4)$$

Consequently,

$$\beta = V_I \cdot \Delta t = 0.256 \delta = 0.0084" \quad (B-5)$$

$$\delta - \beta = 0.033" - 0.0084" = 0.0246" \quad (B-6)$$

As noted, neither one of the extreme cases discussed above represents the true situation, which is intermediate between these. Therefore, it is accurate to state that the sampling probe herein described (with aperture diameter,  $D$ , of 0.015 inch) actually detects the average concentration of gas within a cylindrical volume having a diameter of 0.037 inch (or  $2D$ ), and a length in the direction of probe axis of 0.0084 inch (or  $1/2 D$ ), and with the center of the cylinder located at a distance 0.029 inch ( $\delta - 1/2 \beta$ , or  $2 D$ ) in front of the probe inlet. This statement clearly expresses the relationship between the sampling resolution and the probe aperture size, although the relationship is

not necessarily true in all cases since it is dependent on the sampling environment.

It is important to note that the gas within the cylindrical volume is sampled as if the sampling probe were not present. This is true because the aerodynamic effect resulting from the probe's presence has been taken into account explicitly, subject to the approximations applicable here.

It should also be noted that the above statement regarding the sampling resolution holds only for the pre-sampling stage, that is, the stage just before the gas enters the probe inlet. Any complications, such as reactions with the wall, which occur in the post-sampling stage, may still cause errors in the gas concentration deduced. In a later discussion (Appendix C), the problem of sampling resolution will be discussed further, using after-burning of CO as an example.

As discussed previously, upon passing through the sampling nozzle throat (line "b") the velocity of the sampled gas attains sonic speeds. The exact thermal properties, such as temperature, pressure, and density, as well as the velocity of the gas at this point, can be calculated assuming that the process is isentropic. The following energy balance equation can be used to correlate the properties of the sampled gas at line "a" and line "b".

$$\frac{1}{2} V_a^2 + C_p T_a = \frac{1}{2} V_b^2 + C_p T_b \quad (B-7)$$

For an ideal gas,

$$C_p = \frac{\gamma}{\gamma-1} - \frac{R}{M} \quad (B-8)$$

in which,  $\gamma = 1.4$  for air. Therefore

$$\frac{1}{2} V_a^2 + \frac{\gamma}{\gamma-1} - \frac{R}{M} T_a = \frac{1}{2} V_b^2 + \frac{\gamma}{\gamma-1} - \frac{R}{M} T_b \quad (B-9)$$

Since it is also assumed that the gas velocity,  $V_b$ , is sonic, the value of  $V_b$  can be calculated for a given temperature  $T_b$  from the relation,

$$V_b^2 = \gamma - \frac{R}{M} T_b \quad (B-10)$$

After substituting the expression in equation (B-10), as well as the known values of  $T_a$  (2000°C or 2273°K) and  $V_a$  (300 ft/sec or  $9.14 \times 10^3$  cm/sec) into equation (B-9), the value of  $T_b$  can be readily determined, and is found to be,

$$T_b = 1891^\circ K$$

From equation (B-10) then,

$$V_b = 8.72 \times 10^4 \text{ cm/sec}$$

For an isentropic process,

$$\rho_b = \rho_a \left( \frac{T_b}{T_a} \right)^{1/\gamma-1} = 0.529 \times 10^{-3} \left( \frac{1891}{2273} \right)^{\frac{1}{1.4-1}} = 0.334 \times 10^{-3} \text{ g/cm}^3$$

and,

$$p_b = p_a \left( \frac{T_b}{T_a} \right)^{\frac{\gamma}{\gamma-1}} = 50 \times \left( \frac{1891}{2273} \right)^{\frac{1.4}{1.4-1}} = 26.3 \text{ psi}$$

The total gas sampling rate can also be calculated as follows.

$$\rho_b V_b A_b = (0.334 \times 10^{-3}) \times (8.72 \times 10^4) \times (1.14 \times 10^{-3}) = 0.0332 \text{ g/sec}$$

It should be noted that the gas sampling rate (0.0332 g/sec) calculated from the above equation is exact in the sense that the initial gas velocity ( $V_a$ ) has been taken into account explicitly. The result obtained is also essentially the same as the value (0.0333 g/sec) derived earlier from equation (B-1). This further confirms the previously employed assumption that the initial gas velocity,  $V_b$ , which is small in comparison with the sonic speed, can be ignored in calculating the gas sampling rate through a nozzle.

Due to the geometry of a nozzle, once the sampled gas passes through the aperture (at line "b") it experiences a rapid aerodynamic expansion with a rapid increase (supersonic) in velocity, and with a concurrent decrease in temperature. Eventually, a point is reached (line "c") beyond which no further increase of velocity can be sustained and a series of non-isentropic shock waves are initiated. There is no simple means of specifying the exact location of line "c", since this is, to a large extent, dependent on the nozzle geometry. However, an upper limit can be set by assuming that at a maximum distance (line "c,max.") the temperature of the gas drops to absolute zero. Therefore, according to the energy relation,

$$\frac{1}{2} V_a^2 + C_p T_a = \frac{1}{2} V_c^2, \text{max.} \quad (\text{B-11})$$

For an ideal gas, the value of  $V_{c,\max}$  determined from this expression is,

$$V_{c,\max} = 2.14 \times 10^5 \text{ cm/sec}$$

This velocity is approximately twice the gas velocity at the nozzle aperture, and represents the ultimate gas velocity that can be achieved in such an aerodynamic expansion process. Of course, the actual onset of shock waves would have occurred somewhere before this point.

For the sake of simplicity it can be assumed that line "c" is located at one aperture diameter distance away from line "b", with  $A_c = 2 A_b$ . It can be found from the plot of  $P/P_a$  as a function of  $A_b/A$  based on the isentropic assumptions, (Liepmann, p. 126) that

$$P_c = 0.1 P_a = 5 \text{ psi.}$$

Therefore, according to the isentropic relationships,

$$\rho_c = \rho_a \left( \frac{P_c}{P_a} \right)^{1/\gamma} = 0.529 \times 10^{-3} \left( \frac{1}{10} \right)^{1/1.4} = 0.102 \times 10^{-3} \text{ g/cm}^3 \quad (B-12)$$

and,

$$T_c = T_a \left( \frac{P_c}{P_a} \right)^{\frac{\gamma-1}{\gamma}} = 2273 \left( \frac{1}{10} \right)^{\frac{1.4-1}{1.4}} = 1177 \text{ }^{\circ}\text{K} \quad (B-13)$$

From the equation of continuity,

$$V_c = \frac{\rho_b V_b A_b}{\rho_c A_c} = \frac{0.0332}{0.102 \times 10^{-3} \times 2 \times (1.14 \times 10^{-3})} \quad (B-14)$$

$$= 1.43 \times 10^5 \text{ cm/sec}$$

This value of  $V_c$  is intermediate between  $V_b$  and  $V_{c,\max}$  and is, perhaps, not an unreasonable choice.

In summary, the detailed profiles of the density ( $\rho$ ), temperature (T) and velocity (V) of the sampled gas within regions II and III of the present sampling probe system are presented in Fig. B-2. These profiles were obtained by assuming an isentropic process, as discussed in the previous section.

It is seen from Fig. B-2 that, in the nozzle sampling process described here, the temperature of the sampled gas drops from an initial value of 2000°C or 2273°K at line "a" to a value of 1177°K at line "c", solely due to the aerodynamic cooling. This cooling effect can be more readily appreciated if it is expressed as a cooling rate in units such as degrees/sec or cals./sec/g. in order to facilitate direct comparison with other types of cooling, such as conductive cooling and convective cooling which normally occur in a probe which is water cooled. To determine this aerodynamic cooling rate, the total transit time for the sampled gas in moving from line "a" to line "c" needs to be estimated. In a previous calculation (equation (B-4)), the gas transit time from line "a" to line "b" was estimated to be  $2.35 \times 10^{-6}$  sec. The transit time ( $\Delta t'$ ) from line "b" to line "c" can also be estimated by assuming that the gas velocity,  $V_x$ , within this region increases linearly from  $V_b$  ( $8.72 \times 10^4$  cm/sec) at line "b" to  $V_c$  ( $1.43 \times 10^5$  cm/sec) at line "c". Therefore,

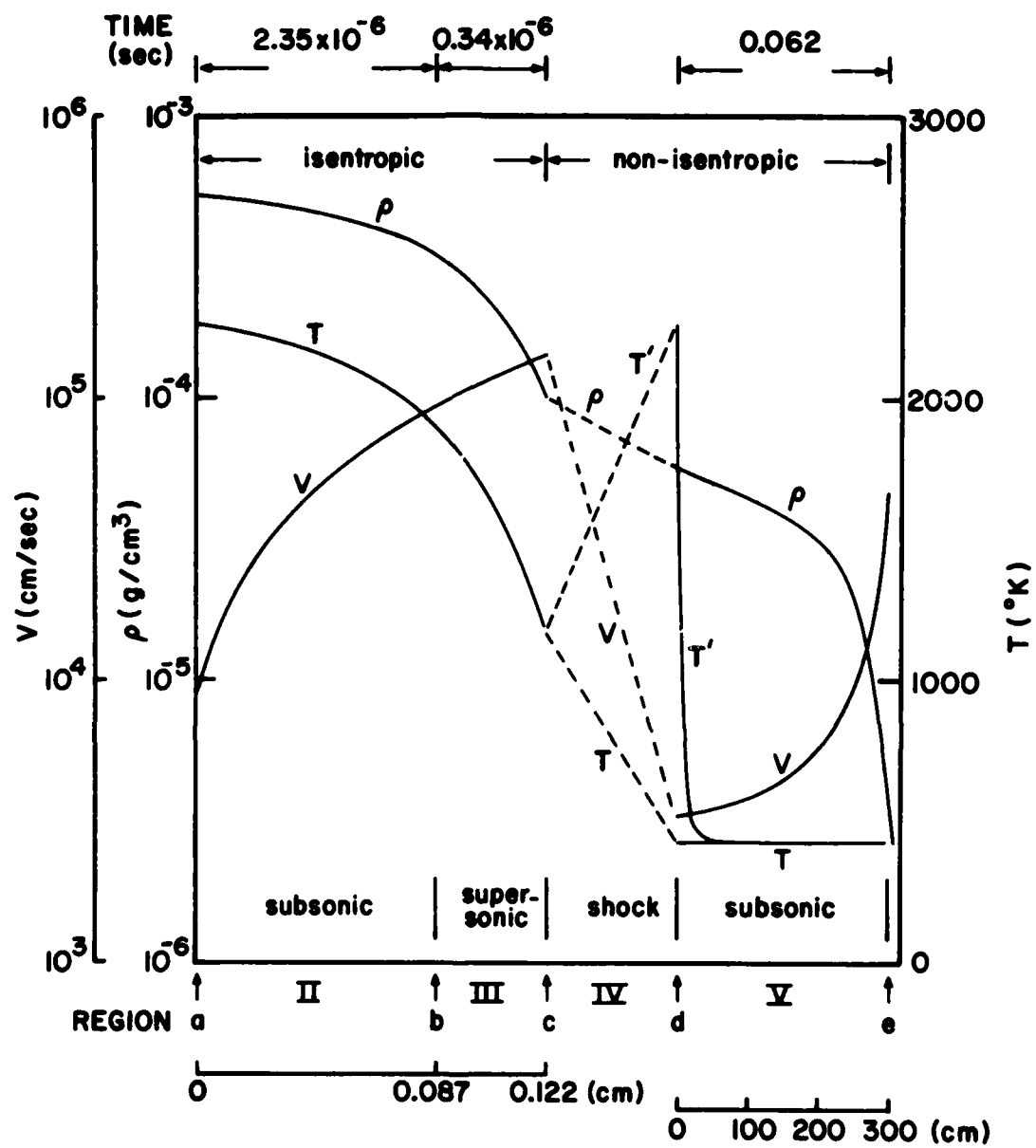


Figure B-2. Profiles of the velocity, temperature and number density of the sampled gas within the present probe sampling system.

$$\Delta t' = \int_0^{0.015''} \frac{dx}{V_x} = 0.34 \times 10^{-6} \text{ sec} \quad (B-15)$$

Consequently, the total gas transit time from line "a" to line "c" is  $2.69 \times 10^{-6}$  sec (that is,  $\Delta t + \Delta t'$ ). The rate of cooling of the sampled gas due to the aerodynamic cooling process can then be readily calculated as follows.

$$\text{Rate of cooling (in } ^\circ\text{K/sec)} = \frac{\Delta T}{\Delta t + \Delta t'} = \frac{2273 - 1177}{2.69 \times 10^{-6}} = 4.07 \times 10^8 \text{ } ^\circ\text{K/sec} \quad (B-16)$$

or,

Rate of cooling (in cal/sec. g)

$$\begin{aligned} &= C_p \cdot \frac{\Delta T}{\Delta t + \Delta t'} = \frac{\gamma}{\gamma - 1} \cdot \frac{R}{M} \cdot \frac{\Delta T}{\Delta t + \Delta t'} \quad (B-17) \\ &= \left( \frac{1.4}{1.4-1} \cdot \frac{1.99}{29} \right) \text{ cal/} ^\circ\text{K.g} (4.07 \times 10^8 \text{ } ^\circ\text{K/sec}) \\ &= 9.8 \times 10^7 \text{ cal/g.sec} \end{aligned}$$

In a conventional isokinetic probe, which depends on convective water cooling to quench the gas sample, the quenching rate attainable is typically on the order of  $10^6$   $^\circ\text{K/sec}$ . This is at least two orders of magnitude smaller than the cooling rate derived from the above calculation. The advantage in using an aerodynamic sampling probe is thus clearly demonstrated. The above calculation also clearly indicates that during the presently utilized sampling process, little heat is transferred from the sampled gas to the probe environment, in comparison with that attainable with the aerodynamic cooling process. The conditions within probe regions II and III are virtually adiabatic, which justifies the use of isentropic equations in the characterization of the flow-field within these regions.

Region IV, which is bounded by line "c" and line "d", is perhaps the most poorly understood region in the present flowfield characterization attempts. Within this region, a series of oblique shock waves are expected to develop, during which a sharp rise in the gas temperature and pressure will occur, along with a sharp decrease in the gas velocity. This is a non-isentropic process. At the termination of this shock front (line "d"), the gas velocity will be reduced to subsonic, while the gas pressure will be readjusted to a value sustained by the existing pumping system. The final gas temperature at line "d" will depend essentially on the quantity of heat which can be dissipated to the probe wall. Although the velocity and pressure of the sampled gas at line "d" is calculated (see later section) using a given gas sampling rate and system pumping speed, this calculation is at best an approximation, due to the lack of knowledge with respect to the heat dissipation rate within this region.

Certainly, the gas temperature beyond the shock front will not be 2000°C, (the temperature of the incoming gas outside of the probe) because the shock process is no longer isentropic. Since the shock waves are closely confined by the probe wall, it is conceivable that a large portion of the kinetic energy of the gas particles will be lost to the wall, after a series of collisions, in the form of a "slip flow", and possibly only a small portion of this energy will be recovered, and result in increasing the temperature of the gas.

Due to the lack of detailed knowledge of the shock process mentioned above, the temperature profile of the sampled gas within region IV is illustrated in

Fig. B-2 as represented by two lines, each corresponding to an extreme condition. The dashed line "T" is based on the assumption that at the termination of the shock process the sampled gas has transferred essentially all of its kinetic energy to the probe wall, and the gas temperature has dropped to 150°, the same as that of the probe wall. On the other hand, the  $T'$  dashed line is based on the assumption that during the shock process, none of the gas energy has been lost to the probe wall (that is, an isentropic process) and that the temperature of the gas will eventually rise to 2000°C (the same as that of the incoming gas prior to sampling) at the termination of the shock process. Of course, neither approximation represents the true situation which is intermediate between these two extremes. The profiles of the gas density ( $\rho$ ) and velocity ( $V$ ) within region IV are also represented by dashed lines, as seen in Fig. B-2, owing to the lack of detailed knowledge.

As described previously, once the sampled gas leaves region IV and enters region V, its velocity will be reduced to subsonic. The temperature of the gas will also be gradually decreased, due principally to the water cooling, but also to a lesser extent due to the expansion of the gas as it moves further downstream toward the pumping system. The detailed characterization of the flowfield, including the velocity and pressure distribution in this region, is also difficult to estimate, due to the lack of information with respect to the heat transfer rate between the gas and its environment. Some approximations will still be required as will be discussed in the following section.

In the present mass spectrometric sampling system, the sampling probe is interfaced with the mass spectrometer through a transfer line (1/4 inch O.D. and 3/16 inch I.D.) which is approximately 10 ft in length. The entire line is maintained at a temperature of 150°C in order to prevent condensation of moisture within the line. Figure B-3 shows a schematic illustration of the sampling system, which includes the sampling probe, the transfer line, the mass spectrometer and a differential pumping system which serves to prevent over-loading of the mass spectrometer by the sampled gas. The flowfield within this region is largely dictated by the transfer line configuration and the pumping system for a given sampling rate.

Since the majority of the sampled gas is pumped away through the first pump shown in the figure, only this pump need be considered, as far as the gas flow within region V is concerned. In the following calculation, it is further assumed that the gas within region V has the same thermal properties as those of air. With respect to the gas temperature, two different assumptions can be made: 1) Assume that the gas temperature has already reached 150°C at point "d". Therefore its temperature will be in equilibrium with that of the probe within the entire region. 2) Assume that the temperature of the gas at point "d" is 2000°C. Therefore, the temperature of the gas will gradually decrease as the gas moves further downstream. Calculations of the flowfield within region V on the basis of these two assumptions will be different. In the following discussion, the calculation based on the first assumption is considered first, since this calculation is less complex and a more exact solution can be obtained.

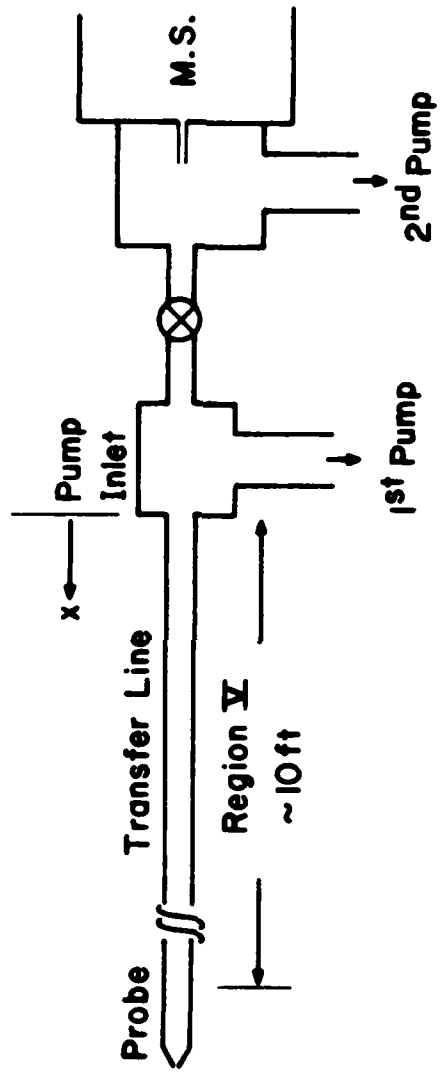


Figure B-3. Schematic illustration of the interface between the probe and the mass spectrometer monitoring system.

The flow of the gas within region V is basically viscous, and is governed by the well-known Poiseuille's law, which can be stated by the relation,

$$Q'_x = \frac{\pi D^4}{256 \eta x} (P_x^2 - P_p^2) \quad (B-18)$$

where  $Q'_x$  is the gas thorough-put at a distance,  $x$ , from the pump inlet;  $D$  is the inside diameter of the transfer line (3/16 inch or 0.48 cm);  $\eta$  is the viscosity of the gas (air) at 150°C ( $250 \times 10^{-6}$  poise); and  $P_x$  and  $P_p$  are the gas pressures at point  $x$ , and at the pump inlet, respectively.

The gas thorough-put,  $Q'_x$ , is expressed in units of (pressure) (volume)/(sec) and is related to the gas sampling rate  $Q$  (0.0333 g/sec) by the expression,

$$Q'_x = Q \frac{RT}{M} \quad (B-19)$$

where  $R$  is the gas constant;  $M$  is the molecular weight;  $T$  is the gas temperature (150°C). Since the values of  $Q$  and  $T$  are assumed to be constant everywhere within region V, it follows that  $Q'_x$  must also be constant everywhere. Combination of the above two equations yields,

$$Q = \frac{\pi D^4}{256 \eta x} \frac{M}{RT} (P_x^2 - P_p^2) \quad (B-20)$$

This equation explicitly expresses the term,  $(P_x^2 - P_p^2)$ , as a function of the distance,  $x$ , from the pump inlet. After substituting known values for all terms (except  $x$ ,  $P_x$ , and  $P_p$ ) into the above equation, this expression reduces to,

$$(P_x^2 - P_p^2) = 1.5 \times 10^{-5}x \quad (B-21)$$

in which  $P_x$  and  $P_p$  are in units of atm., and  $x$  is in units of cm.

The value of the pump inlet pressure,  $P_p$ , can also be calculated from the equation,

$$Q \frac{RT}{M} = \text{thorough-put at pump inlet}$$
$$= S P_p = 39.8 \text{ atm-cm}^3/\text{sec} \quad (B-22)$$

in which  $S$  is the pumping speed at the pump inlet, which can be assumed to be the same as the pumping speed of the first pump (this is rated at 500 liters/min or  $8333 \text{ cm}^3/\text{sec}$ ). Therefore the value of  $P_p$  is calculated to be

$$4.78 \times 10^{-3} \text{ atm or } 3.63 \text{ torr (1 atm = 700 torr).}$$

Substituting the known value of  $P_p$  into equation (B-21) yields,

$$P_x = 1.5 \times 10^{-5} x + 2.28 \times 10^{-5} \quad (B-23)$$

in which  $P_x$  is in atm and  $x$  is in cm.

The density ( $\rho_x$ ) of the sampled gas at any point in region  $V$  can also be readily calculated from the relation,

$$\rho_x = \frac{M}{RT} P_x \quad (B-24)$$

The distribution of the gas velocity,  $V_x$ , can also be calculated from the continuity equation,

$$Q = \rho_x A V_x = 0.0333 \text{ g/sec} \quad (B-25)$$

The profiles of the density ( $\rho$ ) and velocity ( $V$ ) of the sampled gas in this region are also shown in Fig. B-2. It is seen here that the gas velocity remains essentially subsonic within the transfer line, except at the entrance to the pump inlet, where the gas velocity again becomes supersonic ( $>3.3 \times 10^4$  cm/sec). However, in reality a supersonic flow may never be achieved since the transfer line is not frictionless and some retardation of the gas velocity always occurs, especially in the low pressure region near the pump inlet entrance.

It will be recalled that the gas sampling rate of the present probe was calculated based on equation (B-1), assuming an isentropic process, with sonic speed attained at the probe orifice. The validity of the isentropic process assumption was confirmed in the previous section. However, the assumption of sonic speed at the probe orifice has not been verified explicitly until now. It is known from aerodynamics that a sonic speed is reached at the nozzle's throat (line "b") in an isentropic process only when the nozzle's exit pressure can be maintained below a critical value,  $P_r$ , which can be expressed mathematically by the equation,

$$P_r = \frac{\gamma}{\gamma + 1}^{\gamma/(\gamma-1)} P_I = 0.54 P_I \text{ (for air)} \quad (B-26)$$

In the present case  $P_I$  is 50 psia, while the nozzle's exit pressure is given as  $P_d$ , which can be calculated from equation (B-23), and is found to be 0.0673 atm (or 1.0 psia). Clearly this value is substantially lower than  $P_r$  (which is  $0.54 \times 50$  psia), and the assumption of sonic flow at the probe's aperture is justified.

With the known gas velocity distribution the total time (t) required for the gas to be transferred from the front end of region V to the pump inlet can be calculated as follows:

$$t = - \int_{305}^0 \frac{1}{V_x} dx = 0.062 \text{ sec} \quad (B-27)$$

This time can be viewed as an approximation of the total gas transit time from the point where the gas enters the sampling probe to the point at which the sampled gas reaches the mass spectrometer ion source. This is true because the velocity of the sampled gas at both the front end (regions I to IV) and the rear end of the transfer line is supersonic, sonic, or near-sonic, and its transit time is negligible in comparison with the time the gas spends within the transfer line (0.062 sec).

It should be emphasized that the gas transit time derived from the above calculation is largely based on the two assumptions:

1. The tip of the sampling probe is an ideal nozzle, with the gas achieving sonic speed at the nozzle throat.
2. The gas flow within the transfer line is viscous and follows Poiseuilles law.

The gas transit time for a given transfer line configuration is thus highly dependent on the nozzle aperture area and the sampling environment pressure. In a previous calculation, applicable for a sampling probe having a nominal aperture diameter of 0.008 inch which was inserted into a flame of 0.1 atm

pressure, gas velocity within the transfer line was shown to be approximately one order of magnitude lower than that found in the present case, and the calculated transit time was as long as 0.4 sec. This result is somewhat surprising since one would intuitively expect that in the flame sampling, the gas would move at a faster speed due to the lower pressure within the transfer line. However, in fact, with the larger aperture and a higher sampling environment pressure, the sampled gas apparently achieves a faster initial velocity within the transfer line, which consequently results in a shorter transit time for a given transfer line configuration.

It is interesting to compare the presently calculated transit time with an actually measured value obtained in an earlier test. In this test, a static sampling probe was inserted into the combustor (POA = 22.5 psi), at a point 2.88 inches downstream from the inlet section. Argon was injected into the air stream (POF=89 psi) through an injection port and controlled by a manually operated relay switch. The outer end of the probe was connected to the mass spectrometer via a 10 ft transfer line (1/4 inch O.D.). The Ar<sup>+</sup> ion intensity was continuously monitored, and this signal was transmitted to the Y-axis of an X-Y recorder. The X-axis of the recorder was driven by a time-based saw-tooth sweep signal.

Initially, the Ar gas solenoid valve was kept in the closed position, during which time, the recorder trace remained at the baseline level. Immediately after the valve was opened, admitting Ar, a mark was made on the recorder trace, indicating the initiation of Ar injection. After this onset,

the  $\text{Ar}^+$  ion signal still remained at the baseline level for approximately 0.2 second. After this 0.2 second delay, the  $\text{Ar}^+$  signal increased abruptly until a constant level signal was obtained. This signal should be representative of the new gas composition in the flowfield. The 0.2 second delay is the total system response time, including time required for the solenoid valve activation, argon injection, probe sampling, gas transfer within the transfer line, mass spectrometric detection and the signal recording. This response time is not highly accurate, however, since the experimental measurement was rather crude.

However, the measured time delay of 0.2 second should approximately correspond to the gas transit time from the probe entry to the mass spectrometer ion source. This value is approximately 3 times larger than the calculated value (0.062 sec) which was derived by assuming sonic sampling with a nozzle sampling probe and viscous flow within the transfer line. It should be noted that the static sampling probe employed in this test is certainly not an ideal nozzle. Furthermore, the chamber pressure was 22 psi which is only one-half of that (50 psi) assumed in the calculation. These differences will lead to a smaller sampling rate, slower gas velocity, and longer gas transit time, and so there is no real discrepancy in the calculated and measured data.

It is to be noted that the derived profiles of gas density,  $\rho$ , and velocity,  $V$ , within the transfer line (in region V), as shown in Fig. B-2, are based on the assumption that the gas temperature,  $T$ , is maintained constant

(150°C) within the entire region. As discussed previously, this represents only an extreme case, whereas in the real case, some rise of the gas temperature must have occurred due to the shock process (in region IV). It is of interest to determine to what extent this temperature increase will affect the gas flowfield within region V. More importantly, it is desirable to know how rapidly the sampled gas will be cooled down again if the gas temperature has indeed been sharply increased from the shock process. This is of vital importance in understanding the capability of the present sampling probe system to quench the sampled gas.

In the following calculation, it is assumed that the gas temperature is initially at 2000°C at point "d" (in Fig. B-1). The cooling of this gas is mainly due to the contact (convective cooling) with the probe wall, which is assumed to be continuously maintained at 150°C (by water-cooling) since the gas will further expand as it moves downstream, some degree of cooling is also achieved due to this aerodynamic expansion. However, as seen in Fig. B-2, the gas velocity at the initial portion of region V is quite low, and so the cooling of the gas due to this expansion effect is insignificant in comparison with the convective cooling.

With the temperature of the sampled gas at point "d" assumed to be 2000°C, the Reynolds number for the flow at this point is given by the expression,

$$R_d = \frac{\rho V D}{\mu n} = \frac{4}{\pi D} \frac{\rho V A}{\mu n} = \frac{Q}{\pi D n} \quad (B-28)$$

where the term,  $n$ , is the viscosity of the gas (air) at 2000°C ( $7.0 \times 10^{-4}$  poise). This relation yields,

$$R_d = 126 \ll 2300$$

and thus, the flow at this point is laminar. As a matter of fact, the entire flow within region V is laminar, since the value,  $Q$ , is constant everywhere, and the value of  $n$  ranges from  $7.0 \times 10^{-4}$  poise at 2000°C to  $2.3 \times 10^{-4}$  poise at 150°C.

For incompressible laminar flow through a tube of diameter,  $D$ , and constant wall temperature,  $T_s$ , the Nusselt number ( $N_d = \frac{hD}{k}$ ) is known to be 3.658. This value expresses explicitly the relationship between the convective heat transfer coefficient,  $h$ , between the wall and the fluid, and the thermal conductivity,  $k$ , of the fluid. Although this value is only applicable for an incompressible laminar flow, it is applicable in the present case because, as discussed previously, the cooling of the sampled gas due to aerodynamic expansion is negligible. Therefore,

$$h = 3.658 \frac{k}{D} \quad (B-29)$$

For a small section of the tube with length,  $dx$ , the energy balance within this section can be expressed as follows,

$$h (T - T_s) (\pi D) dx = -Q C_p dT \quad (B-30)$$

Substituting equation (B-29) into equation (B-30), yields

$$-Q C_p dT = 3.658 \pi k (T - T_s) dX \quad (B-31)$$

Since it is assumed that the sampled gas is an ideal gas, the heat capacity  $C_p$  can be readily calculated from the expression,

$$C_p = \frac{\gamma}{\gamma - 1} \frac{R}{M} = 0.239 \text{ cal/g.}^{\circ}\text{K} \quad (B-32)$$

The thermal conductivity,  $k$ , is known to be a function of the gas temperature but is independent of the gas pressure if an ideal gas is assumed. Based on tabulated data (Handbook of Chem. and Physics, 51th Ed. p.E-2), the value of  $k$  for air can be expressed as a function of temperature,  $T$ , in the following approximate form.

$$k = 0.18T + 8.1 \quad (B-33)$$

Here  $k$  is expressed in units of  $10^{-6}$  cal/cm.sec. $^{\circ}$ K and  $T$  is in  $^{\circ}$ K. Results obtained using the above equation can also be compared with more extensively tabulated data (Nat'l. Bur. Stand. (U.S.) Circ. 564, 1955) which gives the value of  $k$  at temperatures up to 2500 $^{\circ}$ K. The agreement is generally good except at temperatures above 1000 $^{\circ}$ C, where the relationship becomes somewhat non-linear. However, the error is not very large and the use of eq (B-33) is probably acceptable for present purposes.

Substituting equation (B-33) and all known values of  $C_p$ ,  $Q$  and  $T_s$  into eq. (B-31) yields,

$$-7.89 \times 10^{-3} dT = 3.658 \pi (T-423) (0.18T + 8.1) \times 10^{-6} dX \quad (B-34)$$

Integration of equation (B-34) with a given initial value of  $T$  ( $2000^{\circ}\text{C}$ ) at  $x = 0$  (point d) yields,

$$\frac{T - 423}{T + 45} = \exp (-6.78 \times 10^{-2} x - 0.226) \quad (\text{B-35})$$

The temperature profile of the sampled gas within region V, based on this equation, is shown in Fig. B-2 ( $T'$  curve). It is seen that the greatest temperature drop occurs within the first 5 cm from the starting point (d). The significance of this rate of temperature decrease in terms of reaction quenching will be further discussed in Appendix C.

It should be emphasized that as discussed previously, the actual temperature at point d must lie somewhere between the extreme values of  $2000^{\circ}\text{C}$  and  $150^{\circ}\text{C}$ . Consequently, the actual temperature profile within region V must also lie somewhere between the  $T$  and  $T'$  lines shown in Fig. B-2. It is also worth noting that the temperature profile within region V can also be mathematically derived by using a procedure similar to that indicated by equation (B-30) if a known initial temperature at point d can be specified.

The continuous variation of the gas temperature naturally will also affect the density,  $\rho$ , and velocity,  $V$ , profiles of the sampled gas within this region. For simplicity, equation (B-20) can be simplified and rewritten in the following form.

$$\begin{aligned}
 Q &= \frac{\pi D^4}{256nX} \frac{M}{RT} P_2 \\
 &= \frac{\pi D^4}{256nX} \frac{RT}{M} \rho^2
 \end{aligned} \tag{B-36}$$

This equation is no longer valid strictly since it is derived by assuming a constant gas viscosity,  $n$ , and temperature,  $T$ . Fortunately it has been found experimentally that the increase of the gas viscosity,  $n$ , approximately parallels that of the gas temperature,  $T$ . The net effects of the changes of these two parameters along the transfer line (region V) on the gas density,  $\rho$ , largely cancel out, as seen in equation (B-36). This means that the gas density,  $\rho$ , is relatively insensitive to the temperature change along the transfer line, and the density profile (Fig. B-2) derived in the previous calculation by assuming a constant gas temperature is still applicable for the present case. Consequently, the previously obtained velocity profile (Fig. B-2) is also applicable, based on the continuity equation.

In conclusion, through the present flowfield characterization effort, the detailed profiles of the velocity, temperature, pressure and density of the sampled gas within the entire probe sampling system have been obtained. The result of this effort provides an in-depth understanding of the performance of the present probe sampling system and serves as a basis for a discussion of the validity of the probe sampling techniques, which will be presented in the next section.

## APPENDIX C

### DISCUSSION OF THE VALIDITY OF GAS SPECIES CONCENTRATION MEASUREMENTS USING THE PRESENT PROBE SAMPLING SYSTEM

Historically, the use of probes for monitoring gas species concentrations in combustion environments has been the subject of many concerns regarding the validity of the measurements and the extent to which these might be disturbed by the mere presence of the probe in the flowfield. Due to the size of the probe, the aerodynamic flow of the combustion flowfield is disturbed by the wake of the probe, and by the withdrawal of the gas sample. This aerodynamic disturbance would be expected to alter the original concentration gradients, and thus the composition of the gas entering the probe. A probe may also constitute a heat sink which can disturb the temperature distribution around the probe area, and thus change the species concentration profiles in this area.

Once the gas enters the probe aperture, further chemical reactions may still proceed to some degree if insufficient quenching capability is provided by the probe. Of course, considerations relative to quenching should not be limited solely to the probe tip region. The entire gas transfer line starting at the probe tip and ending at the detector must be considered.

Potential problems associated with the use of a sampling probe are certainly not limited only to the above-described aspects. Other possible complications, including mass discrimination, surface reactions, and soot

formation can all affect the validity of species concentration measurements made using probes.

In the foregoing section, a novel water-cooled stainless-steel probe with a quartz nozzle probe tip was described. This probe is designed for sampling of gaseous species in high-temperature and high-pressure combustion environments, such as that which characterizes a ramjet combustion flowfield. Many considerations were taken into account in the design of the probe such that all adverse effects that may affect the validity of the concentration measurement can be eliminated or at least minimized. In this section, general discussions of several of these potential problem areas are presented. Emphasis is placed on the understanding of the significance of these problems with respect to applications of the proposed probe sampling system for gas sampling in a high-temperature and high-pressure combustion environment.

In addition to general discussions, some more detailed analyses are also made on a quantitative basis. The sampling of CO in an afterburning region using the present probe sampling system will serve as an example. In these analyses, the effects of aerodynamic disturbance, temperature gradients, and probe quenching are taken into account. The concept of equivalent reaction length is employed in these analyses, from which a quantitative description of the sampling resolution of the probe can be derived. From these analyses, a clearer understanding of the capability, as well as the limitations of the present probe system can be obtained. Furthermore, these analyses also suggest means of improving the present sampling system.

### Aerodynamic Disturbance

In conventional isokinetic sampling, the sample velocity at the probe inlet is nearly matched to the flow velocity of the medium sampled, so that aerodynamic disturbance of the flowfield owing to the presence of the probe is largely eliminated. However, in spite of the latter advantage, the isokinetic probe is not generally favored for combustion sampling because it provides insufficient quenching, and is subject to uncertain thermal effects.

On the other hand, in an aerodynamic sampling probe, problems with respect to quenching and thermal effects are largely eliminated. Unfortunately, a significant aerodynamic disturbance of the combustion flowfield is caused by the presence of such a probe. As seen in Fig. B-1, a major disturbance of the flowfield will extend to some distance upstream from the probe (line "a"). This disturbance, coupled with the cooling of the gas which occurs in this region (II), ensure that the gas concentration detected does not correspond to the actual concentration of the gas at the probe orifice.

If it can be assumed that once the gas passes through line "a" (where the flowfield disturbance onsets) all reactions of the gas will be frozen due to the rapid aerodynamic cooling, then it is correct to say that the detected gas concentration corresponds to the average concentration of the gas located at line "a" within a disk of diameter somewhat larger than that of the probe's aperture. However, in reality, complete quenching is never achieved in such a probe. The net result is that the sampling region cannot be precisely defined, and the spatial uncertainty is approximately equal to the size of the aerodynamic disturbance region (that is, region II, see Fig. B-1). A more

detail discussion of the spatial resolution of the probe is provided in the latter section.

Still another problem relative to the aerodynamic disturbance is the fact that this disturbance may also cause some sampling bias which favors either heavier or lighter components of the gas. No further discussion of this effect is given here since the problem of mass discrimination in general will be further discussed in a later section.

#### Thermal Effects

A major concern in the use of a sampling probe, especially a water cooled probe, is that the probe represents a heat sink which can disturb the temperature distribution around the probe area. This perturbation produces changes in chemical reaction rates, which results in changes in species concentration profiles.

One experiment conducted by Seery (1976) involved insertion of an uncooled quartz probe into a low-pressure, methane-air premixed flame (2030°K). The results of this experiment showed that the temperature of the gas along the axis of the probe at a distance of 0.7 mm upstream from the probe was decreased by approximately 60°C. This decrease was gradually diminished to zero at a distance of 4.5 mm from the probe.

This measured thermal effect, while undoubtfully significant in the low pressure flame system, needs to be closely examined in relation to the present sampling system. In this examination, the following two points are clarified: 1) differentiation of the thermal effects in the presampling region and the sampling region. 2) fundamental analysis of each cause of thermal effects and the significance of each with respect to the present sampling environment, which differs markedly from a low pressure flame.

As seen in Fig. B-1, the presence of the sampling probe in the combustion flowfield exerts a strong aerodynamic disturbance which extends to line "a". This disturbance causes a sharp change of the gas velocity within region II downstream from line "a". Along with this velocity change, there is also a sharp change in the gas temperature distribution within this region (see Fig. B-2), which is purely aerodynamic in nature. Actually, this sharp temperature change is desirable, since the probe is intended to sample the gas within this region. It is desirable that once the gas has entered this region a sharp temperature drop of the gas can take place such that no further change of the gas composition will occur thereafter.

In order to ensure the validity of the gas composition measurements made with the sampling probe, it is vitally important that the composition of the gas immediately before it enters the sampling zone (region II) be unaltered due to the presence of the sampling probe. Referring to Fig. B-1, this means that both the flowfield and temperature distributions of the gas in region I should not be disturbed by the probe. As discussed previously, the aerodynamic disturbance of the gas flowfield within this region is minimum and can be ignored. However perturbation of the temperature distribution in this region may still occur to some degree, and this is the subject of the present discussion.

Cooling of the gas in a presampling region (such as region I in Fig. B-1) in the presence of a heat sink (probe) can occur as a result of thermal conduction, convention, and radiation. Considering first conduction cooling, it is known that the heat flux per unit area ( $Q_x$ ) transferred from the presampling region to the heat sink (probe) is expressed by,

$$Q_x = -k \frac{(T_g - T_p)}{\Delta X} \quad (C-1)$$

Here  $T_g$  is the temperature of the gas in the presampling region;  $T_p$  is the temperature of the probe tip; and  $\Delta X$  is the distance between the presampling region and the probe. The thermal  $k$  is the thermal conductivity of the gas and is known to be independent of the gas pressure for an ideal gas. Therefore the heat flux per unit area remains virtually constant for a given temperature gradient, regardless of the gas pressure. This flux may be quite significant in a low pressure flame (typically 0.1 atm) and can cause a substantial temperature drop in the presampling zone. However, this same heat flux loss from a presampling zone in a high pressure combustion system, such as the combustion flowfield of interest here, with 50 psia pressure, will cause hardly any temperature drop due to its much higher pressure and mass flow rate per unit area.

It is also clear from eq. (C-1) that the gas temperature drop in the presampling region due to thermal conduction is proportional to the temperature difference ( $T_g - T_p$ ). In the present quartz/stainless-steel probe design, owing to the lower heat conductivity of the quartz material, the temperature of

the quartz probe ( $T_p$ ) is maintained at a value much higher than that of a conventional water-cooled metal probe. As a result, the probe tip is not as important as a heat sink and a lower temperature drop in the presampling region therefore occurs.

Another point worth mentioning is that thermal conduction is a form of heat transfer characterized by the random exchange of gas particles between two adjacent regions of different temperature. In a continuous flow system, however, the rate of this random exchange is reduced substantially if the bulk velocity of the gas medium is significant in comparison with the random velocity of the gas (which ranges from  $5 \times 10^4$  cm/sec at 25°C to  $1.4 \times 10^5$  cm/sec at 2000°C for air). In the present probe sampling system, which employs aerodynamic sampling, the bulk gas velocity does indeed become quite large in region II (see Fig. B-2). As a result, the effective thermal conductivity for this gas medium is actually much smaller than the thermal conductivity,  $k$ , which is characteristic of a static gas or the thermal conductivity which is applicable for a gas medium with much lower bulk velocity, such as is seen in an isokinetic sampling probe. This is an additional advantage of an aerodynamic sampling probe, that is, it likely induces much less perturbation of the temperature distribution in the presampling region due to a reduction of the effective thermal conductivity.

Cooling of the presampling region due to convection is not a problem in the present case since in a stream lined flowfield such as that shown in Fig. B-1 it is assumed that once the bulk flow of the gas leaves the presampling region (region I), it will no longer return to region I. However, for gas sampling in a recirculation region, the assumption of a well defined stream lined flowfield

is no longer valid and a portion of sampled gas may have been brought into contact with the probe wall before entering the sampling orifice. If the probe wall is maintained at a very low temperature, as is typically the case in a conventional water-cooled metal probe, some premature cooling of this portion of the sampled gas must have occurred, which will undoubtedly affect the validity of the sampling data. On the other hand, in the present sampling system the temperature of the quartz probe can be maintained at a much higher value (typically 1500°K-2000°K). The problem of premature cooling of the gas in the presampling region due to convection can thus be largely minimized, although not entirely eliminated because of practical difficulties.

Radiation loss in the presence of a heat sink (such as a probe) is also believed to be a major mechanism for the cooling of the gas in the presampling region, especially in a low-pressure flame. In the latter environment, the steady state temperature of the gas at a given point (in the absence of the probe) results in part from the fact that the energy loss through radiation emitted by the gas at the given point is balanced by the absorption of thermal radiation emitted by gas in the vicinity of the point. However, when a sampling probe is placed in the vicinity of the point in question, this balance must be disturbed to some degree because of the difference in the emission-absorption characteristics of the sampling probe and the gas it displaces. Consequently, a new balance is established which results in a net change in the temperature of the gas in the presampling region.

The thermal radiation is known to be proportional to the fourth power of

the gas temperature. Therefore, the higher the flame temperature, the greater is the temperature change of the gas in the presampling region. The radiation flux is also inversely proportional to the square of the distance from the source of radiation. This means that the disturbance of the gas temperature distribution will be largest in the region immediately surrounding the probe.

In the absence of experimental data, it can be argued, solely on the basis of theoretical considerations, that the cooling of the gas in the presampling region due to radiation is probably not a significant factor for the present probe sampling system. As discussed in the previous section, the present probe utilizes aerodynamic sampling. In such a probe, detected concentration of gas should correspond to the gas concentration in the vicinity of line "a" (Fig. B-1) rather than that in the immediate vicinity of the probe. Therefore one is only concerned with radiation cooling of the gas in region I, rather than that in region II. Since region I is located at some distance (0.033 inch or 1 mm., in the present case) away from the probe, the effect of the probe, through radiation to the gas in this region, is probably not very critical.

Another consideration is that the present probe is mainly intended to be applied to the sampling of gas species in a combustion system (such as a ramjet combustor flowfield) the pressure or number density of which is typically two orders of magnitude higher than that of a low pressure flame. It is known from a basic law of radiation (Beer's Law) that the attenuation of radiation through a gas medium is proportional to the gas number density ( $\rho$ ) or the pressure of the gas medium, that is,

$$\frac{dI}{dx} = -\sigma \rho I \quad (C-2)$$

in which  $I$  is the flux of the radiation at position  $x$ , and  $\sigma$  is the total interaction cross section between the radiation and the gas medium. Clearly, the penetrating power of the radiation (or the sphere of radiation influence) in a high pressure environment such as the present combustion system is also approximately two orders of magnitude smaller than that in a low pressure flame. As discussed previously, the disturbance of the gas temperature profile due to the presence of a quartz probe inserted in a low pressure flame is known to extend to a region about 5 mm from the probe. This means that the same disturbance, if due to radiation effects, could extend no more than 0.05 mm from the probe with the sampling system described. This length is much less than the distance between region I and the present sampling probe, and is also considerably smaller than the achievable resolution of this probe, which is dictated primarily by aerodynamic sampling considerations.

In conclusion, thermal effects, arising from use of a sampling probe (which can be considered to be a heat sink), are largely negligible with the present probe sampling system. Because of the unique nature of aerodynamic sampling, only the thermal effect on the gas in the presampling region at some distance away from the probe needs to be considered. The position of the buffer layer (region II) greatly reduces the heat transfer between the presampling region (region I) and the probe through either thermal conduction or radiation. Furthermore, in a ramjet combustor, which is characterized by a high mass flow and a large gas number density, the heat transfer due to thermal conduction

and radiation can hardly cause any significant change of the gas temperature in the presampling region. The only significant disturbance of the gas temperature in the presampling region of such an environment which is expected in the presence of a probe is that due to convection cooling (in a recirculation region). Even in this situation, the cooling rate can be reduced by maintaining a higher probe tip temperature by using quartz materials.

### Quenching

One of the most important advantages in using a probe with an ideal nozzle tip for combustion species sampling is the capability of such a probe to rapidly quench reactions of the sampled gas due to aerodynamic cooling of the gas at the nozzle tip. For the probe used in the present study, the attainable aerodynamic cooling rate at the nozzle tip is estimated to be  $4 \times 10^8$  °K/sec, which is at least two orders of magnitude larger than that of a conventional probe which employs convective water cooling to quench the gas sample. All reactions of the sampled gas are essentially quenched due to this rapid cooling.

An interesting question arises as to whether the chemical reactions of the sampled gas, which are frozen in the probe's tip region due to the effective aerodynamic cooling, will be reinitiated in the shock wave region (IV) due to the probable sharp rise of the gas temperature, or in the post-shock region (V), within which convective cooling must provide quenching of the sampled gas. This question cannot be readily answered because it is not clear to what degree the temperature of the sampled gas will rise in such a shock process. However,

it is certain that some degree of quenching must occur within the shock region. As stated previously, the final gas temperature cannot reach 2000°C, the temperature of the gas prior to sampling. Consequently, any chemical reactions which occur in this region must proceed at a lower rate than those which occurred in the gas prior to sampling.

In the following discussion, an in-depth analysis is provided using the case of CO afterburning as an example. In this analysis, the problem of quenching the reaction of CO (from further oxidation to CO<sub>2</sub>), in the sampled gas is considered for the entire probe sampling region, beginning at the point of entrance of CO into the sampling probe, and terminating at the point of entry of the CO sample into the mass spectrometer or other detection apparatus. This analysis is possible because of the knowledge derived from characterization of the flowfield in the sampling probe as described in the previous section (Appendix B).

Prior to this analysis, a brief review of fundamental chemical kinetics is appropriate, in the course which several physical parameters that affect the chemical reaction rates will be identified. Obviously, the first parameter to be considered is the temperature of the reacting species. It is well known from fundamental chemical kinetics considerations that the effect of temperature on the rate constant for simple first-and second-order reactions is described by the Arrhenius equation,

$$k = A \exp (-E/RT) \quad (C-3)$$

where  $E$  is the activation energy, and  $A$  is the frequency factor, which is only weakly dependent on the temperature and can be treated as a constant in most cases. Therefore, for any reaction having an appreciable activation energy, the reaction rate constant must increase with increasing gas temperature.

For second-order or higher order reactions, however, there is another physical parameter that can also affect the reaction rate. In these types of reactions, the formation of reaction products results from collisions between two or more reactant species. If the collision frequency is reduced due to the reduction of the gas density the rate of these chemical reactions will also be reduced.

A major objective in the present probe sampling experiments is to derive detailed information on the combustion efficiency in the ramjet combustor flowfield. An indication of the degree of combustion at any given point within the combustor flowfield can be obtained by direct measurement of the concentration of CO at the sampling point. In order to ensure the accuracy of this measurement, it is important that the sampling probe be properly designed so that no further reaction of CO can occur, once the gas enters the sampling probe.

In a study of CO after-burning it was found by Femmore and Jones (J. Phys. Chem., 61, 651, 1957) that the disappearance of CO can be defined, without specifying the detailed reaction mechanisms, by the following equation,

$$\frac{dN_{CO}}{dt} = -k N_{CO} N_{O_2} \quad (C-4)$$

Here,  $N_{CO}$  and  $N_{O_2}$  are the concentrations of CO and  $O_2$ , respectively, in the after-burning zone, and  $k$  is the overall CO disappearance rate constant, which can be expressed (based on empirical measurements) by the following equation,

$$k = 1.2 \times 10^{12} \exp \frac{-24000}{RT} \text{ cm}^3 \text{ mole}^{-1} \text{ sec}^{-1} \quad (C-5)$$

The above two equations were found to generally satisfactory for most hydrocarbon ( $C_2H_4$ ,  $C_2H_2$ ,  $CH_4$ ,  $C_3H_8$ ) - air flame systems studied. If these two equations are also applicable for the present combustion system, then the disappearance rate of CO due to chemical reactions at any point within the sampling probe in the transfer line can be directly related to the CO disappearance rate at the presampling region (line a in Fig. B-1) as a result of chemical reactions, by the expression,

$$\frac{\left(\frac{dN_{CO}}{dt}\right)}{\left(\frac{dN_{CO}}{dt}\right)_a} = \frac{N_{CO} N_{O_2} \exp \left(-\frac{24000}{RT}\right)}{(N_{CO})_a (N_{O_2})_a \exp \left(-\frac{24000}{RT_a}\right)} = \frac{\rho^2}{\rho_a^2} \frac{\exp \left(-\frac{24000}{RT}\right)}{\exp \left(-\frac{24000}{RT_a}\right)} \quad (C-6)$$

The above equation explicitly describes the quenching of CO at any point within the present probe sampling system.

Since the detailed profiles of the gas density,  $\rho$ , and temperature,  $T$ , along the entire sampling line have been either calculated or estimated, as shown in Fig. B-2, the quenching ratio  $\frac{dN_{CO}}{dt} / \left(\frac{dN_{CO}}{dt}\right)_a$  can be readily calculated. A plot of this ratio as a function of the position within the sampling line is shown

in Fig. C-1. Furthermore, the profiles of the ratios,  $\rho^2/\rho_a^2$ , and,  $\exp(-\frac{24000}{RT})/\exp(-\frac{24000}{RT_a})$ , representing the effects of density and temperature, respectively, on the rate of quenching are also shown in this figure.

It is seen in this figure that the quenching ratio (line 3) within regions II and III does indeed drop rapidly. This decrease is attributed to decreases in both the gas temperature (line 2) and the gas density (line 1). The effect of the use of aerodynamic sampling to achieve rapid quenching of chemical reactions is again demonstrated.

In view of the inadequate knowledge of the shock region (points c to d), all profiles shown in this shock region are represented by dashed lines. As discussed previously, the final temperature of the gas at point d resulting from the shock process must lie somewhere between 2000°C and 150°C. Consequently two lines (lines 2' and 2) are shown within this region, indicating the range of  $\exp(-\frac{24000}{RT})/\exp(-\frac{24000}{RT_a})$ , using the above two assumed final temperature, respectively. On the other hand, since the gas density,  $\rho$ , at this point is only weakly dependent on the temperature assumed at that point, a single line (line 1) is given for the ratio,  $(\rho/\rho_a)^2$ , within this region. As a result, the quenching ratio,  $\frac{dN_{CO}}{dt}/(\frac{dN_{CO}}{dt})_a$ , within this region can also be represented by two lines, (line 3' and 3), one for each of the possible temperature extremes.

Calculations indicate that profiles 2 and 3 will reach  $7.4 \times 10^{-11}$  and  $8.2 \times 10^{-13}$ , respectively, at point d. Both these numbers are too small to be

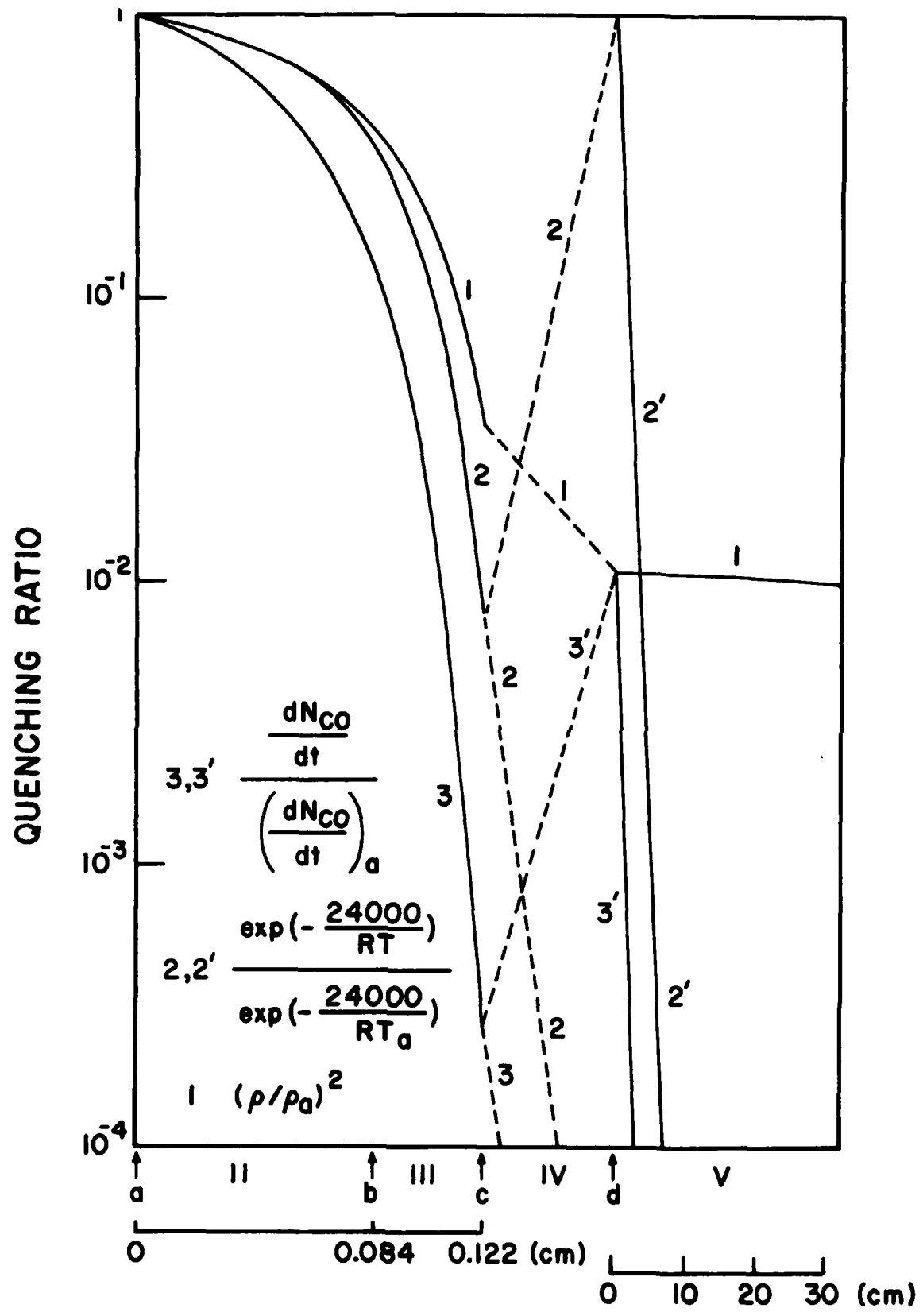


Figure C-1. Plot of quenching ratio as a function of position for CO within the present probe sampling.

shown on the scales in the figure. Beyond this point, profiles 2 and 3 will drop still further, so these are not shown at all in region V.

It is seen in Figure C-1 that within regions II and III, the quenching ratio,  $\frac{dN_{CO}}{dt} / (\frac{dN_{CO}}{dt})_a$ , decreases by almost four orders of magnitude, which is caused by the rapid decreases of both gas temperature and density. This decrease is very rapid considering that the total elapsed time during which this occurs is only  $2.69 \times 10^{-6}$  sec., and the total distance traversed by the gas is only 0.12 cm. The sampled CO gas is essentially frozen within these regions.

As also seen in the figure, profile 3 continues to drop beyond point c within regions IV and V. Any further reaction of CO becomes virtually impossible in these regions. Again, it should be noted that profile 3 within these regions is derived by assuming that all kinetic energy of the gas is lost to the probe environment during the shock process. Of course, this assumption is not realistic, and the true quenching effect is expected to be less drastic, as indicated by this profile.

On the other hand, profile 3' within regions IV and V is observed to first rise to a maximum at point, d, and is then followed by a rapid decrease, largely due to the cooling of the sampled gas by convective water cooling. Again, it will be recalled that this maximum is derived by assuming that the temperature of the sampled gas is restored to 2000°C during the shock process in an adiabatic system. In reality, this is not likely, and the final quenching ratio can never be restored to the maximum indicated by the profile.

### Probe Sampling Resolution

Because of the physical size of a sampling probe, the gas sampled is not representative of the concentration of gas species at a point within the combustion environment, but rather corresponds to the averaged concentration within a certain volume in this environment. Naturally, it is desirable that this volume be a minimum in order to achieve optimum probe sampling resolution. This is especially true in a region such as the initial section of a dump combustor, which is characterized by sharp concentration gradients.

Obviously, the sampling resolution is dependent upon the sampling probe, and more specifically, is a function of the size and the configuration of the probe sampling tip. In an isokinetic sampling probe, since the gas stream is not disturbed by the presence of the probe, it is reasonable to assume that the probe is sampling only a gas stream whose cross sectional area is the same as that of the probe aperture. On the other hand, the resolution of an aerodynamic sampling probe is always poorer by comparison, due to the disturbance of the flowfield. However, in isokinetic sampling, due to the inefficient cooling of the sampled gas, further reactions of the sampled gas may occur after sampling. The finally measured value will therefore no longer correspond to the concentration at the sampling point.

In a previous discussion (Appendix B) of the presently employed quartz/stainless-steel probe, which has an aperture with a diameter of 0.015 inch, the measured gas concentration was found to correspond to the average gas concentration which issues from a disc having a diameter of 0.037 inch at a

distance of 0.033 inch ( $\delta$ ) away from the sampling probe. However, it was also emphasized that the concentration detected does not necessarily correspond to the average concentration of the gas exactly 0.033 inch away from the probe, because further reaction of the gas passing this point always occurs to some degree, regardless of the probe efficiency. In this previous discussion, the sampling resolution was defined by the use of an equivalent reaction length concept. In the present section, this same concept is further explored and applied for consideration of the sampling CO in an afterburning environment. Since the detailed profile of the quenching ratio within the entire probe sampling system has been determined, a more accurate definition of the sampling resolution for the sampling of CO with the present probe sampling system can be obtained.

In the present approach, the total equivalent reaction length,  $\tau$ , is obtained from the following equation,

$$\int_a^e \left( -\frac{dN_{CO}}{dt} \right) \left( \frac{1}{V} \right) dX = \int_0^\tau \left( -\frac{dN_{CO}}{dt} \right)_a \left( \frac{1}{V_a} \right) dX = \left( -\frac{dN_{CO}}{dt} \right)_a \frac{\tau}{V_a} \quad (C-7)$$

The term on the left side of this equation yields the total change of concentration of CO within the entire probe sampling system (from points a to e) as a result of chemical reactions. The right hand side of the above equation represents the length,  $\tau$ , that the gas at point, a, would travel (if the probe were not present) in order to produce the same change of the CO concentration.

It follows that the CO concentration detected with the present sampling system will correspond to the average CO concentration in the gas within a disc of 0.037 inch in diameter, located at a distance, downstream from the point, a, or at a distance ( $\delta-\tau$ ), upstream from the probe (downstream, if ( $\delta-\tau$ ) is negative).

After rearranging, equation (C-7), one obtains,

$$\int_a^e \frac{\left(\frac{dN_{CO}}{dt}\right)}{\left(\frac{dN_{CO}}{dt}\right)_a} \cdot \left(\frac{V_a}{V}\right) \cdot dX = \tau \quad (C-8)$$

$$= \tau_{II} + \tau_{III} + \tau_{IV} + \tau_V$$

in which,

$$\tau_{II} = \int_a^b \frac{\left(\frac{dN_{CO}}{dt}\right)}{\left(\frac{dN_{CO}}{dt}\right)_a} \cdot \left(\frac{V_a}{V}\right) dX \quad (C-9)$$

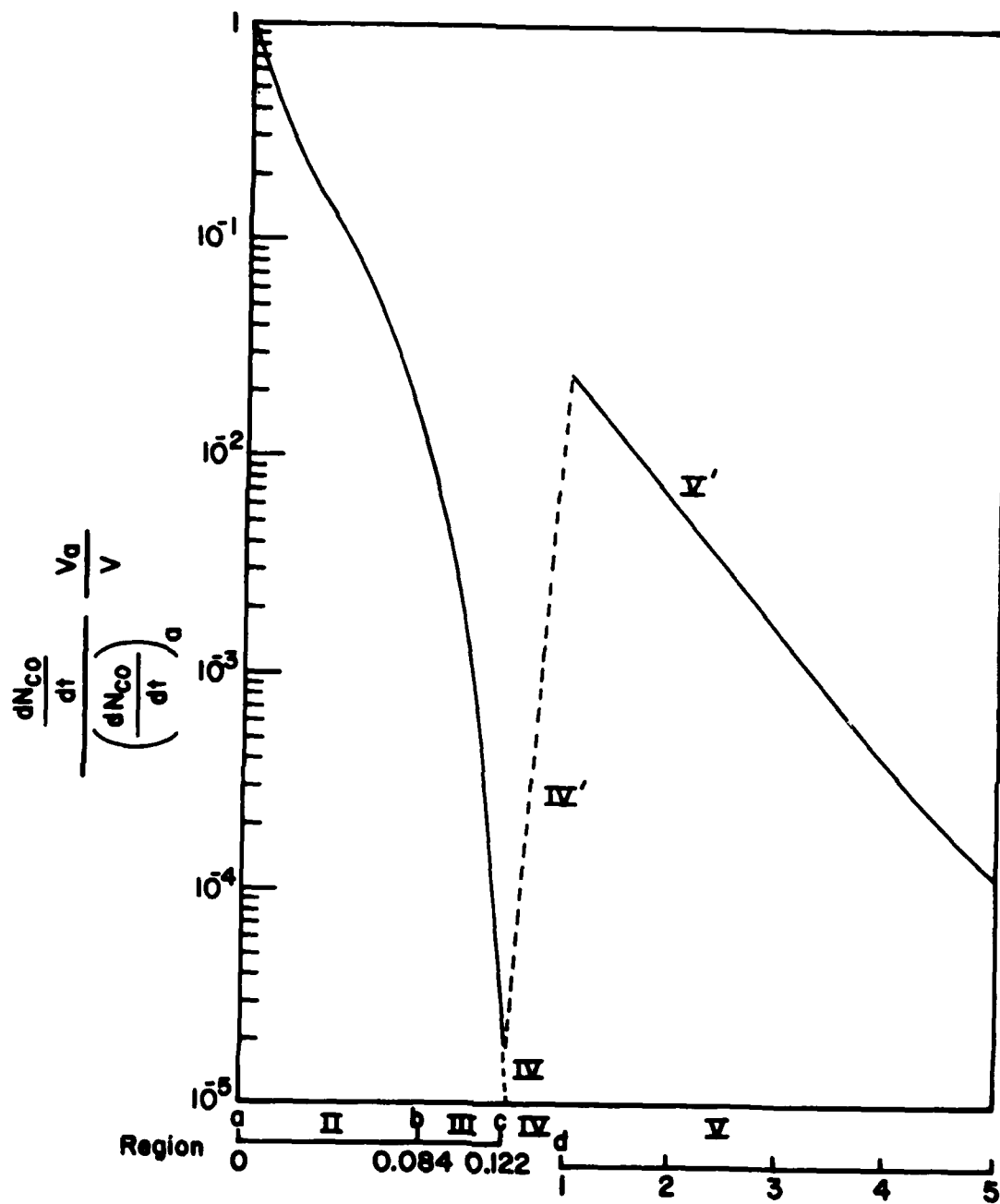
$$\tau_{III} = \int_b^c \frac{\left(\frac{dN_{CO}}{dt}\right)}{\left(\frac{dN_{CO}}{dt}\right)_a} \cdot \left(\frac{V_a}{V}\right) dX \quad (C-10)$$

$$\tau_{IV} = \int_c^d \frac{\left(\frac{dN_{CO}}{dt}\right)}{\left(\frac{dN_{CO}}{dt}\right)_a} \cdot \left(\frac{V_a}{V}\right) dX \quad (C-11)$$

and

$$\tau_V = \int_d^e \frac{\left(\frac{dN_{CO}}{dt}\right)}{\left(\frac{dN_{CO}}{dt}\right)_a} \cdot \left(\frac{V_a}{V}\right) dX \quad (C-12)$$

Figure C-2 shows the profile of  $\frac{\left(\frac{dN_{CO}}{dt}\right)}{\left(\frac{dN_{CO}}{dt}\right)_a} \cdot \left(\frac{V_a}{V}\right)$  as a function of  $x$  for the present probe sampling system. Within regions II and III, the value of  $\frac{\left(\frac{dN_{CO}}{dt}\right)}{\left(\frac{dN_{CO}}{dt}\right)_a} \cdot \left(\frac{V_a}{V}\right)$  drops drastically in a non-linear fashion,



### POSITION (cm)

Figure C-2. Plot of  $(V_a/V) \frac{dN_{CO}}{dt} / \left( \frac{dN_{CO}}{dt} \right)_a$  as a function of position for CO within the present probe sampling system.

with the increase of  $X$ . The deflection in the initial portion of the curve is real, and is due to the finite velocity of the gas outside the probe (region I). The integration of this curve can be accomplished graphically, and yields values of  $\tau_{II}$  and  $\tau_{III}$  as follows,

$$\tau_{II} = 1.8 \times 10^{-2} \text{ cm}$$

$$\tau_{III} = 1.5 \times 10^{-4} \text{ cm}$$

$\tau_{IV}$  has not been calculated owing to the uncertainties in region IV. However, as indicated in earlier discussion, the actual profiles of  $\frac{(\frac{dN_{CO}}{dt})}{(\frac{dN_{CO}}{dt})_a} \cdot (\frac{V_a}{V})$  within this region is believed to be bounded between the profiles IV and IV', shown in Fig. C-2, assuming final temperatures ( $T_d$ ) at point,  $d$ , of 150°C and 2000°C, respectively.

Calculation of  $\tau_V$  is also somewhat uncertain, since it is largely dependent on the gas temperature at point,  $d$ , which is believed to be between 150°C and 2000°C. Also shown in Fig. C-2 is a curve,  $V'$ , which is the profile of  $\frac{(\frac{dN_{CO}}{dt})}{(\frac{dN_{CO}}{dt})_a} \cdot (\frac{V_a}{V})$  within the initial portion (first 4 cm) of region  $V$ , assuming a temperature ( $T_d$ ) at point,  $d$ , of 2000°C. A similar profile,  $V$ , can also be calculated by assuming a temperature ( $T_d$ ) at point,  $d$ , of 150°C, but this is not shown in Fig. C-2, because of its extremely small value. Obviously, the actual value of  $\tau_V$  must lie between two limiting values,  $\lim_{T_d \rightarrow 2000^\circ\text{C}} \tau_V$  and  $\lim_{T_d \rightarrow 150^\circ\text{C}} \tau_V$ , which can be defined as follows,

$$\lim_{Td \rightarrow 2000^\circ\text{C}} \tau_V = \int_d^e V' dx \quad (\text{C-13})$$

$$\lim_{Td \rightarrow 150^\circ\text{C}} \tau_V = \int_d^e V dx \approx 0 \quad (\text{C-14})$$

The profile,  $V'$ , shown in the figure is approximately linear on the semi-log plot. It can be approximated by the following equation at least for the first 4 cm of the region V (beyond 4 cm the profile  $V'$  is too low to be of physical significance).

$$V' = \exp(-1.37x - 3.69) \quad (\text{C-15})$$

Therefore,

$$\begin{aligned} \lim_{Td \rightarrow 2000^\circ\text{C}} \tau_V &= \int_d^e V' dx \\ &\approx \int_0^{300} \exp(-1.37x - 3.69) dx \\ &= 1.8 \times 10^{-2} \text{ cm} \end{aligned} \quad (\text{C-16})$$

and

$$0 < \tau_V < 1.8 \times 10^{-2} \text{ cm} \quad (\text{C-17})$$

In the above calculation, the term,  $\tau_{IV}$ , is excluded due to uncertainties in region IV. However, a crude approximation can be employed to provide an estimated value of  $\tau_{IV}$ . It can be assumed that the profile IV' is linear (as seen in the plot) and spans a distance of 1 cm (that is, from points c to d). An integration of this curve can be readily obtained from the relation,

$$\lim_{T_d \rightarrow 2000^\circ C} \tau_{IV} = \int_c^d IV' dx = 3.4 \times 10^{-3} \quad (C-18)$$

Therefore,

$$\tau_{IV} < 3.4 \times 10^{-3} \text{ cm} \quad (C-19)$$

or,

$$0 < \tau_{IV} + \tau_V < 2.14 \times 10^{-3} \text{ cm} \quad (C-20)$$

In reality, the shock region probably extends for more than 1 cm distance assumed here, but the above equation (equation C-20) will always be valid regardless of the length of region IV. The flow within the shock region can be viewed as a turbulent flow, for which the cooling rate is always faster than that in region V, in which laminar convective cooling is assumed. Furthermore, a longer shock region means a faster gas velocity at point d. The net result is an even smaller  $\tau_{IV} + \tau_V$ .

Finally, by combining equations (C-8) and (C-20), one obtains

$$1.815 \times 10^{-2} \text{ cm} < \tau < 3.955 \times 10^{-2} \text{ cm} \quad (C-21)$$

or,

$$0.007 \text{ inch} < \tau < 0.016 \text{ inch}$$

From previous discussion,  $\delta = 0.033 \text{ inch}$ .

Therefore,

$$0.026 \text{ inch} > \delta - \tau > 0.017 \text{ inch}$$

(C-22)

It can thus be stated that the measured CO concentration using the present probe, having an aperture with diameter of 0.015 inch, will correspond to the average CO concentration in the gas within a cylinder with a diameter of 0.037 inch and thickness of 0.009 inch, and with its center located 0.022 inch in front of the sampling probe.

Obviously, the above statement of the sampling resolution of the present probe is only applicable for the sampling of CO, subject to the various assumptions employed. For the sampling of other combustion species, the thickness of the cylinder samples is likely different due to the difference in the quenching rate. A calculation of the thickness can also be accomplished in a similar fashion, once the kinetics governing the rate of formation or disappearance of the species in question are defined. Without specifying the reaction kinetics, the resolution of the present sampling probe for most gas species can be generalized as corresponding to the averaged concentration within a cube whose length on each side is approximately twice the probe aperture, and with the cube located immediately in front of the probe.

With this understanding of the gas sampling resolution for the present sampling probe, several factors affecting the sampling resolution can be analyzed as indicated below.

1. Probe size. Obviously, there is a direct relationship between the probe size and the sampling resolution. The probe size should be as small as possible consistent with avoiding problems such as probe plugging, soot formation, or inadequacy in the sampling rate for analysis.

2. Probe tip configuration. The probe tip should be drawn to a smooth cone to minimize aerodynamic disturbance of the flowfield. The aperture is preferably in the shape of an ideal nozzle in order to achieve better aerodynamic cooling. Furthermore, for a given aperture size, and downstream transfer line configuration, the ideal nozzle will ensure the largest sampling rate and fastest gas velocity. Consequently, shorter gas transfer time and faster response can be achieved.

3. Transfer line configuration. A transfer line with larger diameter and shorter length will reduce the gas transfer time and the average gas number density within the transfer line, which consequently will ensure a faster response and better quenching.

4. Pumping. Adequate pumping should be provided for the probe sampling system to maintain a low pressure within the transfer line. For a given gas sampling rate, the pressure in the pump also must be kept sufficiently low to ensure the normal operation of the pump. This was implicitly assumed in the above calculation.

5. Probe water cooling. A large water cooling rate is always desirable to achieve rapid cooling of the sampled gas in the post shock region. The

material for the gas tubing in this region should also preferably be a high heat conductivity material. However, the choice of this material is somewhat limited in view of the requirement that the surface be inert to the reactive gas. Selection of stainless steel for this purpose is a reasonable compromise.

#### Mass Discrimination

For the probe described herein, the gas sampling rate,  $Q$ , through the nozzle is given by equation (B-1). It is seen from this equation that the value,  $Q$ , for any gas species is not dependent just on the partial pressure of that species, but is also dependent on the parameters,  $M$  and  $\sigma$ , both of which are characteristic of the gas species and which differ for different gas molecules. Mass discrimination thus inevitably occurs to some degree in sampling a gas mixture with the probe considered here. Mass discrimination is also a factor in gas detection systems such as the mass spectrometer employed here. The pumping system of the mass spectrometer favors pumping of lighter gas components, and this further distorts the gas composition in the mass spectrometer chamber.

Detection of gas molecules in a mass spectrometer is based on the principles of gas ionization and ion detection. It is well known that ionization cross sections are widely different for different types of molecules. Commonly used ion detectors such as electron multipliers are also known to be strongly mass dependent.

In view of these various mass discrimination effects and the variety of different gas components which are expected to be encountered in this study, it is practically impossible to devise a scheme to correct for this mass discrimination on a theoretical basis. In practice, accurate determination of the gas composition requires a well-defined calibration procedure. In this calibration process several gas mixtures of known composition must be prepared and sampled with the sampling system under conditions similar to a real combustion sampling condition. A calibration system of this type, which permits calibration of many common combustion species, has already been constructed and utilized for some gases in other experimental systems. However, calibration for some other species, such as water and free radicals, will likely present some difficulties.

### Surface Reactions

The term "surface reactions" generally refers to any interaction between the sampled gas and the surface of the probe, including surface absorption, catalysis, and so forth. None of these interactions would occur if the probe were not employed. The most complicated surface interaction problem is probably the surface catalysis effect. The significance of this effect is largely dependent on the nature of the species and cannot be generalized. A particularly severe example occurs in the sampling of  $\text{NO}_x$  in a flame. It has been shown that the oxygen atom wall recombination rate is an important factor in determining the extent of  $\text{NO}/\text{NO}_2$  reactions in the probe.

Considerable research has been devoted to the complex subject of the catalytic activity of various probe materials. The general consensus is that quartz, with its relatively low catalytic activity, is a preferred material for the probe. This is one of the prime reasons for the use of quartz in the present sampling probe.

#### Soot Formation

The formation and accumulation of soot on the probe can seriously degrade the sampling efficiency. The aperture of the probe can be virtually plugged if an excessive quantity of soot is allowed to accumulate at the probe's orifice. A compromise commonly employed in an effort to solve this problem involves enlargement of the size of the probe orifice. Actually, this only delays the time required for sufficient accumulation to occur to plug the probe. However, there are problems associated with enlarging the probe orifice, such as loss of sample resolution, increased aerodynamic and thermal effects, and variability in the geometry and size of the orifice, which make such a compromise very undesirable.

Quartz, because of its surface smoothness, higher working temperature, and above all, its remarkably low surface affinity, is a much better probe material with respect to the problem of soot accumulation than is metal. This was experimentally verified by tests in which a quartz probe and a stainless steel probe were compared by inserting both into a Bunsen burner flame which was deliberately adjusted for only partial burning of the fuel, in order to

produce a large quantity of soot in the flame. After a period of 20-30 minutes of immersion in such a flame, the stainless steel probe was almost completely plugged with carbon deposits, while the quartz probe was essentially clean and free of any soot accumulation.

#### Durability of the Quartz Probe

The choice of a quartz microprobe to serve as the tip of the present sampling probe is largely based on consideration of the several important advantages which characterize a quartz microprobe, such as ideal nozzle configuration, lower soot formation, surface inertness and less severe thermal effects. However, there are also some inherent problems associated with the use of the quartz microprobe that must be solved before it can be successfully applied for combustion sampling. Obviously, due to the fragility of the quartz material, shielding of the quartz tip must be provided. Leak-tight coupling of the quartz probe with the probe body is also required and may be a problem. The thermal conductivity of the quartz material is known to be several orders of magnitude smaller than that of metals. Finally, it is necessary to prevent melting of the quartz tip in a hostile, high-temperature combustion environment. All these requirements necessitate extensive innovation and sophistication in the overall probe design.

APPENDIX D  
A REVISED CALCULATION OF THE GAS  
FLOWFIELD IN THE PRESENT PROBE SAMPLING SYSTEM

In Appendix B, the gas flowfield within a sampling probe which is inserted in a combustor operated under conditions typically found in a ramjet combustor was characterized. Detailed profiles of the velocity, temperature, pressure, and density of the sampled gas from the region of the presampling zone to the region where the sample is introduced into the detector (mass spectrometer) were obtained, subject to various assumptions and approximations. This flowfield characterization yielded a better understanding of the probe sampling event. The results of this characterization also provide a basis for the evaluation of various effects, including aerodynamic disturbance, thermal disturbance, and reaction quenching on the validity of the gas species concentration measurements accomplished with the present probe sampling techniques.

In the present section, the calculations relating to flowfield characterization which were described in Appendix B are further revised in two aspects. It is expected that, under the probe sampling conditions to be encountered, a series of shock waves will be initiated at some distance downstream of the sampling orifice. During such a shock, a sharp rise in the gas temperature and pressure will occur, along with a sharp decrease in the gas velocity. The detailed characterization of such a shock process is very difficult and consequently was ignored in the previous calculations since it is highly dependent on the geometry of the sampling probe configuration. In the present section, it is assumed that the sampling probe head has a simple cone-shaped configuration,

as shown in Fig.20. The exact cross sectioned area of the probe at any given point between the probe orifice (point b) and the base of this cone (point d) can be readily calculated for a probe having specified dimensions at points b and d. By further assuming a one-dimensional normal shock, the treatment of which is well-established, it is possible to locate the position of the shock wave and calculate the increases in the gas pressure, velocity, temperature and density across this shock wave. This revision in the treatment provides a more detailed characterization of the flow field within the initial portion of the gas sampling probe, although the assumption of a one-dimensional normal shock may still represent a gross simplification in comparison with the situation actually occurring inside the probe.

The second revision of the previous flow field calculation concerns the profiles of the gas velocity, density and pressure within the gas transfer line (between d and c in Fig. 20). In the previous calculation, these profiles were obtained using a simplified form of Poiseuille's equation, without explicitly taking into account the variation of the temperature and viscosity of the sampled gas along the gas transfer line. This is corrected in the present calculation, which results in more accurate profiles of these parameters.

Shown in Fig.20 is a schematic illustration of the current sampling probe system, and the calculated profiles of the gas velocity ( $V$ ), temperature ( $T$ ), pressure ( $P$ ) and density ( $\rho$ ) along the entire probe sampling system. Since the major portion of these profiles, and their derivation, have been discussed in detail previously, the present discussion will be focused mainly on the revisions. However, for the sake of continuity, a brief description of the over-all calculation procedure and the assumptions employed will also be provided.

The sampling probe shown schematically in Fig. 20 is assumed to consist of a cone-shaped head portion (between b and d, 1 cm) and a probe body (between d and e, 3/16 in. ID X 10 ft.). The entire wall of the probe is maintained at a constant wall temperature of 150°C to prevent condensation of the water present in the probe line. The probe has a sonic sampling orifice (at b) with an assumed orifice diameter of 0.015 inch. This probe is placed in a combustion gas flow field with conditions as defined in the figure. The sampled gas, after traveling the entire length of the probe will enter the detector (mass spectrometer) which is located in the vicinity of point e. The gas pressure at this point is largely dictated by the available pumping capability. It is assumed that a mechanical pump with pumping speed of 500 liter/min is utilized. The sampled gas is assumed to be an ideal gas having the same properties as air, which greatly simplifies the later calculation.

As described in the previous section, due to the strong suction exerted by the sampling orifice (point b), all incoming gas that passes through a disc having a diameter of 0.094 cm (0.037 in.), at line a, will be deflected toward the center line. It is calculated that the range of this flow field disturbance (i.e. between a and b) is 0.084 cm. (0.033 in.) which is approximately two times larger than the diameter of the probe orifice, 0.038 cm. (0.015 in.). Within this region the velocity of the gas will be rapidly increased, with a concurrent decrease of the gas density, pressure and temperature, in an isentropic process. Eventually, all of this gas will pass through the sampling orifice at point b.

It has been shown experimentally that a quartz probe orifice constructed by a standard fabrication process closely resembles an ideal nozzle, which means that the gas velocity at the orifice will reach sonic velocity in an isentropic process, provided that the down stream pressure conditions can meet a given

requirement. The gas sampling rate,  $Q$ , can be readily calculated to be 0.0333 g/sec under the present sampling conditions. The temperature, velocity, density and pressure of the sampled gas at point b can also be determined and are as follows:  $T_b = 1891^{\circ}\text{K}$ ;  $V_b = 8.72 \times 10^4 \text{ cm/sec}$ ;  $\rho_b = 3.34 \times 10^{-4} \text{ g/cm}^3$ ;  $P_b = 1.81 \times 10^6 \text{ dyne/cm}^2$ . The gas transit time within this region can also be calculated to be  $2.6 \times 10^{-6} \text{ sec}$ . It is seen here that the sampled gas has been aerodynamically cooled by  $382^{\circ}\text{K}$  within this period of time which corresponds to a quenching rate of  $1.5 \times 10^8^{\circ}\text{K/sec}$ .

Due to the geometry of the nozzle, once the sampled gas passes through the orifice it further experiences an aerodynamic expansion with a rapid increase (supersonic) in velocity, at the expense of the gas temperature in an isentropic process. Eventually, a point is reached (line c) beyond which no further increase of velocity can be sustained, and a series of non-isentropic shock waves are initiated. After these shock waves (line c') the gas velocity is restored to subsonic speed, which is accompanied by a sharp rise in the gas temperature, pressure and density.

Beyond line c', the gas motion will again become characteristic of that for an isentropic process, owing to the divergent configuration of the probe cone (between c' and d). However, the assumption of an isentropic process is no longer valid once the gas passes point d, beyond which the gas temperature will be gradually cooled by the probe wall, which is water-cooled to a constant temperature of  $150^{\circ}\text{C}$ . The gas flow within the entire region between points d and e is largely viscous, and is dictated by the probe line configuration and the pumping system.

It is noted that between points a and d the sampled gas has essentially experienced a series of isentropic contraction and expansion processes, except during the period of the shock which is a non-isentropic process. However, even this process can be assumed to be adiabatic, since the normal shock can be assumed to be of infinitely thin length and short duration, during which period, very little energy can be dissipated to the environment (such as the probe wall). Therefore, the gas conditions between these two points can be related by the following energy conservation equation,

$$C_p T_a + 1/2 V_a^2 = C_p T_d + 1/2 V_d^2 \quad (D-1)$$

This, along with the continuity equation (D-2)

$$Q = V_d \rho_d A_d = 0.0333 \text{ g/sec} \quad (D-2)$$

and the viscous flow equation, which describes the gas flow within the transfer line (between d and e), the detail of which will be described later, permit determination of the gas condition at point d, which are as follows:  $T_d = 2264^\circ\text{K}$   $V_d = 1.6 \times 10^4 \text{ cm/sec}$ ;  $\rho_d = 1.18 \times 10^{-5} \text{ g/cm}^3$ ; and  $P_d = 7.7 \times 10^4 \text{ dyne/cm}^2$ .

As seen in Fig.20 it is assumed that a normal shock occurs at the region between points c and c'. Since the normal shock can be assumed to be of arbitrarily short distance, it follows that the cross sectional areas at these two points are equal, that is,

$$A_c = A_{c'} \quad (D-3)$$

It is also noted that these areas are related to the distance between points b and c, because it has been assumed that the probe head is of a simple cone-shaped geometry.

According to elementary one-dimensional gas dynamics, the ratio of the pressures ( $P_{c'}/P_c$ ) across a normal shock can be expressed as,

$$P_{c'}/P_c = 1 + 2\gamma/(\gamma + 1)M_c^2 - 1 \quad (D-4)$$

in which  $\gamma$  is the ratio of the specific heat of the gas at constant pressure to that at constant volume (1.4 for air); and  $M_c$  is the Mach number of the gas at point c. For an ideal gas the number,  $M_c$ , is readily calculable once the gas velocity and temperature at point c have been obtained, that is,

$$M_c = V_c/(\gamma R T_c)^{1/2} \quad (D-5)$$

For an isentropic process, the gas conditions at points b and c are related by the following equations:

$$P_c/P_b = (\rho_c/\rho_b)^{\gamma} (T_c/T_b)^{\gamma/(\gamma - 1)} \quad (D-6)$$

$$Q = \rho_c V_c A_c = 0.0333 \text{ g/sec} \quad (D-7)$$

$$C_p T_b + 1/2 V_b^2 = C_p T_c + 1/2 V_c^2 \quad (D-8)$$

Similarly, the gas conditions at points c' and d are related by the following equations:

$$P_{c'}/P_d = (\rho_{c'}/\rho_d)^{\gamma} = (T_{c'}/T_d)^{\gamma/(\gamma - 1)} \quad (D-9)$$

$$Q = \rho_{c'} V_{c'} A_{c'} = 0.0333 \text{ g/sec} \quad (D-10)$$

$$C_p T_d + 1/2 V_d^2 = C_p T_{c'} + 1/2 V_{c'}^2 \quad (D-11)$$

The gas conditions at both points b and d are known, as has been presented previously. This, along with the above state equations (D-3 to D-11), will lead to one, and only one, set of self-consistent solutions, which corresponds to the position of the normal shock as well as the gas conditions at the points c and c'. These are the following:

Distance between b and c = 0.65 cm

$$T_c = 244^\circ\text{K}$$

$$V_c = 2.02 \times 10^5 \text{ cm/sec}$$

$$\rho_c = 2.0 \times 10^{-6}$$

$$P_c = 1.4 \times 10^3 \text{ dyne/cm}^2$$

$$T_{c'} = 2209^\circ\text{K}$$

$$V_c' = 3.7 \times 10^4 \text{ cm/sec}$$

$$\rho_c' = 1.1 \times 10^{-5} \text{ g/cm}^3$$

$$P_c' = 7.0 \times 10^4 \text{ dyne/cm}^2$$

with the above-established boundary conditions, as well as those of points a, b, and d, the detailed profiles of the gas temperature, velocity, density and pressure over the range between a and d can be obtained using equation similar to (D-6) to (D-11) as indicated in Fig.20. Also shown in Fig.20 are the gas transit times within each section.

As discussed in the previous section, the cooling of the sampled gas (by wall convective cooling) along the transfer line (that is between d and e) can be treated quite accurately as an incompressible laminar flow, for which the Nusselt number is known to be 3.658. By explicitly taking into account the variation of the thermal conductivity ( $k$ ) as a function of gas temperature, based on reported tabulated data, the temperature profile of the sampled gas along the transfer line can be expressed by the following analytical equation,

$$(T_x - 423)/(T_x + 45) = \exp [-0.0678x - 0.226] \quad (D-12)$$

The term  $x$  is the position along the transfer line which ranges from zero (at e) to 300 cm (at d). A plot of  $T_x$  vs.  $x$  is also shown graphically in Fig. 20.

For a given temperature profile, the distribution of the gas pressure within the transfer line can be derived, based on the well known Poiseuilles law, which is expressed in the following basic form,

$$Q = (M/RT)(\pi D^4/128n)(P)(dP/dx) \quad (D-13)$$

The term  $n$  is the viscosity of the gas at the given temperature,  $T$ , and can be approximated by the following equations within the temperature range of 300°K to 2500°K, according to the reported tabulated data (Natl. Bur. Stand. Circ. 564, 1955),

$$\eta \text{ (in poise } \times 10^4) = 1.45 + 2.55 \times 10^{-3}T \quad (D-14)$$

The profile of gas pressure within the transfer line as shown in Fig. 20 is obtained by numerical integration of the equation (D-13) by taking into account the variations of the gas temperature and viscosity, as represented by equations (D-12) and (D-14) respectively. The initial drop of the gas pressure within the first few cm is due to the cooling of the gas by wall convective cooling, while the broad drop of the pressure at the later portion is largely due to the pumping action at the outlet (point e).

Consequently, the profiles of the gas density and velocity within the transfer line can be readily obtained from the equation for an ideal gas (D-15), and the continuity equation, (D-16), respectively,

$$\rho_x = P_x M/RT \quad (D-15)$$

$$Q = \rho_x V_x A = 0.0333 \text{ g/sec} \quad (D-16)$$

Both those two profiles are shown in Fig. 20. Also shown is the gas transit time (0.054 sec) within the transfer line, which is again obtained by numerical integration. This value can be compared with the result (0.062 sec) obtained in a previous calculation without taking into account the variation of the gas temperature and viscosity.

In the previous section a discussion of the validity of gas species concentration measurements using the present probe sampling system was provided. For the purpose of illustration, an in-depth analysis of the quenching of the reaction of CO (from further oxidation to  $\text{CO}_2$ ) within the present sampling probe system was also provided. This analysis, to a large extent, was based on the knowledge derived from characterization of the flowfield in the sampling probe system. In view of the present revision of the flowfield characterization it is desirable that this analysis also be revised accordingly. Although this work is yet to be

accomplished, it is expected that the new result, which may affect the quantitative evaluation of the quenching efficiency, will not alter the general conclusions reached previously relevant to the aspects of aerodynamic disturbance, thermal effects, quenching and sampling resolution in the present probe sampling system.

AD-A114 854

WRIGHT STATE UNIV DAYTON OHIO  
MASS SPECTROMETRIC MEASUREMENTS OF THE CONCENTRATIONS OF GASEOU<sup>-</sup>ETC(IU)  
APR 82 C CHANG, T O TIERMAN

F33615-78-C-2066

NL

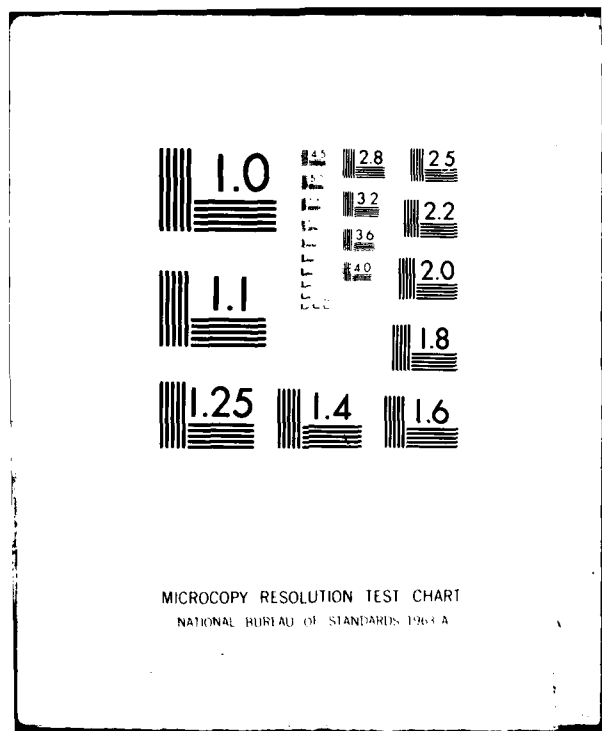
UNCLASSIFIED

AFWAL-TR-81-2139

3-1 3

8-9-82

END  
DATE  
8-9-82  
DTIC



## APPENDIX E

### ANALYSIS OF THE DIGITAL MASS PROGRAMMER AND THE SIGNAL DEMULTIPLEXING MODULES

As described in the previous section, a digital mass programmer (DMP, Model 091-6) and two signal demultiplexing modules (DM, Models 091-8 and 091-9, one each) were acquired from Extranuclear Laboratories, Inc. Considerable effort was devoted to systematic checking of these units, and the interfacing of these units to the mass spectrometer and the computer facility.

Shown in Fig. E-1 is a schematic diagram of the interface between the DMP and DM units and the mass spectrometer. Depending on the setting of the DMP, a series of up to 16 ion signals are acquired by the electron multiplier in sequential form, and transmitted to the electrometer (031-1) for further amplification. The output signals from the electrometer are then transferred to the DM unit input. As seen in the figure a bucking circuit is provided in the DM unit. Depending on the address command set in the DMP unit each channel of the 16 different ion signals can be individually zeroed-out by simply turning the bucking dial knob provided for each channel on the DM unit. Therefore, the background ion signal in each channel can be eliminated before any further processing.

The bucked ion signal from the DM is applied to the input of the DMP and amplified by the channel-programmed gain (x 00.0 to 99.9,

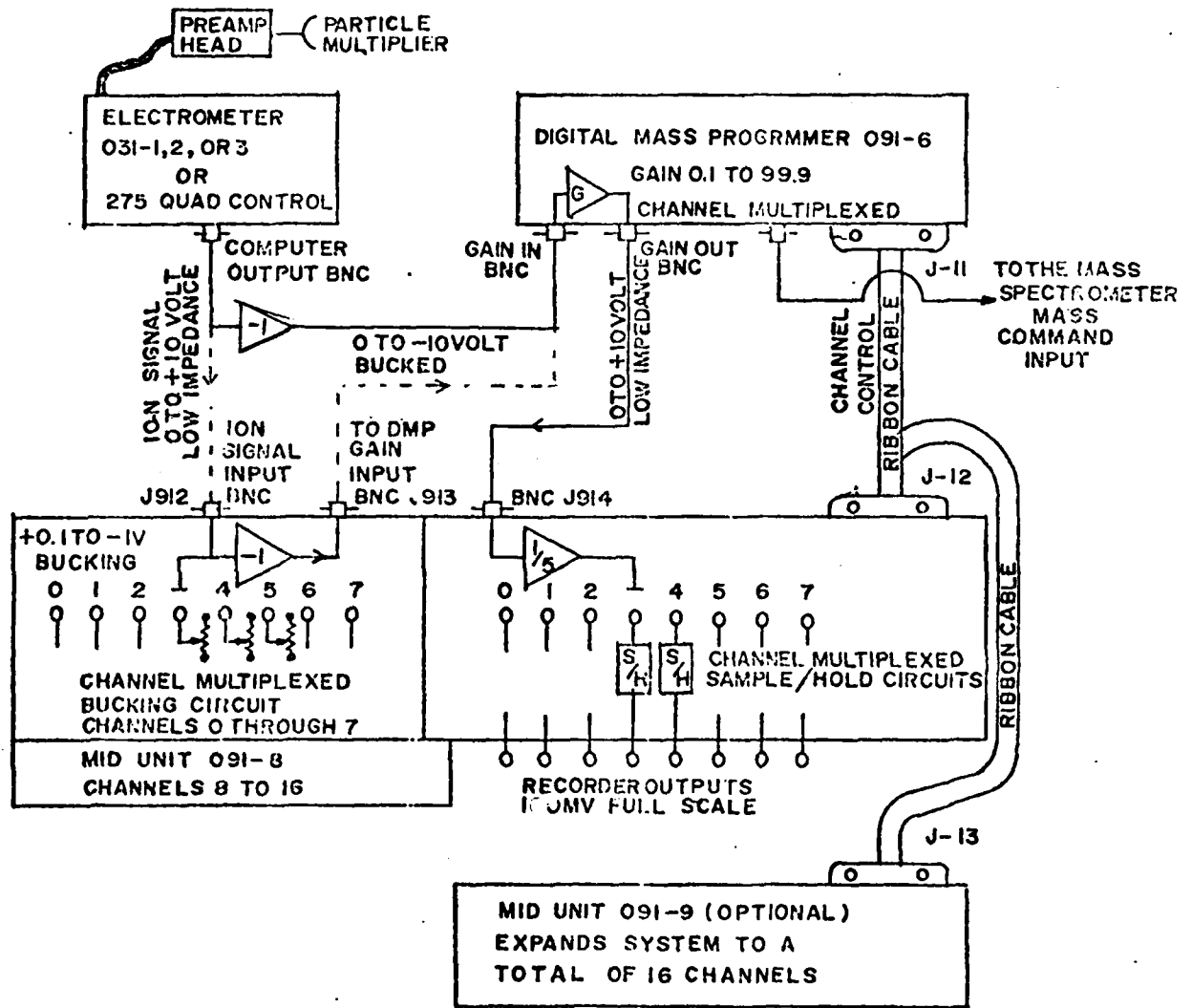


Figure E-1. Schematic Diagram of the Interface Between the DMP and DM Modules and the Mass Spectrometer.

individually set for each channel). The bucked and amplified ion signals (still in sequential form) are then transmitted back to the DM unit, in which the ion signals are divided by a factor of 5, and applied to a demultiplexing circuit. This circuit demultiplexes the incoming 16 sequential ion signals and applies each demultiplexed ion signal to a selected sample/hold (S/H) circuit capacitor via the selected time constant resistor. Each of these S/H circuits is capable of retaining the last-received signal (in a given channel) until the next signal (in the same given channel) is received. This effectively allows all sixteen ion channel signals to be acquired "simultaneously" and presented at sixteen individual output channels on the DM units.

It is recognized that the settings of the 16 bucking dials on the DM units can artificially alter the DM unit outputs. Therefore, each of these 16 dials must be carefully preset before each test. During the initial check it was found that these dials can provide only very coarse adjustment, and are lacking in fine tuning capability. Furthermore, the tuning knobs were found to be physically loose, and it seemed likely that during a test, any vibration of the instruments would result in unintended changes in the dial settings. In view of these considerations, and the fact that any desired background ion signal subtraction can be readily achieved by using the computer data processing system, it was felt that use of the ion bucking system provided on the DM units should be avoided. To permit this the modification shown in Fig. E-1 is required. The output signals from the electrometer were directly applied to the "Gain In" input of the DMP unit and by-pass the bucking circuit. In this way, the bucking dials on the DM units have no effect. In order

to preserve an accumulating mass spectrum, the Gain Amplifier Inverting Switch inside the DMP chassis must be turned to "Inverted" position.

The next task which had to be accomplished in checking the system was to determine the correspondance between the ion mass (m/e) and the "start AMU" setting on the DMP unit. The results are shown in Fig. E-2. It appears that the "start AMU" setting varies linearly with the ion mass. Of course, the plot shown here serves only as a guide, since the shape of this plot may be affected by various instrument parameters (such as  $\Delta M$ , pole Bias, Resolution dials on the mass spectrometer and the Mass Vernier, Span dials on the DMP unit) whose settings are likely to be readjusted prior to each test in order to optimize the system performance.

The sample/hold circuit used in the DM units is basically an operational amplifier-integrator. During the sample period the input signal,  $V_i$ , charges a circuit capacitor, C, through whatever resistance, R, the input circuit offers. The operational amplifier is in the "follower" configuration and its output,  $V_o$ , will follow the amplitude of the input signal,  $V_i$ , according to the following equation, (which will be discussed further in a later section)

$$\frac{V_o}{V_i} = 1 - \exp(-t/RC) \quad (E-1)$$

in which t is the sampling period, and RC is the circuit time constant.

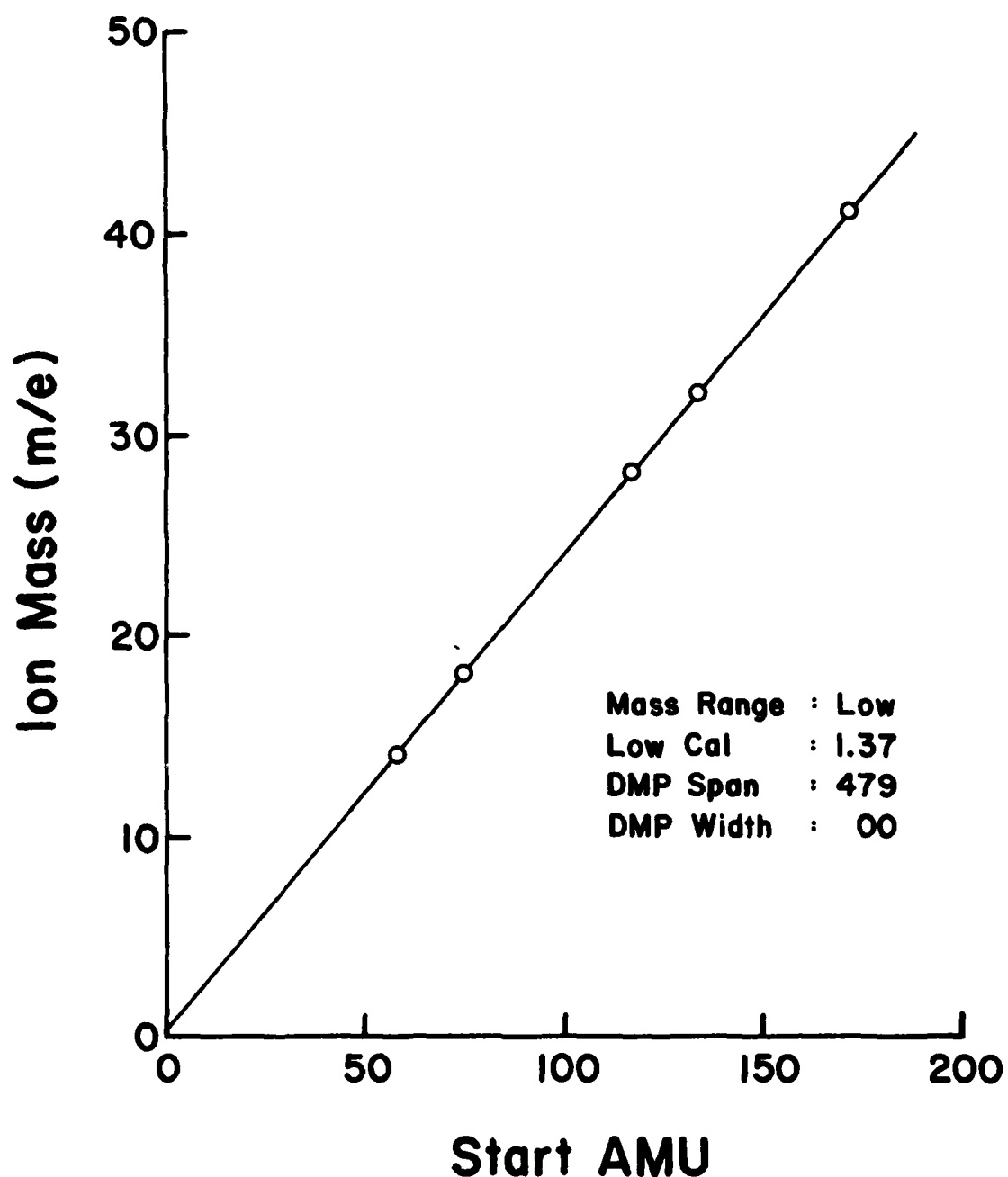


Figure E-2. The Ion Mass As a Function of the "Start AMU" Control Settings.

The time constant,  $RC$ , must be appropriate to the signal that is to be sampled, that is, sufficiently short for the sampling to reflect the frequency of the signal, but sufficiently long to allow some averaging of the high-frequency noise that is inevitably present. The current DM units provide three switchable time constants (0.1, 0.3 and 1.0 sec) which are probably chosen largely based on the system performance consideration. As clearly shown in Eq. (E-1), the sampling period,  $t$ , must be at least three times longer than the time constant,  $RC$ , in order to ensure that the DM output,  $V_o$ , is the same as the mass spectrometer ion signal,  $V_i$ .

Eq. (E-1) can be rearranged to yield

$$\log \left( 1 - \frac{V_o}{V_i} \right) = \frac{-1}{RC} \cdot t \quad (E-2)$$

Shown in Fig. E-3 are plots the measured  $\log \left( 1 - \frac{V_o}{V_i} \right)$  as a function of sampling time,  $t$ , at three different time constant settings. The time constants ( $RC$ ) measured from the slopes of these plots are found to be 0.13, 0.35, and 1.03 sec. respectively, in good agreement with the manufacturer's quoted values.

Since the shortest time constant available is 0.1 seconds, information time responses of less than 0.3 sec. are not practical. This requirement may not pose a problem in normal mass spectrometric operation. However, in dealing with a rapidly changing environment, such as the one presented in a turbulent combustion flow field, in which temporal resolution smaller than 0.1 sec is often desirable, the present DM operation will be inadequate.

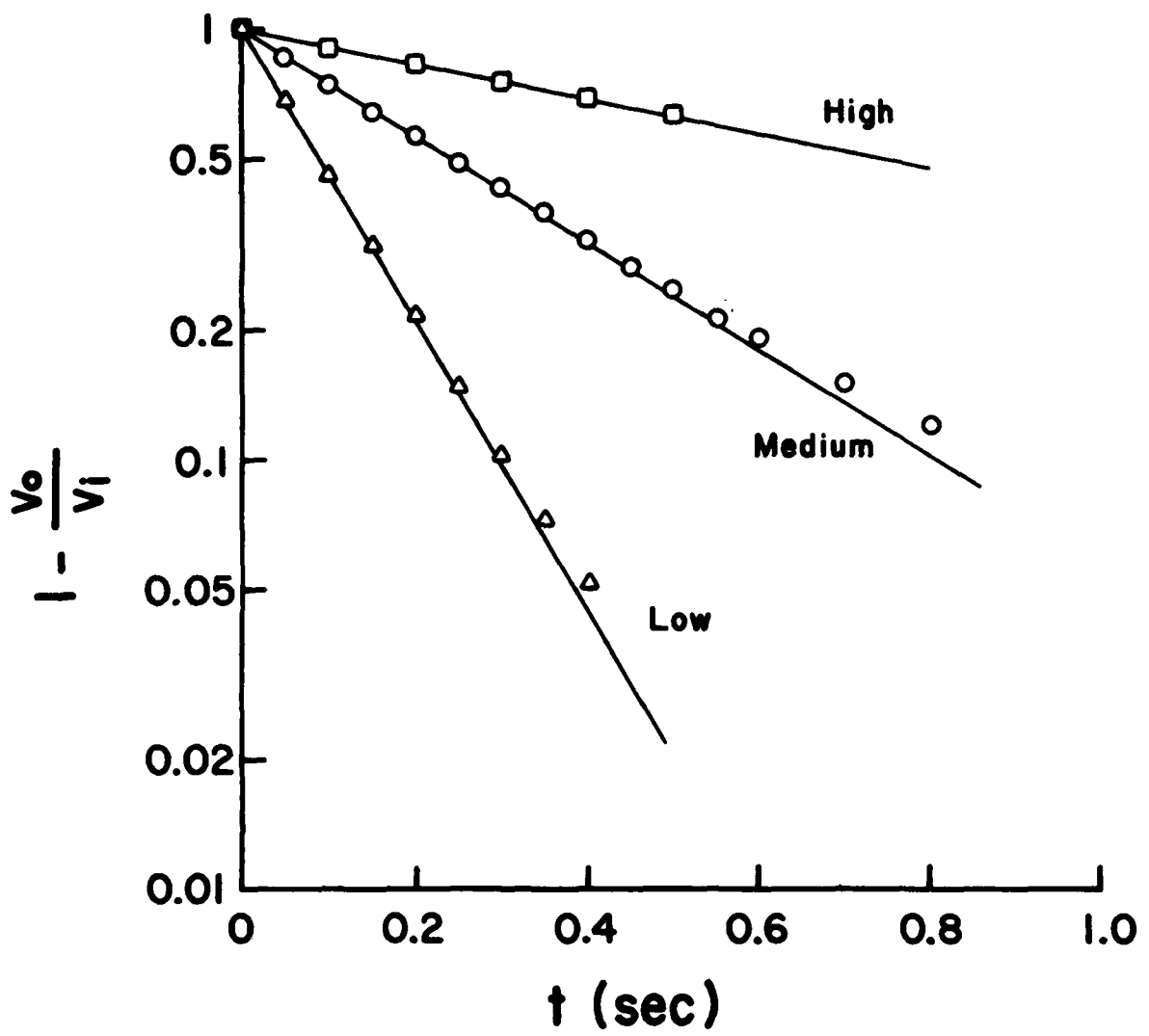


Figure E-3.  $\log (1 - \frac{V_0}{V_i})$  As a Function of Sampling Time.

Faced with this problem, it is helpful to reconsider the relationship between DM output signal,  $V_o$ , and the mass spectrometer ion signal,  $V_i$ , as presented in Eq. (E-1). Even in the case where the sampling period,  $t$ , is shorter than the time constant,  $RC$ , and the observed value of  $V_o$  is different from that of  $V_i$ , one can still arrive at the value of  $V_i$  based on the measured value of  $V_o$ , as long as the relationship between these two quantities can be expressed by a relation such as that shown in Equation (E-1). Eq. (E-1) holds only in one special case, however. This, at least in principle, points out the way to allow for faster system response and to improve the temporal resolution. To achieve this, the following two tasks must be performed: 1) the operation of the mass spectrometer (including cycle advance, data recording, etc.) must be externally controlled by an interfaced computer, such that an explicit relationship between the time of sampling,  $t$ , and the recorded value of  $V_o(t)$  can be established; and 2) the mathematical relationship between  $V_i(t)$  and  $V_o(t)$  at any given time,  $t$ , during a test must be obtained so that the value of  $V_i(t)$  can be derived from the experimentally measured value of  $V_o(t)$ . Further discussion relating to the implementation of these two tasks is provided in the following section.

Shown in Fig. E-4 is a schematic representation of the time sequence of events in the proposed data acquisition process. The cyclic operation of the mass spectrometer is controlled by the DMP unit in the usual manner. Within each cycle a total of 15 different ion mass channels can be sequentially scanned. The duration of each cycle can be as short as 0.1 sec., although a much shorter duration is possible, but not recommended,

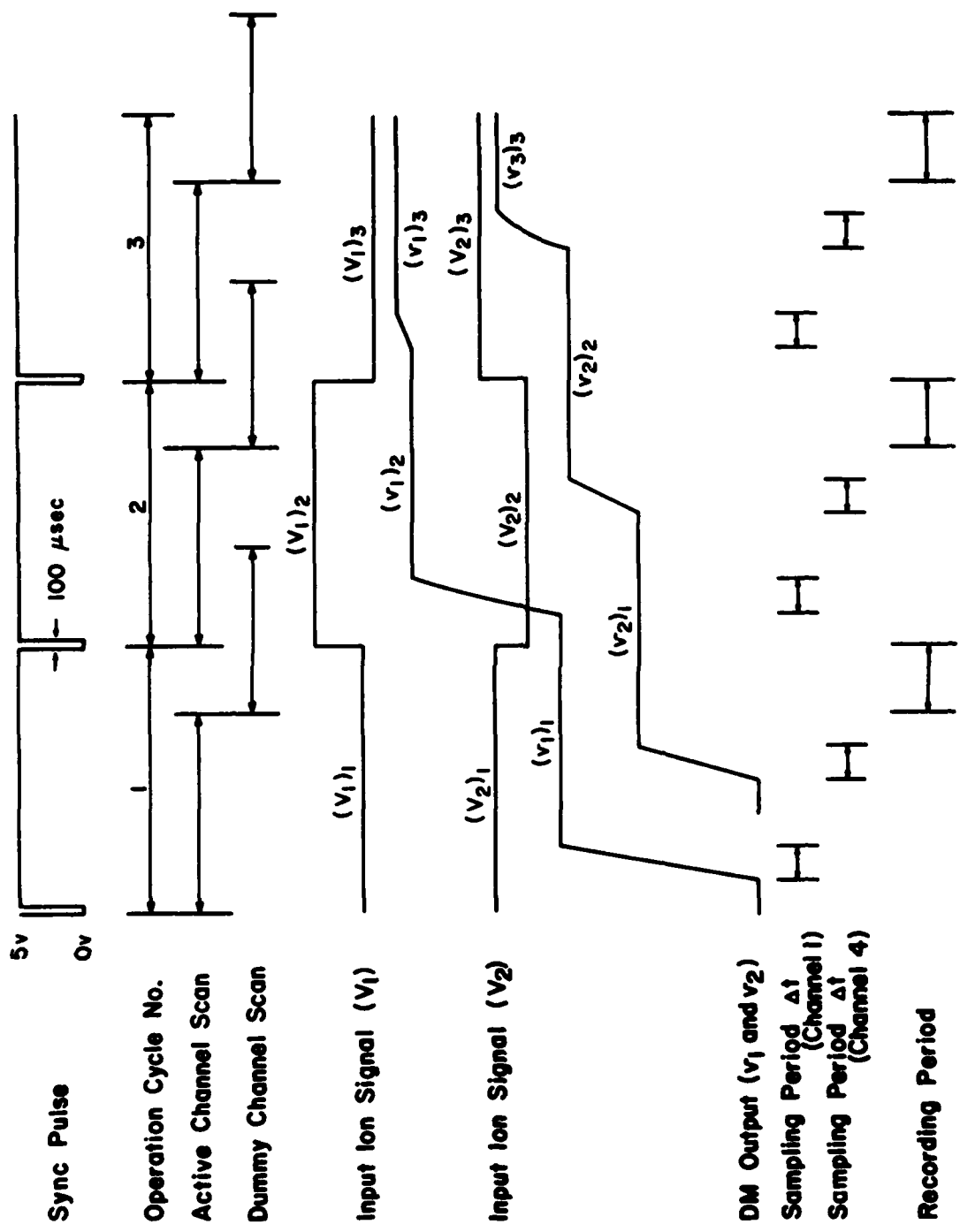


FIGURE E-4. Time Sequence of Events in the Data Acquisition Process.

since too much time will be wasted in channel switching (5 msec per switching event).

In the proposed data acquisition scheme, the initiation of each operating cycle must be synchronized with the interfaced computer clock, such that the exact time [t, see Eq. (E-1)] can be assigned to each acquired data point  $V_0(t)$ . This is achieved in the following manner. An external command post (J-11, A-16) is provided in the DMP chassis. Application of a TTL (transistor-transistor-logic) low pulse (that is, a ground potential pulse 100  $\mu$ sec wide) to this post will end the current channel scan, advance to the next channel, and start the next channel scan as instructed. A pulse of this type (see Fig. E-4) can be readily provided by the interfaced computer, by making an appropriate software program modification. As shown in Fig. E-4, each operating cycle consists of an "active" channel scan period, during which a total of up to 15 ion channels are sequentially scanned, and a "dummy" channel scan period (the last channel of the 16 total available) which is arbitrarily assigned to an ion mass of no interest for the test. However, the total time allocated for these two periods, as initially entered through the DMP panel, is somewhat longer (by  $\sim 20\%$ ) than the operation cycle duration as dictated by the computer sync pulse (see Fig. E-4). In this manner, shortly after the initiation of the test, the DMP cyclic operation will be quickly brought into synchronization with the computer sync pulse control. Thereafter, the sync pulse will always fall during the execution of the dummy channel scan and prematurely end this channel scan, and then advance the DMP to the next

channel, that is, to the next operating cycle.

Also shown in Fig. E-4 are the traces of the input ion signals,  $(v_i)_j$ , designated as the input ion signal (from the mass spectrometer, after DMP amplification) for ion mass channel  $i$  during the  $j$ th operation cycle. The resultant DM output signals (as acquired by the computer),  $(v_i)_j$ , designated as the DM output signal for ion mass channel  $i$  during the  $j$ th operation cycle, are also shown in this figure. It is seen in this figure that the change of the  $(v_i)_j$  signal level only occurs during the sampling period  $\Delta t$ , typically 5-50 msec) allocated for the ion mass channel  $i$  within each operating cycle. For the rest of the time the signal  $(v_i)_j$  remains unchanged due to the "hold" operation of the sample/hold circuit. In a rapidly changing environment, where the species concentration level may change from cycle to cycle, the observed signal,  $(v_i)_j$ , will not be the same as the signal,  $(v_i)_j$ , due to the slow response of the DM circuit. However, a relationship between these two values must exist during any operating cycle. A mathematical derivation of this relationship is provided in the following section, which would allow the calculation of the  $(v_i)_j$  value based on the obtained  $(v_i)_j$  value.

For simplicity, in the following the subscript  $i$  is dropped for the case where only one channel is being considered.

### I. At Cycle 1. (j = 1)

Input voltage =  $v_1$

During the sampling period, ( $\Delta t$ ), the DM output is increased from 0 to  $v_1$ , and holds its final value,  $v_1$ , after the completion of sampling.

Referring to the sample and hold circuit (Fig. E-5),

$$(v_1)_t = iR + \frac{0}{C} = i_t R + v_t \quad (E-3)$$

and during the sampling period,  $v_1 = \text{const.}$  ( $t = 0$  to  $\Delta t$ ).

The differential of Eq. (E-3) yields,

$$\frac{dv}{dt} = R \frac{di}{dt} + \frac{i}{C} = 0. \quad (\text{for } t = 0 \text{ to } \Delta t) \quad (E-4)$$

$$\frac{di}{i} = -\frac{1}{RC} dt \quad (E-5)$$

The integration of Eq. (5) from  $t = 0$  to  $t$  yields,

$$\ln \frac{i}{i_0} = -\frac{t}{RC}$$

$$\text{or } i_t = i_0 \exp \left( -\frac{t}{RC} \right) \quad (E-6)$$

The  $i_0$  can be obtained from the initial condition.

At  $t = 0$

$$v_1 = i_0 R + 0 \quad (E-7)$$

$$i_0 = +\frac{v_1}{R}$$

$$\text{So, } i_t = \frac{v_1}{R} \exp \left( -\frac{t}{RC} \right) \quad (E-8)$$

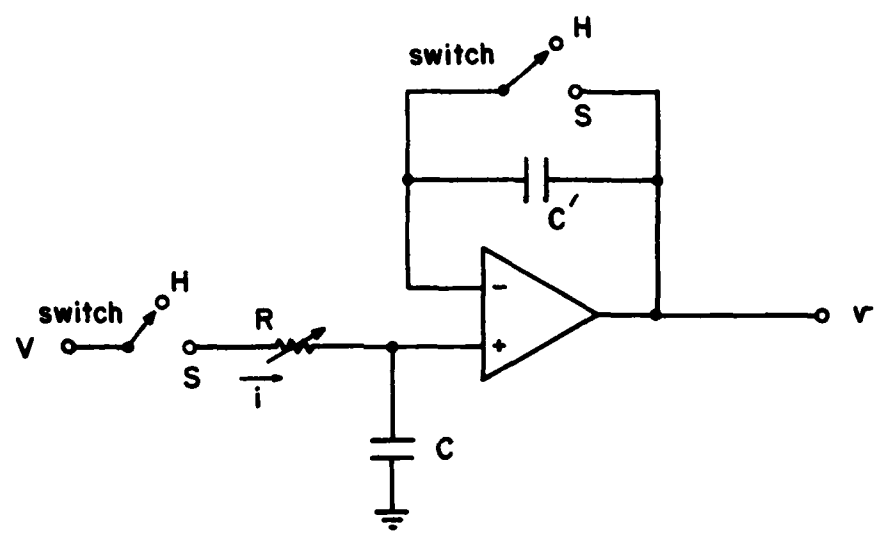


Figure E-5. Schematic of the Sample/Hold Circuit.

and,

$$\begin{aligned}(V_1)_t &= V_1 = i_t R + v_t \\ &= V_1 \exp \left( -\frac{t}{RC} \right) + v_t\end{aligned}\quad (E-9)$$

At  $t = \Delta t$ , Therefore,

$$v_{t=\Delta t} = v_1 = V_1 \left[ 1 - \exp \left( -\frac{\Delta t}{RC} \right) \right] \quad (E-10)$$

## II. At Cycle 2 (j = 2)

Input Voltage =  $V_2$

During sampling, the DM output voltage will be increased from  $v_1$  at  $t = 0$  to  $v_2$  at  $t = \Delta t$ .

The value of  $v_1$  is obtained previously, that is,

$$v_1 = V_1 \left[ 1 - \exp \left( -\frac{\Delta t}{RC} \right) \right]$$

Again, during sampling,

$$(V_2)_t = V_2 = i_t R + \frac{Q}{C} = i_t R + v_t \quad (E-11)$$

Differentiation of Eq. (11) yields,

$$\frac{dV_2}{dt} = 0 = R \frac{di}{dt} + \frac{1}{C} \quad (E-12)$$

Integration of Eq. (12) from  $t = 0$  to  $t = \Delta t$  yields,

$$i_{\Delta t} = i_0 \exp \left( -\frac{\Delta t}{RC} \right) \quad (E-13)$$

The expression of  $i_0$  is obtained as follows,

At  $t = 0$

$$v_2 = i_0 R + v_1$$

Therefore,  $i_0 = \frac{1}{R} [v_2 - v_1]$

$$= \frac{1}{R} [v_2 - v_1 [1 - \exp(-\frac{\Delta t}{RC})]] \quad (E-14)$$

Substituting Eq. (14) into Eq. (13), one obtains,

$$i_{\Delta t} = \frac{1}{R} [v_2 - v_1 [1 - \exp(-\frac{\Delta t}{RC})]] \exp(-\frac{\Delta t}{RC}) \quad (E-15)$$

Therefore, at  $t = \Delta t$ ,

$$v_2 = i_{\Delta t} R + v_2$$

Therefore,  $v_2 = v_2 - [v_2 - v_1 [1 - \exp(-\frac{\Delta t}{RC})]] \exp(-\frac{\Delta t}{RC})$

$$= v_2 [1 - \exp(-\frac{\Delta t}{RC})] + v_1 [1 - \exp(-\frac{\Delta t}{RC})] \exp(-\frac{\Delta t}{RC})$$
$$= v_2 [1 - \exp(-\frac{\Delta t}{R})] + v_1 \exp(-\frac{\Delta t}{RC}) \quad (E-16)$$

or,

$$v_2 - v_1 \exp(-\frac{\Delta t}{RC}) = v_2 [1 - \exp(-\frac{\Delta t}{R})] \quad (E-17)$$

Equation (E-16) and (E-17) provide the relationship between the observed DM output signal,  $v_2$ , and the input signal,  $v_2$ , during the second operating cycle. It is interesting to note that  $v_2$  cannot be derived exclusively based on the information of  $v_2$  alone, and the measured value of  $v_1$  obtained during the previous cycle must also be available for the derivation of  $v_2$ .

### III. At Cycle 3 (j = 3)

Input signal =  $v_3$

During the sampling the DM output voltage will be changed from  $v_2$  to  $v_3$ . The expression of  $v_2$  has been obtained from equation (E-16).

At  $t = 0$ ,

$$v_3 = i_0 R + v_2$$

$$i_0 = \frac{1}{R} (v_3 - v_2)$$

$$= \frac{1}{R} [v_3 - v_2 (1 - \exp(-\frac{\Delta t}{RC})) - v_1 \exp(-\frac{\Delta t}{RC})] \quad (E-18)$$

At  $t = t$ ,

$$v_3 = i_t R + v_t = i_t R + \frac{Q}{C} \quad (E-19)$$

Differentiation of Eq. (19) yields,

$$0 = R \frac{di_t}{dt} + \frac{i}{C} \quad (E-20)$$

Integration of Eq.(E-20) from  $t= 0$  to  $t = \Delta t$  yields,

$$\begin{aligned} i_{\Delta t} &= i_0 \exp(-\frac{\Delta t}{RC}) \\ &= \frac{1}{R} [v_3 - v_2 (1 - \exp(-\frac{\Delta t}{RC})) - v_1 \exp(-\frac{\Delta t}{RC})] \cdot [\exp(-\frac{\Delta t}{RC})] \\ &= \frac{1}{R} [v_3 - v_2] \cdot \exp(-\frac{\Delta t}{RC}) \end{aligned} \quad (E-21)$$

At  $t = \Delta t$

$$v_3 = i_{\Delta t} R + v_3$$

Therefore,

$$\begin{aligned} v_3 &= v_3 - i_{\Delta t} \cdot R \\ &= v_3 [1 - \exp(-\frac{\Delta t}{RC})] + v_2 \cdot \exp(-\frac{\Delta t}{RC}) \end{aligned} \quad (E-22)$$

or,

$$v_3 - v_2 \cdot \exp(-\frac{\Delta t}{RC}) = v_3 [1 - \exp(-\frac{\Delta t}{RC})] \quad (E-23)$$

It is interesting to note that equations (E-22) and (E-23) are very similar to equations (E-16) and (E-17), respectively.

Similar derivations are applicable for cycles 4, 5 and so on,

It can therefore be generalized that  
for  $j$ th operating cycle,

$$v_j - v_{j-1} \cdot \exp(-\frac{\Delta t}{RC}) = v_j [1 - \exp(-\frac{\Delta t}{RC})] \quad (E-24)$$

or

$$v_j = v_j [1 - \exp(-\frac{\Delta t}{RC})] + v_{j-1} \cdot \exp(-\frac{\Delta t}{RC}) \quad (E-25)$$

The two equations above explicitly show that for any operating cycle, the true input voltage,  $v_j$ , can be derived from the experimentally measured value of  $v_j$  and  $v_{j-1}$ , as long as the sampling period for each channel is maintained constant throughout the experiment.

If during the experiment the channel 0 is tuned to a reference ion (such as  $\text{Ar}^+$ ), while the channel 1 is tuned to an ion characteristic of a gaseous species whose concentration is to be measured, the ratio of the concentration of this species ( $C_1$ ) to that of the argon ( $C_0$ ) during  $i$ th operating cycle can be obtained as follows,

$$\frac{C_1}{C_0} = \frac{k_1}{k_0} \frac{(v_1)_i}{(v_0)_i}$$

$$= \frac{k_1}{k_0} \cdot \frac{(v_1)_i - (v_1)_{i-1} \cdot \exp(-\frac{\Delta t}{RC})}{(v_0)_i - (v_0)_{i-1} \cdot \exp(-\frac{\Delta t}{RC})} \quad (\text{E-26})$$

in which  $k_1$  and  $k_0$  are the sensitivity factors of the gaseous species and argon, respectively.

Following are several special cases in which the derivation of  $v_1$  based on Eq. (E-22) can be simplified.

Case I: At cycle 1 ( $j = 1$ )

$$v_{1-1} = v_0 = 0$$

Eq. (E-24) is thus reduced as follows,

$$v_1 - 0 = v_1 [1 - \exp(-\frac{\Delta t}{RC})] \quad (\text{E-27})$$

This equation is essentially the same as Eq. (E-10).

Case II:

If  $\Delta t \gg RC$  (eg.  $\Delta t > 5 RC$ ),

$$\exp(-\frac{\Delta t}{RC}) \approx 0$$

Eq. (24) is thus reduced to,

$$v_j = V_j [1 - \exp(-\frac{\Delta t}{RC})] \approx V_j \quad (E-28)$$

Equation (E-28) indicates that the capacitor of the sample/hold circuit has been saturated before the end of each sampling period ( $\Delta t$ ). For a mass spectrometer-computer interface operated in the "high" speed integration mode (each operation cycle = 0.1 sec.) the sampling period for each channel is approximately 5 msec. This means that the time constant,  $RC$ , of the sample/hold circuit must be 1 msec or less, which is 100 times lower than the minimum time constant (0.1 sec) provided by the present DM module.

### Case III.

In a steady state environment in which the species' concentration remains unchanged, that is,

$$V_1 = V_2 = \dots = V_f = V \quad (E-29)$$

Equation (E-10) yields,

$$v_1 = V [1 - \exp(-\frac{\Delta t}{RC})] \quad (E-30)$$

and Eq. (E-15) yields,

$$\begin{aligned} v_2 &= V [1 - \exp(-\frac{\Delta t}{RC})] + V [1 - \exp(-\frac{\Delta t}{RC})] \exp(-\frac{\Delta t}{RC}) \\ &= V [1 - \exp(-\frac{\Delta t}{RC})] [1 + \exp(-\frac{\Delta t}{RC})] \\ &= V [1 - \exp(-\frac{2\Delta t}{RC})] \end{aligned} \quad (E-31)$$

Eq. (E-21) yields,

$$\begin{aligned} v_3 &= V[1 - \exp(-\frac{\Delta t}{RC})] + V[1 - \exp(-\frac{2\Delta t}{RC})][\exp(-\frac{\Delta t}{RC})] \\ &= V[1 - \exp(-\frac{3\Delta t}{RC})] \end{aligned} \quad (E-32)$$

Similarly, equation (E-24) will also yield.

$$v_j = V[1 - \exp(-\frac{j\Delta t}{RC})] \quad (E-33)$$

A plot of  $v_j$  vs.  $[1 - \exp(-\frac{j\Delta t}{RC})]$  should therefore yield a straight line, whose slope corresponds to the value  $V$ . However, in reality, this plot is difficult to obtain since one is not certain what is the true value of  $j$  when the first DM output is recorded experimentally. The simplest approach is to let the DM sample the ion signal for a period of 10 sec or more before actual data acquisition. If the data are acquired in the "low" integration mode (that is, operating cycle = 1 sec) sampling period,  $\Delta t = 50$  msec, for each channel) during this 10 second period, the total sampling time for each channel would be 0.5 sec (50 msec x 10 cycles) which is at least five times as large as the time constant (0.1 sec) of the DM circuit. Alternatively, if the data are acquired in the "high" integration mode (that is, operating cycle = 0.1 sec. sampling period,  $\Delta t = 5$  msec, for each channel), during this 10 second period the total sampling time for each channel would also be 0.5 sec. (5 msec. x 100 cycles). Therefore equation (E-33) can be reduced to,

$$v_j = V \quad (E-34)$$

The observed DM output signals will remain constant regardless of the value  $j$ .

It should be noted that, for a steady state condition, there is no real advantage gained using the present operating scheme in comparison with the conventional mass spectrometer-computer interface without synchronization between the DM channel scan and the computer data acquisition. However, in dealing with a rapidly changing environment, such as the one presented in a turbulent combustion flow field, true temporal resolution of ion signals as small as 0.1 sec can be achieved, based on Eq. (E-24), under the present operating scheme. Even faster response can also be obtained if a smaller number of DM channels is to be utilized. On the other hand, in the conventional unsynchronized data acquisition scheme, the temporal resolution attainable is only on the order of 5-10 seconds (assuming 10 or more channels are to be used) owing to the slow response of the DM module.

During the present reporting period several hardware modification and computer program changes were accomplished in order to facilitate the proposed data acquisition scheme. A cable was connected between the DMP chassis (J-11, A16) and the computer clock pulse-controlled pulse generator for providing the TTL low sync pulse. The sync pulse repetition rate was set at one second ("low" integration mode). The active channel scan period was set at approximately 700 msec. The remaining period (300 msec) of the cycle was reserved for DM unit output data

acquisition. A total of 40 A/D samplings (at a rate of approximately 7.3 msec/sample) were acquired and integrated for each channel. Great care was taken in the choice of the exact number of samplings such that the 60 HZ AC noise picked up by the transducer cable could be largely eliminated through this integration process.

Additional work was accomplished during the present reporting period in connecting the DM signal outputs to the interfaced computer as shown in the computer ID sheet presented in Table E-I. This sheet indicates the details of these connections and other pertinent information. It is seen here that each output of the 16 DM channels is branched into two amplifier modules with their amplification gains set at 1 and 10, respectively. This, along with the amplification gain ranging from 0.1 to 99.9 which is provided by the DMP unit, effectively allows two ion signals having intensities different by as much as a factor of  $1 \times 10^4$  to be recorded with equal A/D counts. The Expanded dynamic range greatly facilitates the detection of small signals (such as  $C^+$  from CO) in the presence of ion signals of large intensity (such as  $N_2^+$  from air), which are to be acquired simultaneously.

Several system checks were also performed for the newly acquired DM and DMP units. The results of these checks have been documented in the previous quarterly reports. As a result greater understanding of the performance characteristics of the newly acquired DMP and DM modules have been realized. In spite of several minor problems encountered, these new instruments provide considerable improvements in the mass spectrometer operating capability for future application.

TABLE E-1.  
A REVISED COMPUTER ID SHEET FOR MASS SPECTROMETER DATA ACQUISITION

CHANNEL	RANGE	UNITS	GROUP	WINDOW	CORE COEFFICIENTS	COMMENTS
1 12A	16378.	MV	1	0.	1. 1.00000 P17 X1	DMP GAIN 2.5
2 12B	1308.	MV	1	0.	2. 1.00000 P17 X1	DMP GAIN 2.5
3 11A	16368.	MV	2	0.	3. 1.00000 P17 X1	DMP GAIN 0.5
4 11B	1308.	MV	2	0.	4. 1.00000 P17 X1	DMP GAIN 0.5
5 12A	5.72.	MV	3	0.	5. 1.00000 P17 X1	DMP GAIN 2.5
6 12C	5.72.	MV	3	0.	6. 1.00000 P17 X1	DMP GAIN 1
7 13A	5.22.	MV	4	0.	7. 1.00000 P17 X1	DMP GAIN 1
8 13B	5.22.	MV	4	0.	8. 1.00000 P17 X1	DMP GAIN 1
9 14A	5.06.	MV	5	0.	9. 1.00000 P17 X1	CMP GAIN -
10 14B	5.06.	MV	5	0.	10. 1.00000 P17 X1	A94 U96 E95
11 15A	5.06.	MV	6	0.	11. 1.00000 P17 X1	DMP GAIN 1
12 15B	5.06.	MV	6	0.	12. 1.00000 P17 X1	DMP GAIN 1
13 15A	1.62.	MV	7	0.	13. 1.00000 P17 X1	DMP GAIN 1
14 15C	1.62.	MV	7	0.	14. 1.00000 P17 X1	DMP GAIN 1
15 17A	1.62.	MV	8	0.	15. 1.00000 P17 X1	DMP GAIN 1
16 17B	1.72.	MV	9	0.	16. 1.00000 P17 X1	DMP GAIN 1
17 19A	1.92.	MV	9	0.	17. 1.00000 P17 X1	DMP GAIN 1
18 19B	1.92.	MV	9	0.	18. 1.00000 P17 X1	DMP GAIN 1
19 19A	1.62.	MV	12	0.	19. 1.00000 P17 X1	DMP GAIN 1
20 19B	1.62.	MV	12	0.	20. 1.00000 P17 X1	DMP GAIN 1
21 11A	1.62.	MV	11	0.	21. 1.00000 P17 X1	DMP GAIN 1
22 11B	1.72.	MV	11	0.	22. 1.00000 P17 X1	DMP GAIN 1
23 11A	1.54.	MV	12	0.	23. 1.00000 P17 X1	DMP GAIN 1
24 11B	1.72.	MV	12	0.	25. 1.00000 P17 X1	DMP GAIN 1
25 11A	1.72.	MV	13	0.	26. 1.00000 P17 X1	DMP GAIN 1
26 11B	1.72.	MV	13	0.	27. 1.00000 P17 X1	DMP GAIN 1
27 11A	1.22.	MV	14	0.	28. 1.00000 P17 X1	DMP GAIN 1
28 11B	1.42.	MV	14	0.	29. 1.00000 P17 X1	DMP GAIN 1
29 11A	1.32.	MV	15	0.	30. 1.00000 P17 X1	DMP GAIN 1
30 11B	1.42.	MV	15	0.	31. 1.00000 P17 X1	DMP GAIN 1
31 11A	1.42.	MV	16	0.	32. 1.00000 P17 X1	DMP GAIN 1
32 11B	1.72.	MV	16	0.	33. MASS 67. MASS	DMP GAIN 3
33 MASS	67.	MASS	17	0.	34. FHTK 1148. GCEN	U96 S94 FUR 115A
34 FHTK	1148.	GCEN	18	0.	35. FAIK 152. CCLM	U96 S94 HH91
35 FAIK	152.	CCLM	19	0.	36. FHTK 172. GCEN	U96 S94 JU91
37 PNS	152.	GCEN	20	0.	38. PNS 5292. MV	U96 S94 (U-1/E-5) TORR RANGE
39 TEMP1	5292.	MV	22	0.	40. TEMP1	0.01 AMP GAIN 100

## APPENDIX F

### DISCUSSION OF THE ERRORS IN THE PRESENT FLAME SPECIES CONCENTRATION MEASUREMENTS

In Section IV the measurement of gas species concentration profiles in a one-dimensional flat flame using the present gas monitoring system is described. As is the case with any such experimental measurement, the gas species mole fraction profiles measured have (as presented in Figs. 16, 17 and 19) are subject to certain uncertainties, arising from various sources of error. The purpose of the present section is to briefly discuss these sources of error, in order to better understand the accuracy which can be estimated to the present measurements. Furthermore, this analysis will also provide a basis for evaluating the applicability of the present gas diagnostic system to more complicated environments, such as that in a ramjet combustor.

The first type of error to be discussed is that arising from the accuracy and precision which are characteristic of each individual instruments employed in determining the mole fraction profiles. The instruments or components employed in the present flame species measurements which are subject to variation include the gas source (and the purity thereof) which supplies the gas for the burner; the flow meters used for measuring the flow rate of each individual gas component to the burner; the position dial indicator used for indicating the distance between the burner base and the sampling probe; the mass spectrometer (including all accessory detection system components); and the computer interface system (including the data reduction programs). Judged from the plots shown in Figs. 9-12, as well as from the results reported previously (10,11), the overall precision of the mass spectrometer and the interfaced computer system

is probably on the order of 1-2%. The precisions of all other components just mentioned are known to be well within 1%.

It is well known that a mass spectrometer is a relative value detection system which requires calibration in order to obtain absolute data. For any quantitative gas concentration measurement with a mass spectrometer, a gas calibration test employing a gas mixture of known composition must be conducted prior to the actual sample measurement. In order to properly correct for any potential discrimination effects in the sampling system, as well as in the mass spectrometer detection system, it is important that the calibration be conducted under conditions identical to that of actual sample measurement. In the present flame sampling measurements, owing to experimental difficulties, it is necessary that calibrations for most stable species be accomplished by sampling an unburned gas mixture of known composition which is flowing through the burner at room temperature. This may introduce some calibration error since one is sampling species in an actual flame at a temperature which is typically at 1500-2000°C. It is difficult to estimate the magnitude of this error because many components of the present sampling and detection system may be affected by this large temperature differential. For example, mass discrimination at the sampling site will likely change with the change of the gas temperature. The sample inlet system as presently configured employs a two-stage differential pumping system and only a small portion of the sampled gas actually enters the mass spectrometer while the rest is pumped away. The splitting ratio, which is defined as the ratio of the amount of gas entering the mass spectrometer to that being pumped away, is known to be dependent not only on the molecular weight of each gas component, but also on the temperature of the gas. Gas temperature may also affect the actual operation of the mass spectrometer, such as the ionization efficiency, ion focusing, and other parameters.

The use of a sampling probe in a flame is also known to cause some experimental errors owing to such effects as the disturbance of the concentration gradient at the sampling site, inadequate quenching, post sampling surface reactions, and so on. An in-depth discussion on the use of sampling probes for species concentration measurements has been given in the text of this report, and in Appendix B-D, and will not be repeated here.

As mentioned previously, the mass spectrometer is a relative value detection system. In the present flame sampling experiments, the mass spectrometer yields only the mole fraction of a given gas component relative to that of a reference gas (for example, argon). In order to arrive at the absolute mole fraction values, further assumptions such as that embodied in Eq.(21) must be made. As stated in the text, Eq.(21) is only an approximation since it is known that other species, including stable molecules such as  $H_2$ ,  $H_2CO$ , and radicals such as  $CHO$ ,  $OH$ ,  $H$ ,  $O$ , and ions of various kinds, are all present within the flame at various stages. Naturally, the error resulting from this assumption depends, to a large extent, on the actual concentration of these species which are not taken into account by the equation. One simple way to reduce this error is to employ a reference gas which is chemically inert but which is also present in large quantity. In a combustion system which utilizes air, an obvious choice for the reference gas is nitrogen. Depending on the initial fuel/air ratio, the mole fraction of nitrogen is normally in the range of 70-80%, which likely remains constant, within  $\pm 2\%$ , regardless of the combustion mechanism.

Presented in the following is a discussion of a simplified material balance calculation (ignoring gas diffusion effect) for the elements C, H, and O in the methane/oxygen flame, on the basis of the measured mole fraction profiles shown

in Fig. 19. Since there are only four elements (C, H, O, and Ar) present in this flame, it follows that the sum of the atom fractions (AF) of these four elements must be 1.

$$(AF)_C + (AF)_H + (AF)_O + (AF)_{Ar} = 1 \quad (F-1)$$

The general expression for the atom fraction, for atom  $j$  ( $j = C, H, O, Ar$ ) is,

$$(AF)_j = \frac{\sum M_{i,j} [MF]_i}{\sum N_i [MF]_i} \quad (F-2)$$

where  $M_{i,j}$  is the number of atoms,  $j$ , in a given molecule ( $i = \text{CH}_4, \text{O}_2, \text{H}_2$ , radicals, etc.) within the flame, while  $N_i$  is the total number of atoms in the species  $i$ .

From the data presented in Table VII, the initial atom fractions of the atoms, C, H, O, and Ar prior to ignition can be readily calculated, and are as follows,

$$(AF)_C, \text{ initial} = 0.037 \quad (F-3)$$

$$(AF)_H, \text{ initial} = 0.811 \quad (F-4)$$

$$(AF)_O, \text{ initial} = 0.145 \quad (F-5)$$

$$(AF)_{Ar}, \text{ initial} = 0.007 \quad (F-6)$$

If the effects of lateral and longitudinal diffusion of each species in the flame are ignored, then the atom fraction of each element at any point,  $p$ , along a one-dimensional steady state flame must be constant, that is,

$$(AF)_{C,p} = (AF)_C, \text{ initial} = 0.037 \quad (F-7)$$

$$(AF)_{H,p} = (AF)_H, \text{ initial} = 0.811 \quad (F-8)$$

$$(AF)_{O,p} = (AF)_O, \text{ initial} = 0.145 \quad (F-9)$$

$$(AF)_{Ar,p} = (AF)_{Ar}, \text{ initial} = 0.007 \quad (F-10)$$

A material balance can be determined here to examine the over-all accuracy of the present mole fraction measurements, based on the experimental results shown in Fig. 19. However, in view of the fact that several minor species were not measured here, an assumption such as that made in expressing Eq. (21), must again be employed in order to calculate the atom fractions at each probe position. The results of these material balance calculations for the elements C, H and O are displayed graphically in Fig. F-1, in which the calculated atom fractions,  $(AF)_{j,p}$  ( $j = C, H, O$ ), at all probe positions are expressed as the percent of the initial atom fractions,  $(AF)_j$ , initial. It is seen from this figure that the maximum error for C is approximately 17%, while the maximum error for H is approximately 9%. The material balance for O is not a sensitive indicator because of the large excess of oxygen present in the flame.

It should be noted that part of the error indicated by the data in Fig. F-1, is due simply to the approximate nature of the material balance calculation, which ignores gas diffusion effects. This error does not affect the accuracy of the mole fraction measurements presented in Fig. 19. In view of the non-random nature of the errors indicated by the curves shown in Fig. F-1, it is felt that the most important error in the data obtained in the present experiment (Fig. 19), arises from the assumption made in applying Eq. (21). It is believed that greater accuracy would have been realized if the relative mole fraction of each measured species were expressed instead of the absolute mole fraction used in Fig. 19.

Finally, it is worth noting that a material balance calculation for the elements C and H was also reported by Fristrom (13), who used a similar diagnostic system to that used in the present study, for a  $CH_4/O_2$  flame species concentration measurement. In the latter study, the maximum errors

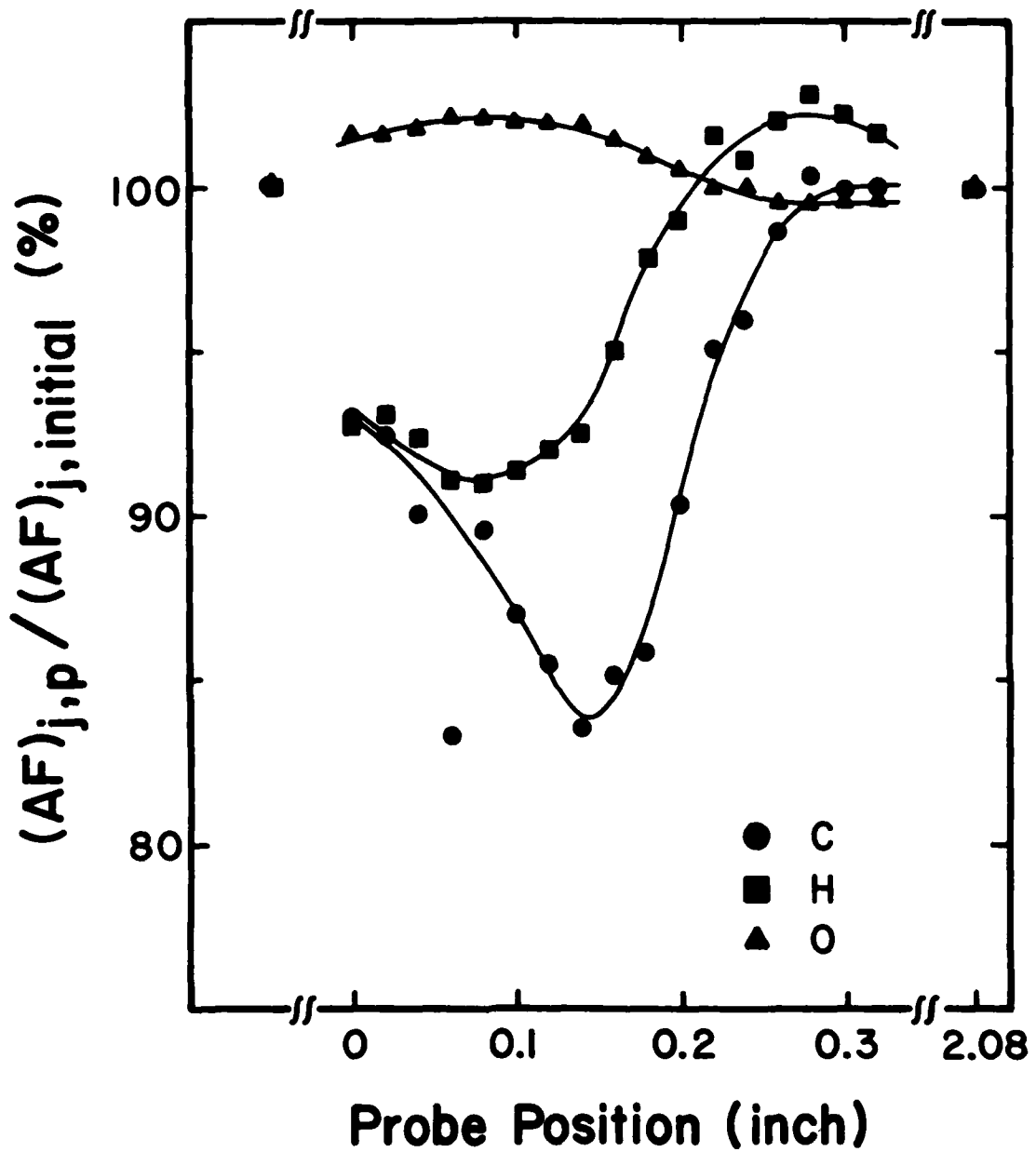


Figure F-1. Material Balance of C, H, and O atoms.

reported for C and H were 12% and 9%, respectively. It should be noted that the material balance calculation employed by Fristrom is based on the concept of mass flow fraction rather than the concept of atom fraction utilized in the present study. The former is a much more rigorous treatment, which requires the measurement of both the detailed flame temperature profiles, and the bulk gas velocity profile along the flame axis, in addition to the mole fraction profiles. As a result, the diffusion effect of each flame specie can be properly taken into account in the final material balance calculation. It should also be noted that in Fristrom's material balance calculations, the concentrations of two minor species,  $H_2$  and  $H_2CO$ , were also included, since the concentration profile data for these two components were also available.

